

DESIGN, SYTHESIS AND CHARACTERIZATION OF
NOVEL SEMICONDUCTING METAL CHALCOGENIDES WITH
MULTIFUNCTIONAL PROPERTIES

by

MIN WU

A dissertation submitted to the
Graduate School-New Brunswick
Rutgers, The State University of New Jersey
in partial fulfillment of the requirements

For the degree of

Doctor of Philosophy

Graduate Program in Chemistry and Chemical Biology

Written under the direction of

Professor Jing Li

And approved by

New Brunswick, New Jersey

January 2008

ABSTRACT OF THE DISSERTATION

Design, Synthesis and Characterization of Novel Semiconducting Metal Chalcogenides with Multifunctional Properties

by MIN WU

Dissertation Director:

Professor Jing Li

Metal chalcogenides possess a wide range of interesting chemical and physical properties, including low-temperature superconductivity, semiconductivity, ionic conductivity, intercalation, and optical properties. To expand chalcogenides beyond their traditional applications, it is desirable to generate novel chalcogenide materials with multifunctionality for uses in the areas of catalysis, separation, ion exchange, and gas storage by modifying the framework architectures and tuning the chemical components. The primary focus of my Ph. D. study is to design and synthesize chalcogenide materials with new structures and interesting multifunctional properties. The large variety of chemical compositions and structures make it possible to tune the properties, such as band gap, luminescence, pore size, surface area, and thermal stability. Most of the

synthesis has been carried out using solvothermal reactions^{refs} in pyrex tube or teflon lined autoclaves. Novel three-dimensional (3D) microporous chalcogenides constructed on building units $[M-Sn-Q]^{n-}$ ($M=Zn, Cd, Mn$; $Q=S, Se$) have been obtained. Their structures have been characterized by both single crystal and powder X-ray diffraction methods. Optical diffuse reflectance experiments have indicated that these compounds are semiconductors with intermediate band gaps between 1.5~2.9eV. The successful doping/substitution of 5%~20% Mn and Se in the $[Zn-Sn-S]^{n-}$ structure allows systematic tuning of the band gap and optical properties of this semiconductor compound. All compounds show a high thermal stability over 400°C. Our studies also show that the guest molecules and cations residing in the open frameworks are exchangeable. Another novel two dimensional ion sulfide $[Fe(en)_3] \cdot [Fe_{16}S_{20}] \cdot en$ compound was synthesized as well. UV-Vis reflectance spectroscopy showed a very low absorption coefficient and small band gap ~0.5eV. Doping/substitution experiments with Co and Mn replacing Fe were carried out and the properties will be discussed. In summary, this work has provided examples of rational synthesis and property tuning of new functional materials with new structure types, and demonstrated structure-property correlation in metal chalcogenide based compounds. It has provided useful information for the future developments of material synthesis with desired multifunctionality.

ACKNOWLEDGEMENTS

At the outset, I would like to express my appreciation to my advisor, Dr. Jing Li, for her enthusiastic supervision during this work. She has constantly encouraged me to remain focused to achieve my goal. Her great vision and insightful comments have helped me to establish the overall goal of this research and to move the investigation forward. I also thank her for her personal care to my family in all these years.

I would like to thank my committee members for their critical comments and kind help during the completion of my thesis.

I would like to thank our collaborators Dr. Gene Hall, Dr. Yuen Tan, Dr. Mark Croft, and Dr. Yong Zhang for their contributions to the characterization and understanding of some of the properties of the new materials included in this thesis, and many thanks to Dr. Thomas J. Emge, Dr. Xiaoying Huang and Dr. Wenhua Bi for single crystal data collection.

I would like to thank the former and current group members. They have provided assistance both technically and mentally during my doctoral research endeavor for the past years. It has been a great pleasure to work with you.

I am also grateful to Professor Hongyou Guo and Professor Lidan Zhang who were my first professors when I started my research career in Solid-State Chemistry, and my special thanks go to Professor Dingsheng Yu and his wife Professor Xianyin Song. They all provided selfless and warm-hearted help, and moreover, opened a new window for me to decide to study abroad.

I am forever indebted to my family. All this wouldn't be possible without the understanding, patience and encouragement from my parents (Guangzhong Wu and Changbi Ke), and my husband Guohong Hu. My little son Shiven Hu, has been the driving force of my achievement.

TABLE OF CONTENTS

Title Page.....	i
Abstract.....	ii
Acknowledgements.....	iv
Table of Contents.....	vi
List of Tables.....	viii
List of Illustrations.....	ix
Chapter One	1
1.1. Tetrahedral Chalcogenide Clusters.....	2
1.2. Assembly of Tetrahedral Clusters and Framework Topologies in Chalcogenide.....	7
1.3. Synthesis Methods and Approaches.....	10
1.4. Properties and Potential Applications.....	11
Chapter Two	15
2.1. Powder X-ray Diffraction (PXRD).....	16
2.2. UV-Vis Diffuse Reflectance Spectroscopy.....	17
2.3. Photoluminescence Spectroscopy	18
2.4. X-ray Absorption Spectroscopy.....	19
Chapter Three	21
3.1. Experimental Section	22
3.2. Results and Discussion	27
3.3. Conclusion.....	30

Chapter Four	31
4.1. Experimental Section	32
4.2. Results and Discussion	38
4.3. Concluding Remarks.....	50
Chapter Five	52
5.1. Experimental Section	53
5.2. Results and Discussion	66
5.3. Conclusion and summary	77
Reference	78
Curriculum Vita	81

LISTS OF TABLES

Chapter Three

Table 1. Crystallographic data for 1	24
Table 2. Atomic coordinates and equivalent isotropic temperature factors (\AA^2) for 1	25
Table 3. Selected bond lengths (\AA) and bond angles ($^\circ$) for 1	26

Chapter Four

Table 4. Crystallographic data and structure refinement of 2	34
Table 5. Atomic coordinates ($\times 10^4$) and equivalent isotropic displacement parameters ($\text{\AA}^2 \times 10^3$) for 2	35
Table 6. Selected bond lengths (\AA) and angles ($^\circ$) for 2	36

Chapter Five

Table 7. Crystallographic data and structure refinement for 3	55
Table 8. Atomic coordinates ($\times 10^4$) and equivalent isotropic displacement parameters ($\text{\AA}^2 \times 10^3$) for 3	56
Table 9. Selected bond lengths (\AA) and angles ($^\circ$) for 3	58

LIST OF ILLUSTRATIONS

Chapter One

- Figure 1. Ball-and-stick diagrams of T2, T3 and T4 supertetrahedral clusters. 4
- Figure 2. P1 (M_8Q_{17}) and P2 ($M_{26}Q_{44}$) penta-supertetrahedral clusters. 5
- Figure 3. Cluster building blocks: (a) Adamantane-like $[Ge_4Se_{10}]^{4-}$; (b) $[In_3Te_9]^{9-}$; and (c) $[M_5Q_{12}]^{3-}$. 6
- Figure 4. Chalcogenide clusters assembled by (a) Corner sharing terminal chalcogen atoms for T2-T3; (b) Corner sharing for T4-T4; (c) Edge sharing for other types of clusters; (d) $-S-S-S$ bridge sharing for T4-T4. 9

Chapter Two

- Figure 5. Schematic diagram of Powder X-ray Diffractometer. 16
- Figure 6. Reflection of X-rays from two planes of atoms in a solid. 17
- Figure 7. Schematic diagram of UV-vis diffuse reflectance measurement system. 18
- Figure 8. Spectrum of Kubelka-Munk function $F(R)$ vs. photo energy ($h\nu$). 18
- Figure 9. Diagram of photoluminescence process in semiconductors. 19
- Figure 10. Schematic diagram of fluorescence detection mode used in XAS experiments. 20

Chapter Three

- Figure 11. (a) Building block $[Zn_4Sn_3Se_{16}]^{12-}$; (b) View of the 3D network

of 1 along [12-1].	28
Figure 12. Powder X-ray diffraction pattern of 1 (red) shown along with simulated pattern from the single crystal data (black).	29
Figure 13. Optical absorption spectrum for 1 . Estimated band gap is 2.6 eV.	29
Chapter Four	
Figure 14. (a) $SM_4(SnS_4)_6$ cluster ($M = Zn, Sn$); (b) View of the 3D network without Na cations and H_2O molecules; (c) Highly symmetric pore with Na cations (purple) and H_2O molecules.	40
Figure 15. (a) Building block of $[M_4Sn_3S_{13}]^{5-}$ ($M = 0.125Sn + 0.875Zn$) in 2 ; (b) Building block of $[M'_4Sn_3Se_{13}]^{6-}$ ($M' = Zn, Hg$) in $K_3Rb_3Zn_4Sn_3Se_{13}$ and $K_6Hg_4Sn_3Se_{13} \cdot MeOH(H_2O)_3$.	42
Figure 16. (a) TGA profile and (b) DSC plot for compound 2 .	43
Figure 17. Powder X-ray diffraction patterns of $[Na_5Zn_{3.5}Sn_{3.5}S_{13}] \cdot 6H_2O$ and Mn, Se substituted compounds with the substituent concentration between 3% and 20%.	45
Figure 18. (a) Optical absorption spectra of 2 and 5%, 10%, 15%, and 20% Se substituted compounds. (b) Optical absorption spectra of 2 and 3%, 5%, 10%, and 20% Mn substituted compounds.	46
Figure 19. Band gap energy as a function of Se concentration in 2 .	47
Figure 20. (a) TGA profile showing removal of water molecules in the channels. (b) TGA profile after the exchange by DMSO. A weight loss of 3 % was observed.	48

Figure 21. Powder X-ray patterns for DMSO solvent exchange experiments	49
Figure 22. Room temperature photoluminescence of Mn doped [Na ₅ Zn _{3.5} Sn _{3.5} S ₁₃] \cdot 6H ₂ O with varying Mn concentration.	50

Chapter Five

Figure 23. Powder X-ray diffraction pattern of 3 .	65
Figure 24. (a) Anionic [Fe ₁₆ S ₂₀] layers (b) Side view of the layered structure showing [Fe(en) ₃] and ethylenediamine molecules residing between the [Fe ₁₆ S ₂₀] layers.	67
Figure 25. (a)XAS spectra of Fe <i>K</i> edge for a serious of Fe compounds with different valence charge. (b). XAS spectra of Fe <i>K</i> Pre-edge.	70
Figure 26. TGA pattern of compound 3 gave 19.9% weight loss at around 350 °C.	71
Figure 27. Powder X-ray pattern of 3 after TGA 500° C.	72
Figure 28. TGA pattern run until 160° C and kept for 40 minutes.	72
Figure 29. Powder X-ray pattern of before and after TGA 160° C.	73
Figure 30. UV-Vis diffuse reflectance spectrum of compound 3 .	73
Figure 31. Powder X-ray patterns of the original and doped/substituted compounds.	75
Figure 32. UV-Vis diffuse reflectance spectrum of Co/Mn doped compounds.	76

CHAPTER ONE

Introduction

Chalcogens are group 16 elements in the periodic table group 16. The group consists of oxygen (O), sulfur (S), selenium (Se), tellurium (Te), polonium (Po), and ununhexium (Uuh). The name is generally considered to mean “ore former” from the Greek *chalcos* “ore” and *-gen* “formation”. Compounds containing a chalcogen element as an anion (particularly S, Se and Te) are commonly termed chalcogenides. The chalcogenide clusters with well-defined size and composition represent a lower limit of semiconducting nanoparticles and serve to span the size gap between quantum dot structures and molecular species in solution.¹ Open-framework chalcogenides with micropores may lead to interesting host-guest chemistry different from that of zeolites. In contrast to zeolites, which are insulators, metal chalcogenide materials are usually semiconductors. Therefore open-framework chalcogenides with their porosity and optoelectronic properties²⁻⁷ are unique and important candidates for technological applications such as shape- and size- selective sensors, high-surface area photocatalysts and photoelectrodes.³ Layered transition metal chalcogenides also have a wide range of applications, such as catalysts⁸, lubricants⁹, and cathodes in lithium batteries.¹⁰ Most of their unusual and useful properties arise from the layered “sandwich-like” structure. They have been also explored for photovoltaic energy conversion, because these compounds exhibit promising characteristics for the application in thin film solar cells.¹¹

1.1. Tetrahedral Chalcogenide Clusters

Designing and understanding chalcogenide clusters can be very helpful for the development of porous chalcogenides. This is because many three-dimensional (3D) chalcogenides are constructed from clusters. Tetrahedral clusters are loosely defined as

those behaving like pseudo-tetrahedral atoms (tetrahedron with less symmetry). Metal cations in tetrahedral chalcogenide clusters are usually from Groups 12-14 (e.g., Zn, Cd, Ga, In, Ge, Sn) and first row transition metals including Mn, Fe, Co, Cu. Recent synthetic efforts generally involve chalcogenides with only one (M^{2+} , M^{3+} , and M^{4+}) or two metal cation combination (M^{4+}/M^{3+} , M^{4+}/M^{2+} , M^{4+}/M^+ , M^{3+}/M^{2+} , and M^{3+}/M^+). There are very few reported open framework chalcogenides with more complex compositions.

The tetrahedral coordination of metal cations is common in both chalcogenides and zeolites. However, it is much more common in chalcogenides because of the coordination geometry of chalcogen anions. The typical value for a M-S-M angle is approximately between 105° and 115° , smaller than that of a typical M-O-M angle in zeolites (usually between 140° and 150°).¹² This tendency of the M-S-M angles to be close to 109° means that all framework elements can adopt tetrahedral coordination (the tetrahedral angle is 109.4° in a regular tetrahedron).

Among the most common chalcogenide clusters are a series of supertetrahedral clusters. They were denoted as T_n (n = number of metal layers^{13, 14}). The corresponding formula for an isolated supertetrahedral cluster T_n is Mt_nQt_{n+1} , where $t_n = n(n+1)(n+2)/6$. The general formula of T_n clusters with n ranging from 1 to 5 are: MQ_4 (T_1), M_4Q_{10} (T_2), $M_{10}Q_{20}$ (T_3), $M_{20}Q_{35}$ (T_4), and $M_{35}Q_{56}$ (T_5) (M = metal ion, Q = chalcogen), respectively (Figure 1).¹⁵ They are regular, tetrahedrally shaped fragments of the cubic ZnS type lattice. So far the T_5 cluster is the largest supertetrahedral cluster which can be prepared as three dimensional or two dimensional superlattices.^{16,17} The coordination number of anions is an important aspect in the synthetic design of supertetrahedral clusters. T_2 cluster consists of only bicoordinated anions. T_3 cluster consists of

bicoordinated as well, and tricoordinated anions occurred at the face center. Starting from T4 cluster, tetra-coordination of chalcogen anions begins to occur. It is also helpful to understand surface atoms and core atoms in a cluster. Usually surface atoms are ones at corners, edges and faces of the cluster, while core atoms are those inside of the cluster. T1, T2, and T3 clusters have no core chalcogen atom, while the core atom in a T4 cluster is occupied by tetra-coordinated chalcogen atom. For larger clusters ($n > 4$), the core atoms are built a $T(n-4)$ cluster with tetra-coordinated chalcogen atoms.

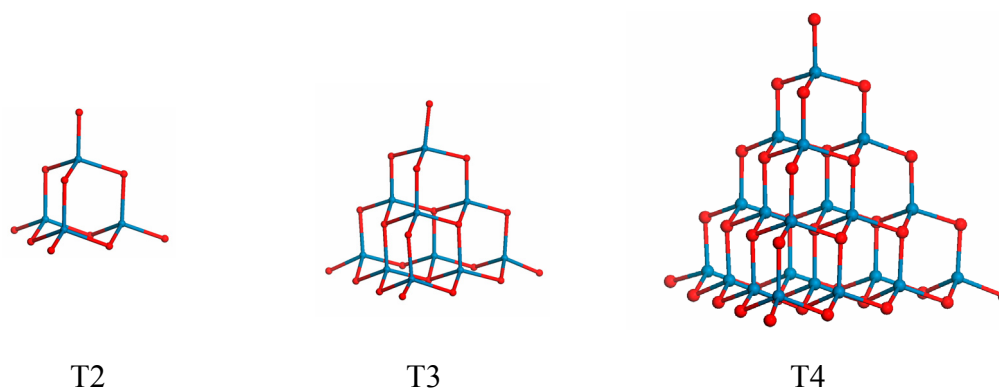


Figure 1. Ball-and-stick diagrams of T2(eg. $\text{Sn}_4\text{Q}_{10}^{4-}$ ($\text{Q}=\text{Se}, \text{Te}$))¹⁶; T3 (eg. $\text{In}_{10}\text{S}_{20}^{10-}$)¹⁷; and T4 (eg. $\text{Cd}_4\text{In}_{16}\text{S}_{35}^{14-}$)¹⁸ supertetrahedral clusters (Chalcogen anions Q are shown as red; metal cations M are shown as blue).

Another type of tetrahedral clusters called penta-supertetrahedral clusters (Figure 2) were denoted as Pn .¹⁵ The corresponding formula for this kind of cluster Pn is $\text{M}_{(4t_n+t_{n+1})}\text{Q}_{(4t_{n+1}+t_n)}$, where $t_n = n(n+1)(n+2)/6$. The size index n is the number of layers of M atoms in the core. A Pn cluster is constructed by coupling four supertetrahedral clusters Tn onto the faces of an antisupertetrahedral cluster of the same order. An antisupertetrahedral cluster here is defined as having the same geometrical features as

supertetrahedral cluster with the position of cations and anions being exchanged. For example, the P1 cluster consists of four T1 clusters (MQ_4) at the corners and one anti-T1 cluster (QM_4) at the core, resulting in the composition $(\text{MQ}_4)_4(\text{QM}_4)$; the P2 cluster contains four T2 clusters and one anti-T2 cluster, giving the composition $(\text{M}_4\text{Q}_{10})_4(\text{Q}_4\text{M}_{10})$. The same procedure can be used to derive the composition of the other Pn clusters.

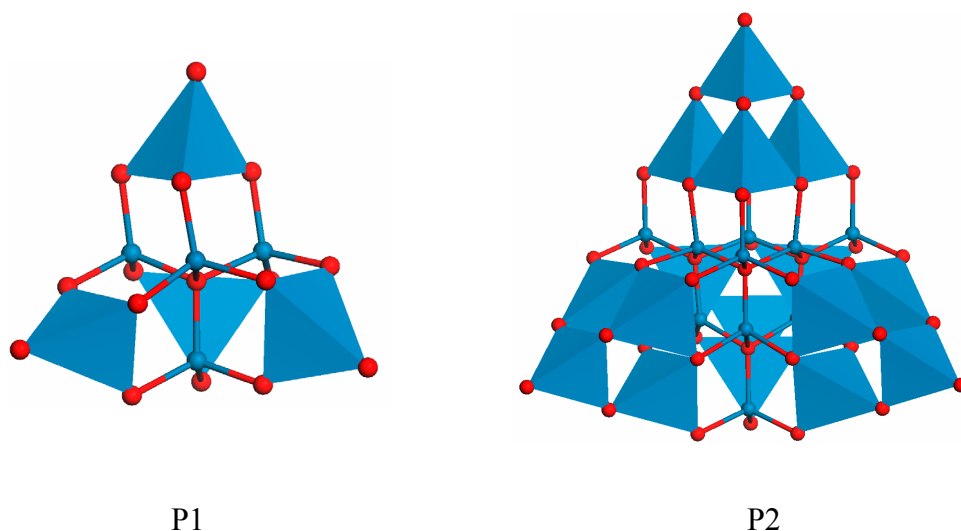


Figure 2. P1 (M_8Q_{17} , eg. $[\text{M}_4\text{Sn}_4\text{S}_{17}]^{10-}$ ($\text{M} = \text{Mn, Fe, Co, Zn}$))¹⁹ and P2 ($\text{M}_{26}\text{Q}_{44}$, eg. $[\text{Li}_4\text{In}_{22}\text{S}_{44}]^{18-}$)¹ penta-supertetrahedral clusters. (Chalcogen anions Q are shown as red; metal cations M are shown as blue).

Certainly, other variations of tetrahedral chalcogenide clusters are possible by adding atoms into or removing atoms from above tetrahedral clusters. Figure 3 shows several cluster units that we have found in chalcogenide structures, including (a) semi-cube $[\text{M}_3\text{Q}_7]^{2-}$ ²⁰, (b) $[\text{M}_3\text{Q}_7]^{3-}$ ²¹, and (c) $[\text{M}_5\text{Q}_9]^{3-}$ ²².

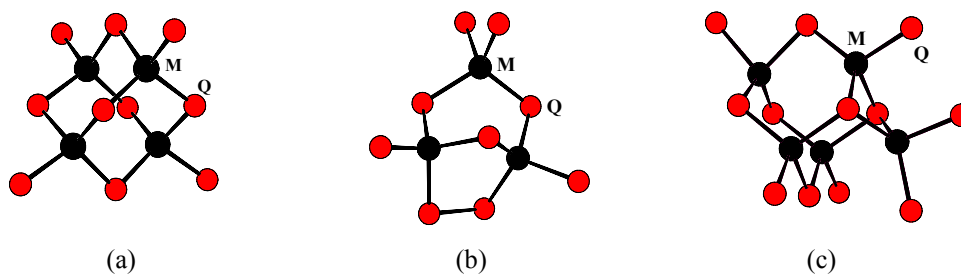


Figure 3. Cluster building blocks: (a) Adamantane-like $[\text{Ge}_4\text{Se}_{10}]^{4-}$ ²⁰; (b) $[\text{In}_3\text{Te}_9]^{9-}$ ²¹; and (c) $[\text{M}_5\text{Q}_{12}]^{3-}$ ²².

The charge on metal cations is an important factor affecting the size of chalcogenide clusters.¹⁵ Divalent metal cations (M^{2+}) have been widely used for preparing chalcogenide clusters. While using only M^{2+} as metal cations in chalcogenide clusters which has been reported is quite limited in small size clusters such as T2, T3. This is because the coordination number of surface chalcogen sites to a framework metal cation is low and the valence sum from adjacent M^{2+} cations is usually inadequate to balance the large number of chalcogen anions. The use of M^{3+} (e.g., In^{3+} and Ga^{3+}) or M^{4+} cations (e.g., Sn^{4+} and Ge^{4+}) can provides more bond valence to balance surface chalcogen anions. The larger size of chalcogenide clusters such as T4, T5 has been generated by using $\text{M}^{3+}/\text{M}^{2+}$ metal cation combination. To meet the additional valence requirement of chalcogen anions, alkali metal (eg. Na^+ and K^+)²³ and some organic groups such as amine (eg. di-n-butylamine)²⁴ were usually served as cations. The charge effect is related to Pauling's electrostatic valence rule that states that the valence of each anion is exactly or nearly equal to the sum of the electrostatic bond strength to it from

adjacent cations. P.Y. Feng termed 'local charge balance' to refer to this situation where the charge of chalcogen anion is balanced locally by its adjacent metal cations. Another term called 'global charge balance' is used to refer to the overall charge density matching between the host framework and the structure-directing agent.¹⁵

All chalcogenide clusters discussed above are anionic and have no cavities associated with them. Interconnection of these clusters can lead to covalent framework structures containing large pores and high pore volume. In a giving 3D network replacing each small size tetrahedron (such as T2 or P1) with a larger tetrahedron (such as T3 or P2) can create a larger pore network due to the increased size of the building blocks.²⁵

1.2. Assembly of Tetrahedral Clusters and Framework Topologies in Chalcogenide

It has long been known that the physical properties of these 2D and 3D superlattices made of clusters can be completely different from those of the bulk solid made of single atoms of the same elements. The materials using clusters as the 'building blocks', rather than single atoms, may have novel properties. They behave like molecular matter and their packing has translation and even orientation order.²⁶⁻²⁸ The properties of these new materials depend not only on the structure of individual building units, but also the 2D or 3D packing of the nano-clusters. It is a self-assembly of passivated nano-clusters into monolayers, thin films, and superlattices of size-selected clusters encapsulated in a protective compact coating. Given the simultaneous availability of various clusters, different assemblies can be achieved. The most common situation is for clusters of the same size to crystallize into a uniform superlattice. Tetrahedral clusters in chalcogenides can be joined together with a single chalcogen anion by corner sharing or

with double chalcogens by edge sharing. Poly-chalcogen anions serve as bridges in several cases as well, such as $-S-S-S-$ (3 chalcogen atoms) bridge.²⁹ Examples are shown in Figure 4. Several 1D, 2D and 3D topological types have been observed from the assembly of T, P and other types of clusters.¹² For small T2 and T3 clusters, three dimensional single and double diamond-type structures formed are common.³⁰⁻³³ However, for T3-T4, T4, or T5, only the double diamond-type structure has been realized so far^{24, 29, 34}.

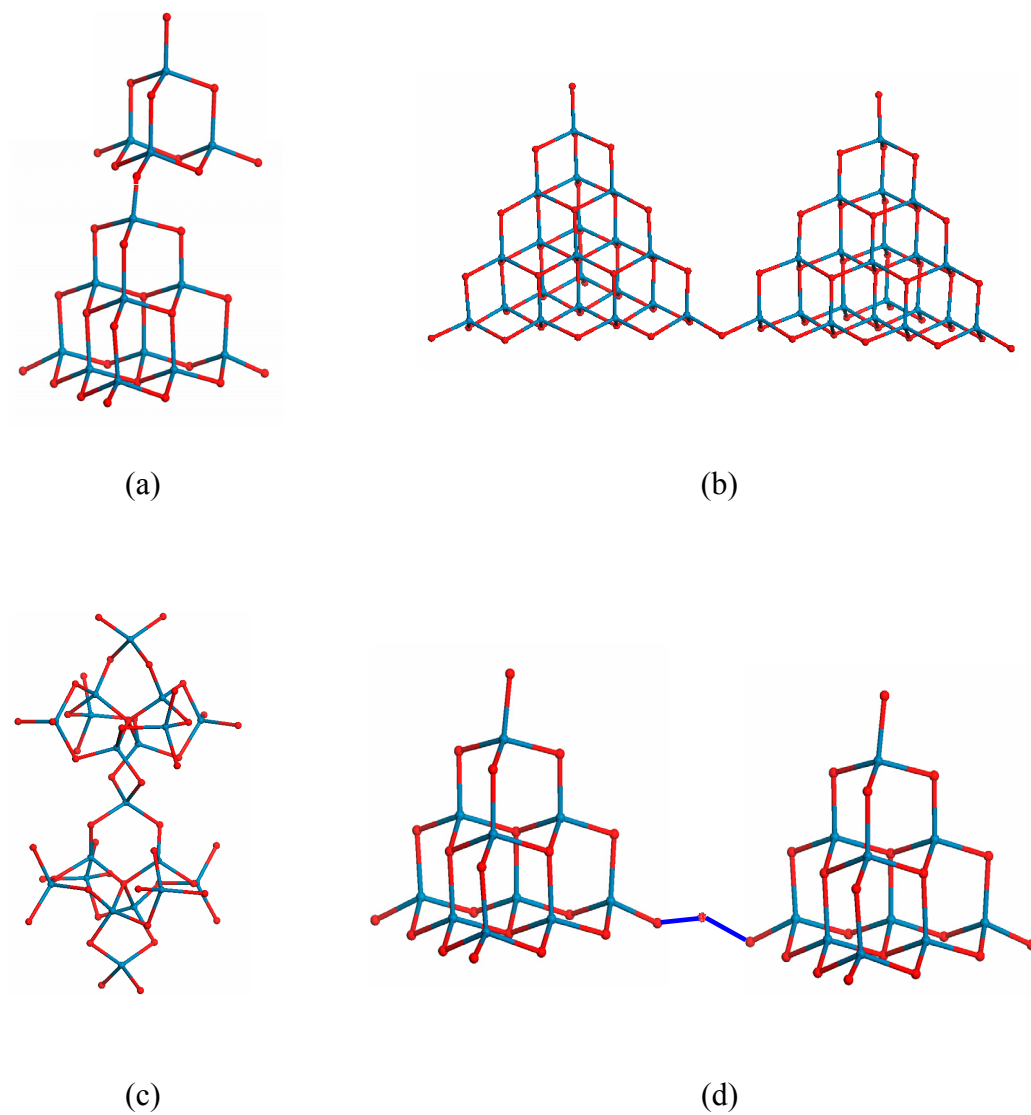


Figure 4. Chalcogenide clusters assembled by (a) Corner sharing terminal chalcogen atoms for T2-T3; (b) Corner sharing for T4-T4; (c) Edge sharing for other types of clusters; (d) -S-S-S bridge sharing for T4-T4.

Until now, the number of the 3D framework structure types in chalcogenide materials which have been observed remains small. There are several factors controlling the types of superlattices that may form, such as inflexibility of the M-Q-M angles. The geometry and charge distribution are important factors as well. On the other hand, hydrogen bonding in chalcogenides is much weaker compared to oxides. So the host-guest electrostatic interaction enhanced by the highly negative framework is expected to play a significant role in chalcogenides.

1.3. Synthesis Methods and Approaches

Much of the metal chalcogenide synthesis has been previously carried out by solid-state reactions. Solid-state reactions occur among solid reactants and are characterized by slow nucleation and diffusion processes. The most straightforward route³⁵ is the combination of the elements at high temperatures.³⁶ These elemental combination reactions can also be promoted in a microwave oven where the synthesis time is significantly reduced.³⁷ Such process requires a significant energy input and gives little control in particle size of products. A low-energy approach is the precipitation of metal chalcogenides from aqueous solutions of the metal cations by use of H₂Q (Q = chalcogen).³⁸ Problems with this method include the use of very toxic reagents H₂Q and high degree of impurity.

The recent development in soft synthesis of metal chalcogenides has been motivated by the tremendous progress in the crystal engineering of organic and coordination compounds via molecular building-block approaches. The key issue is that by turning down the temperature, the solid-state synthesis may proceed in a more controlled and predictable manner. The mild temperature also leads to many kinetic

phases. Among various soft synthesis techniques, hydro(solvo)thermal synthesis is the most common method adopted.²¹ It involves use of water or organic solvents in the vicinity of its critical point at elevated temperatures and pressures in a closed system. Metal salts, for example metal chlorides, have been used in many hydro(solvo)thermal reactions as a source of metal ions, such as ZnCl_2 , InCl_3 , SbCl_3 etc. In some reactions, the chloride ion (Cl^-) also functions as a mineralizer.³⁹ A_2Q and elemental Q (A = alkali metal) are often used as sources of alkali metal ions and polychalcogen anions (Qn^{m-}).⁴⁰ A number of binary metal chalcogenides such as Sb_2S_3 ⁴¹ and SnS_2 ⁴² have also been used in some reactions.

Under hydro(solvo)thermal conditions, the solvent behaves much differently from what is expected at ambient conditions.³⁹ Certain properties of the solvent, such as density, viscosity and diffusion coefficient, are dramatically changed. Consequently, the solubility, the diffusion process and the chemical reactivity of the solid reactants are greatly increased or enhanced. This enables the reaction to take place at a much lower temperature. Unlike most other solid-state synthetic techniques, hydro(solvo)thermal synthesis concerns a much milder and softer chemistry conducted at low temperatures. It makes it possible to leave polychalcogen building blocks intact. Such a synthetic route allows formation and isolation of phases that may not be accessible at higher temperatures because of their metastable nature.^{6, 43}

1.4. Properties and Potential Applications

Microporous aluminosilicate zeolites have largescale commercial applications such as gas separation and petroleum processing.⁴⁴ As mentioned before, oxides are usually

insulators and have very limited electro-optic applications. Therefore, extensive studies have been made on metal chalcogenides because these materials often possess interesting optoelectronic and pore properties simultaneously, and thus, have high surface area, ion exchange capacity, high framework charge density, and photoluminescent properties in a single crystal lattice.⁴⁵ One nice example is a family of chalcogenide zeolite analogs³⁰ synthesized under solvothermal conditions by using organic solvents as templates. These structures involve substitution of three elements, O^{2-} by S^{2-} or Se^{2-} , Si^{4+} by Ge^{4+} or Sn^{4+} , and Al^{3+} by Ga^{3+} or In^{3+} . All four $[M^{4+}-M^{3+}]$ combinations ($[Ga-Ge]$, $[Ga-Sn]$, $[In-Ge]$, and $[In-Sn]$) have been realized, resulting in four different zeolite-type topologies.

Ion exchange with light cations such as mono-valent metal cations followed by calcinations makes it possible to remove larger size organic cations inside the cages which serve as charge balancing species for anionic chalcogenide clusters. For example, after ion exchanged with Cs^+ , the percentages of C, H, and N in $GaGeS$ -TAEA (TAEA = tris(2-aminoethyl)amine, $C_6H_{18}N_4$)³⁰ were dramatically reduced. The exchanged sample remains highly crystalline like the original one. And this Cs^+ exchanged compound has a high Langmuir surface area (specific surface area calculated by Langmuir method used for Type I adsorption⁴⁶) of $807\text{ m}^2/\text{g}$ and a micropore volume of $0.23\text{ cm}^3/\text{g}$. Moreover, these open framework chalcogenides are also strongly photoluminescent and can be excited with wavelengths from 360 to 420 nm. The emission maximum occurs in the range from 460 to 508 nm.³⁰ The general trend is that materials with heavier elements are excited and luminescent at a longer wavelength.

An open-framework material has another advantage for applications such as low-temperature fast-ion conductors because its open channels provide paths for easy ion

migration. Open-framework chalcogenides, due to their higher anionic framework, are anticipated to be better ion conductors than zeolites. Another advantage of open-framework chalcogenides is the high concentration of mobile cations. Chalcogenides, with more negative frameworks, therefore have much more charge-balancing cations. ICF-26 (Li-In-S) which was reported by Feng's group has the specific conductivity of $1.5 \times 10^{-2} \text{ ohm}^{-1} \text{ cm}^{-1}$ at 27°C under 100% relative humidity.⁴⁷ Of particular interest is the high ionic conductivity observed in one lithium-containing material, ICF-22 InS-Li⁴⁷. Its specific conductivity reaches up to $1.1 \times 10^{-2} \text{ ohm}^{-1} \text{ cm}^{-1}$ at 24°C under 31.7% relative humidity. Generally the ionic conductivity of these chalcogenides increases with the relative humidity.

Microporous chalcogenide materials integrate tunable band gaps with open framework architecture and are potential candidates for efficient photocatalysts, particularly in the visible-light region. By controlling framework architecture, it is possible to tune the band structure (both band positions and gap) of an open-framework solid within a given compositional domain. The open framework construction also helps to increase the number of active reaction sites owing to a high surface area. Photocatalysts based on crystalline porous chalcogenides have been reported recently.⁴⁸ $\text{Na}_{14}\text{In}_{17}\text{Cu}_3\text{S}_{35} \cdot x\text{H}_2\text{O}$ is particularly interesting as it is compositionally related to CuInS_2 , which is one of the most efficient photovoltaic materials. About $18 \text{ } \mu\text{mol h}^{-1} \text{ g}^{-1}$ of H_2 gas was produced over the $\text{Na}_{14}\text{In}_{17}\text{Cu}_3\text{S}_{35} \cdot x\text{H}_2\text{O}$ catalyst under irradiation with visible light. This activity was maintained for over 96 h and more than 890 mmol of H_2 gas evolved during this period. The quantum efficiency for this compound was determined to be about 3.7% at 420 nm. These unique advantages of porous

semiconductors, such as having a high surface area and the easy incorporation of light sensitizers, provide new opportunities that can be explored to maximize photocatalytic efficiency, particularly in the visible-light region.

In conclusion, metal chalcogenides compounds combined with porous nature and useful electronic, optical properties are not only fundamentally important but may also find applications in gas adsorption, electrocatalysis, photocatalysis etc.

CHAPTER TWO

Instrumental Analysis

2.1. Powder X-ray Diffraction (PXRD)

Powder X-ray diffraction has been widely used for characterization of solid materials. Each solid has its unique characteristic X-ray powder pattern which can be used as a 'fingerprint' for its identification. PXRD experiment requires a X-ray source, the sample under investigation and a detector to pick up the diffracted X-rays. Figure 5 is a schematic diagram of a powder X-ray diffractometer. The most common X-ray radiation is emitted by Cu, whose characteristic wavelength for the K radiation is $\lambda = 1.5418 \text{ \AA}$. When the incident beam strikes a powder sample, diffraction occurs in every possible orientation of 2θ in a range that depends on different systems. And the diffracted beam is detected by using a moveable detector such as a Geiger counter. The resolution of an X-ray diffraction detector is determined by the Bragg equation: $n\lambda = 2d\sin\theta$ (Figure 6)

where $n = 1, 2, 3, \dots$; λ = wavelength (1.5418 \AA for Cu); d (d-spacing) = interatomic spacing; θ = the diffraction angle.

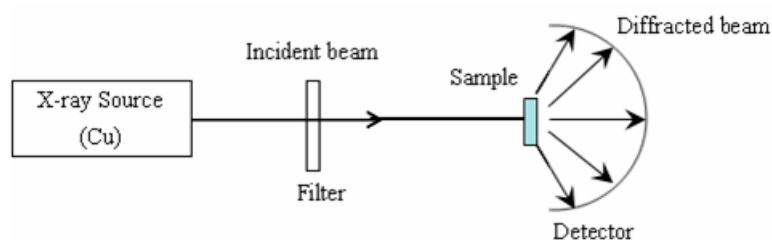


Figure. 5. Schematic diagram of Powder X-ray Diffractometer.

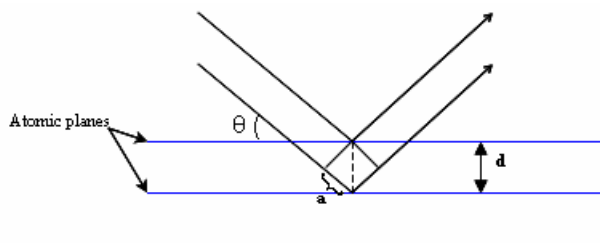


Figure 6. Reflection of X-rays from two planes of atoms in a solid.

2.2. UV-Vis Diffuse Reflectance Spectroscopy

Optical diffuse reflectance spectra were measured at room temperature with a Shimadzu UV-3101PC double beam, double monochromator spectrophotometer. The simple schematic diagram is shown in Figure 7. BaSO₄ powder was used as a standard (100% reflectance). Data were collected in the wavelength range of 200-2000 nm. The thickness of the sample was approximately 2.0-3.0 mm, which is much greater than the size of the individual particles. Therefore, an idea diffuse reflection can be assumed and the scattering factor (S) can be taken as a constant.⁴⁹ For a semiconducting sample construction of Kubelka-Munk function $F(R)^{50}$ vs. $h\nu$ is plotted in Figure 8. It shows a linear region just above the optical absorption edge. Extrapolation of this line to the photon energy ($h\nu$) axis yields the band gap energy of the semiconducting sample.

Kubelka-Munk function: $F(R) = \alpha/S = (1-R)^2 / 2R$

where R_{∞} is reflectance at given wavelength; α is absorption coefficient; and S is scattering coefficient.

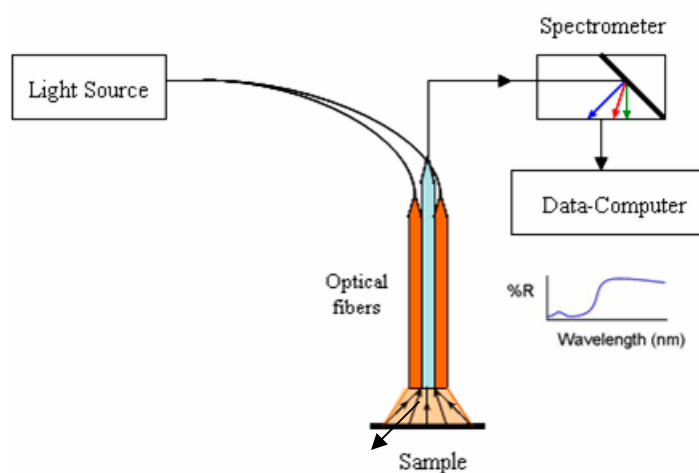


Figure 7. Schematic diagram of UV-vis diffuse reflectance measurement system.

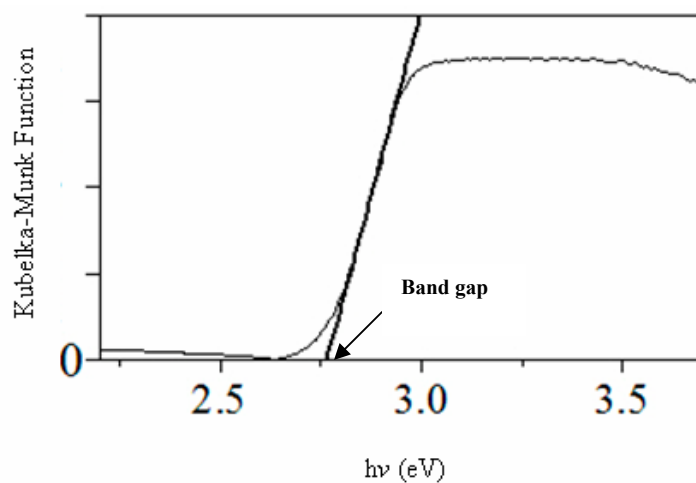


Figure 8. Spectrum of Kubelka-Munk function vs. photo energy ($h\nu$).

2.3. Photoluminescence Spectroscopy

Photoluminescence spectroscopy is a nondestructive method of probing the electronic structure of materials. Light is directed onto a sample where it is absorbed and

imparts excess energy into the material. The excess energy can be dissipated by the sample through the emission of light or luminescence. This process is called photo-excitation. The energy of the emitted light (photoluminescence) relates to the difference of transition between the two electron states (the excited state and the ground state). In semiconductors the most common radioactive transition is between states in the conduction and valence bands, with the energy difference being known as band gap (Figure 9).

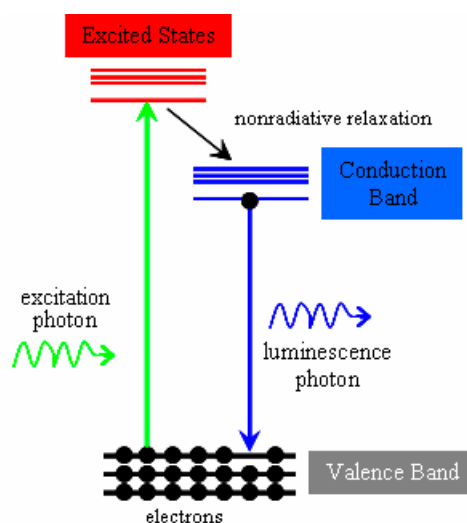


Figure 9. Diagram of photoluminescence process in semiconductors.

2.4. X-ray Absorption Spectroscopy

X-ray absorption spectroscopy (XAS) is a valuable tool for studying electronic properties, valence state of the element, and local structural environment around an element in varied materials⁵¹. There are three detection methods used commonly including transmission mode, fluorescence mode and total electron yield mode. The Fe-*K*

XAS measurements were performed in the fluorescence mode on crystal samples on beamline X19A at the Brookhaven National Synchrotron Light Source(see Figure 10). In a fluorescence experiment, the incident beam of monochromatic X-rays is monitored by a semitransparent ionization chamber (I_0), and the flux of X-rays fluorescence through the sample is collected by ionization chamber (I). The X-ray absorption coefficient of the sample is given by $\mu_x = I_0/I$.

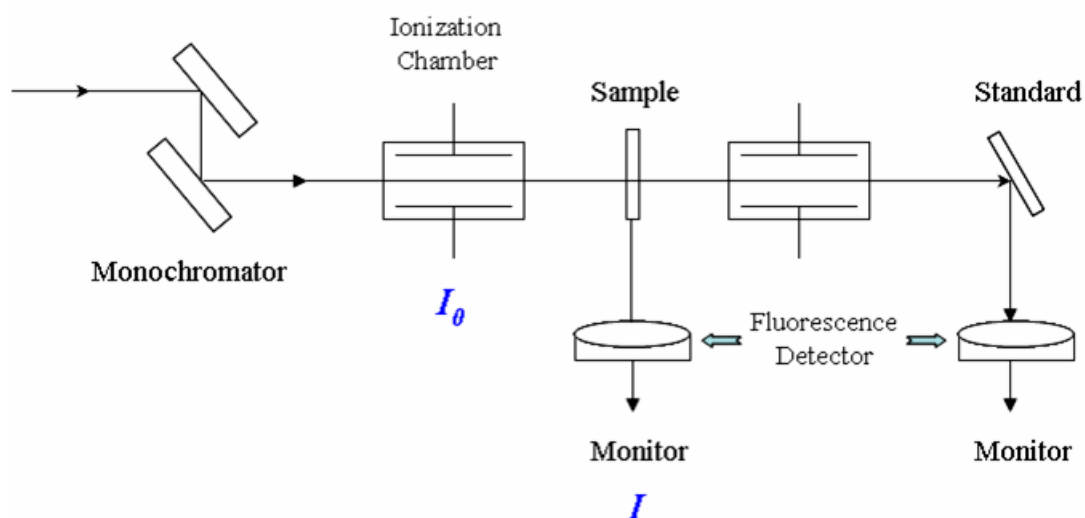


Figure 10. Schematic diagram of fluorescence detection mode used in XAS experiments.

CHAPTER THREE

An Open-framework Bimetallic Chalcogenide Structure

$\text{K}_3\text{Rb}_3\text{Zn}_4\text{Sn}_3\text{Se}_{13}$ Built on a Unique $[\text{Zn}_4\text{Sn}_3\text{Se}_{16}]^{12-}$ Cluster:

Synthesis, Crystal Structure, Ion Exchange and Optical

Properties

Single crystals of $\text{K}_3\text{Rb}_3\text{Zn}_4\text{Sn}_3\text{Se}_{13}$ ²³ were synthesized by solvothermal method. The building block in this structure is a $[\text{Zn}_4\text{Sn}_3\text{Se}_{16}]^{12-}$ cluster which consists of four ZnSe_4 and three SnSe_4 tetrahedra connected through corner-sharing of Se atoms. The 3D network contains intersecting channels running parallel to the crystallographic [211], [1-1-1] and [12-1] directions. The disordered K^+ and Rb^+ cations reside in these channels. Ion exchange of Cs^+ with disordered Rb^+/K^+ ions in the structure showed a partial replacement of 15.8%. Optical diffuse reflectance experiments were carried out and gave a sharp absorption edge at 2.6 eV.

3.1. Experimental Section

Single crystals of $\text{K}_3\text{Rb}_3\text{Zn}_4\text{Sn}_3\text{Se}_{13}$ (**1**) were grown in a reaction containing 0.079g (0.50mmol) of K_2Se (prepared as literature procedure)⁵², 0.0495g (0.60mmol) of Se (powder, -325 mesh, 99.5%, Alfa Aesar), 0.030g (0.25mmol) of Sn (powder, -325 mesh, 99.8%, Aldrich), 0.060g (0.5mmol) of RbCl (99.8%, Alfa Aesar) and 0.023g (0.017mmol) of ZnCl_2 (anhydrous, 98.7%, Fisher) loaded in thick wall Pyrex tube, followed by addition of 0.20 ml distilled H_2O and 0.20 ml CH_3OH (99.9%, Fisher). The reaction mixture sealed in the tube was heated at 130 °C in furnace for 6 days. The products were washed with 80% alcohol followed by distilled water and pure yellow crystals were obtained with a calculated 60% yield.

Powder X-ray diffraction analyses were used for structure determination and phase identification. X-ray powder diffraction analyses were performed on a RigakuD/M-2200T (The Woodlands, Texas USA) automated diffraction system (Ultima+). The measurements were made with a 2θ range between 5 and 60°, at the operation power of

40 KV/40 mA. Single crystal X-ray measurements were made on an Enraf-Nonius CAD4 diffractometer (Rotterdam, The Netherlands) with graphite-monochromated Mo $K\alpha$ Radiation. $R_1 = 0.0515$ from 2030 reflections with intensity $I > 2(I)$. The unit cell parameters, along with data collection and refinement details, are listed in Table 1. Atomic coordinates and equivalent isotropic temperature factors are listed in Table 2. Shown in Table 3 are bond lengths (\AA) and bond angles ($^\circ$). Optical diffuse reflectance spectra were measured at room temperature using a Shimadzu (Columbia, Maryland USA) UV-3101PC double beam, double monochromated spectrophotometer. A Perkin-Elmer (Waltham, Massachusetts USA) Optima 3000XL Inductively Coupled Plasma-Atomic Emission Spectrometer (ICP-AES) was used for Cs^+ analysis.

Table 1. Crystallographic data for **1**.

Molecular formula	$\text{K}_3\text{Rb}_3\text{Zn}_4\text{Sn}_3\text{Se}_{13}$
Molecular weight	2017.74
Color and habit	orange, trigonal
Crystal size	$0.15 \times 0.15 \times 0.15 \text{ mm}^3$
Crystal system	Trigonal
Space group	$R\bar{3}m$ (No.160)
Unit cell parameters	$a = 14.650(2) \text{ \AA}$ $c = 15.744(3)$ $V = 2926.0(3) \text{ \AA}^3$ $Z = 3$
$F(000)$	2640
Density (calcd)	3.435 g/cm^3
Diffractionmeter	Enraf-Nonius CAD4
Radiation	Graphite-monochromatized Mo $\text{K}\alpha\lambda = 0.71073 \text{ \AA}$
Refs. used for cell measurement	$25, 6.21^\circ \leq \theta \leq 1.77^\circ$
Standard reflections	$(3, -1, -1); (3, -4, 3); (1, 4, 1)^R$
Intensity variation	$\pm 5.1 \%$
Absorption coefficient	20.468 mm^{-1}
Transmission factor	0.4221 -0.9996
Scan type and rate	ω scan
Scan range	$(0.70 + 0.35 \tan \theta)^\circ$
Data collection range	$-18 \leq h \leq 12; -17 \leq k \leq 18; -19 \leq l \leq 15; 2.06^\circ \leq \theta \leq 25.98^\circ$ $0 \leq h \leq 12; -12 \leq k \leq 12; -12 \leq l \leq 12^R$ (in rhombohedral axes)
R_{int} (from merging of equiv. refls.)	0.124
Reflections measured	
total:	3840
unique (n):	1245
Observed [$I \geq 2\sigma(I)$]:	962
No. of variables, p	53
Extinction coefficient	0.00023(5)
Weighting scheme	$w = 1/[\sigma^2(F_o^2) + (0.04P)^2 + 90.0 P]$, $P = (F_o^2 + 2F_c^2)/3$
$R1^a$	0.0810 (all data) 0.0515 (observed data)
$wR2^b$	0.1352 (all data) 0.1218 (observed data)
Goodness-of-fit on F^2	1.179
Largest and mean Δ/σ	0.001, 0.000
Largest peak and hole	+1.989 to $-1.314 e \text{ \AA}^{-3}$

$$^a R1 = \frac{\sum ||F_o| - |F_c||}{\sum |F_o|}, \quad ^b wR2 = \sqrt{\frac{\sum [w(F_o^2 - F_c^2)^2]}{\sum w(F_o^2)^2}}, \quad ^c \text{Goof} = S = \sqrt{\frac{\sum [w(F_o^2 - F_c^2)^2]}{n - p}}$$

Table 2. Atomic coordinates and equivalent isotropic temperature factors* (\AA^2) for **1**.

Atoms	x	y	z	Ueq	Wyckoff letter and site position
Sn	0.1489(1)	0.2978(1)	0.7281(1)	0.024(1)	9 <i>b</i> , . <i>m</i>
Zn(1)	0.2393(1)	0.4786(2)	0.5299(2)	0.025(1)	9 <i>b</i> , . <i>m</i>
Zn(2)	0.3333	0.6667	0.3315(4)	0.021(1)	3 <i>a</i> , 3 <i>m</i>
Se(1)	0.4227(1)	0.8453(2)	0.2681(2)	0.030(1)	9 <i>b</i> , . <i>m</i>
Se(2)	0.3333	0.6667	0.4853(3)	0.019(1)	3 <i>a</i> , 3 <i>m</i>
Se(3)	0.2443(1)	0.4885(2)	0.6858(2)	0.028(1)	9 <i>b</i> , . <i>m</i>
Se(4)	-0.0040(2)	0.2787(2)	0.8144(2)	0.034(1)	18 <i>c</i> , <i>l</i>
K(1)	0.0184(4)	0.5092(2)	0.6646(4)	0.053(1)	9 <i>b</i> , . <i>m</i>
Rb(1)	0.0184(4)	0.5092(2)	0.6646(4)	0.053(1)	9 <i>b</i> , . <i>m</i>
K(2)	0.6488(4)	0.8244(2)	0.2903(4)	0.057(1)	9 <i>b</i> , . <i>m</i>
Rb(2)	0.6488(4)	0.8244(2)	0.2903(4)	0.057(1)	9 <i>b</i> , . <i>m</i>

* U_{eq} . defined as one third of the trace of the orthogonalized **U** tensor .

Table 3. Selected bond lengths (Å) and bond angles (°) for **1**.

Atoms	Bond length	Atoms	Bond angle
Sn-Se(1)#1	2.503(4)	Se(4)-Sn-Se(4)#2	113.38(14)
Sn-Se(3)	2.510(3)	Se(3)-Zn(1)-Se(4)#5	109.67(11)
Sn-Se(4)	2.512(2)	Se(3)-Zn(1)-Se(4)#6	109.67(11)
Sn-Se(4)#2	2.512(2)	Se(4)#5-Zn(1)-Se(4)#6	109.40(15)
Zn(1)-Se(3)	2.458(4)	Se(3)-Zn(1)-Se(2)	103.45(18)
Zn(1)-Se(4)#5	2.465(3)	Se(4)#5-Zn(1)-Se(2)	112.24(10)
Zn(1)-Se(4)#6	2.465(3)	Se(4)#6-Zn(1)-Se(2)	112.25(10)
Zn(1)-Se(2)	2.488(3)	Se(2)-Zn(2)-Se(1)#7	113.78(13)
Zn(2)-Se(2)	2.421(8)	Se(2)-Zn(2)-Se(1)	113.78(13)
Zn(2)-Se(1)#7	2.477(4)	Se(1)#7-Zn(2)-Se(1)	104.84(15)
Zn(2)-Se(1)	2.477(4)	Se(2)-Zn(2)-Se(1)#8	113.78(13)
Zn(2)-Se(1)#8	2.477(4)	Se(1)#7-Zn(2)-Se(1)#8	104.84(15)
Se(1)-Sn#9	2.503(4)	Se(1)-Zn(2)-Se(1)#8	104.84(15)
Se(2)-Zn(1)#8	2.488(3)	Zn(2)-Se(1)-Sn#9	103.37(16)
Se(2)-Zn(1)#7	2.488(3)	Zn(2)-Se(2)-Zn(1)#8	106.40(13)
Se(4)-Zn(1)#4	2.465(3)	Zn(2)-Se(2)-Zn(1)#7	106.40(13)
Se(1)-K(2)	3.494(5)	Zn(1)#8-Se(2)-Zn(1)#7	112.36(12)
Se(1)-K(2)#7	3.494(5)	Zn(2)-Se(2)-Zn(1)	106.40(13)
Se(3)-K(1)	3.486(5)	Zn(1)#8-Se(2)-Zn(1)	112.36(12)
Se(3)-K(1)#7	3.486(5)	Zn(1)#7-Se(2)-Zn(1)	112.36(12)
Se(4)-K(1)#4	3.601(5)	Zn(1)-Se(3)-Sn	102.46(14)
Se(4)-K(2)#3	3.639(6)	Zn(1)#4-Se(4)-Sn	104.45(10)
Se(4)-K(2)#10	3.924(4)	Se(1)#1-Sn-Se(3)	111.75(13)
K(1)-Se(3)#8	3.486(5)	Se(1)#1-Sn-Se(4)	111.87(7)
K(1)-Se(4)#6	3.601(5)	Se(3)-Sn-Se(4)	103.70(7)
K(1)-Se(4)#11	3.601(5)	Se(1)#1-Sn-Se(4)#2	111.87(7)
K(2)-Se(1)#8	3.494(5)	Se(3)-Sn-Se(4)#2	103.70(7)
K(2)-Se(4)#13	3.639(6)		
K(2)-Se(4)#14	3.639(6)		
K(2)-Se(4)#15	3.924(4)		
K(2)-Se(4)#13	3.924(4)		

Symmetry transformations used to generate equivalent atoms:

#1 $x-1/3, y-2/3, z+1/3$ #2 $-x+y, y, z$ #3 $-y+2/3, x-y+1/3, z+1/3$ #4 $-x+y-1/3, -x+1/3, z+1/3$
 #5 $x+1/3, x-y+2/3, z-1/3$ #6 $-y+1/3, x-y+2/3, z-1/3$ #7 $-y+1, x-y+1, z$ #8 $-x+y, -x+1, z$
 #9 $x+1/3, y+2/3, z-1/3$ #10 $x-2/3, y-1/3, z+2/3$ #11 $-y+1/3, -x+2/3, z-1/3$
 #12 $-x+y-1/3, -x+4/3, z+1/3$ #13 $-x+y+1/3, y+2/3, z-1/3$ #14 $-x+y+1/3, -x+2/3, z-1/3$
 #15 $x+2/3, x-y+4/3, z-2/3$ #16 $-y+4/3, x-y+5/3, z-1/3$

3.2. Results and Discussion

Single crystal X-ray diffraction study revealed that the title compound is a three dimensional structure. Crystal data for compound **1**: Space Group R3m (No.160), $a = 14.650(2)$, $c = 15.744(3)$ Å, $V = 2926.0(3)$ Å³, $Z = 3$, $d_{\text{calcd}} = 3.435$ g·cm⁻³, μ (Mo K α) = 20.468 mm⁻¹. The basic building block in this structure is a $[\text{Zn}_4\text{Sn}_3\text{Se}_{16}]^{12-}$ cluster which consists of four ZnSe_4 and three SnSe_4 tetrahedra connected through corner-sharing Se atoms as shown in Fig. 11(a). The cluster $[\text{Zn}_4\text{Sn}_3\text{Se}_{16}]^{12-}$ possesses a C_{3v} symmetry with its three-fold axis and mirror plane passing through Se(2) and Zn(2). Each cluster is linked to six others by sharing terminal Se(3) atoms to form a three-dimensional network of the formula $3_{\infty}[\text{Zn}_4\text{Sn}_3\text{Se}_{13}]^{6-}$, as shown in Fig. 11(b). The 3D network contains intersecting channels running parallel to the crystallographic $[211]$, $[1-1-1]$ and $[12-1]$ directions. The channels have an irregular cross section with a size of approximately 7.7×6.4 Å. The disordered K^+ and Rb^+ cations reside in these channels. There are two kinds of Se coordination modes: μ_2 -Se and μ_4 -Se. The average Sn-Se distance is 2.508 Å, and the average Zn-Se distance, 2.469 Å. The bond angles of Se-Sn-Se and Se-Zn-Se fall in a narrow range of 103.70° to 113.38°, and 103.37° to 113.78°, respectively, so both $[\text{SnSe}_4]^{4-}$ and $[\text{ZnSe}_4]^{4-}$ are close to an ideal tetrahedron, very similar to a reported open-framework compound containing $[\text{MSe}_4]^{4-}$ ($\text{M} = \text{Sn}, \text{Cd}$).¹⁹ The pore volume (excluding alkali metals) was calculated to be 1284.5 Å³, around 43.9% of the crystal volume within a unit cell.

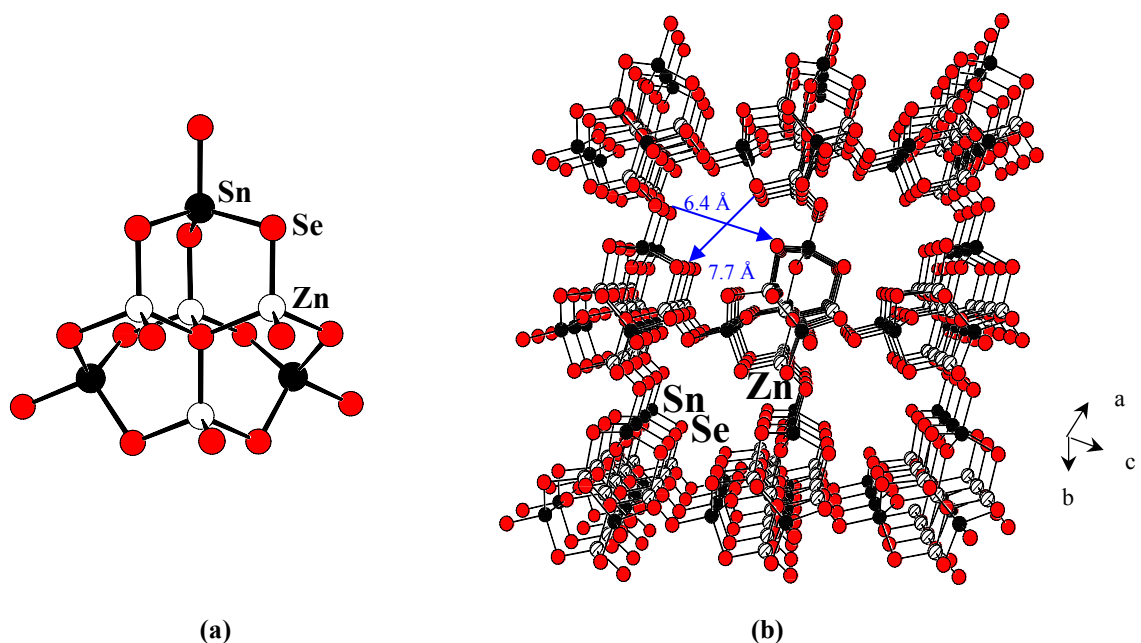


Figure 11. (a) Building block $[\text{Zn}_4\text{Sn}_3\text{Se}_{16}]^{12-}$; (b) View of the 3D network of **1** along $[12-1]$.

Powder samples were successfully prepared for ion exchange and optical absorption experiments. Figure 12 shows the powder X-ray diffraction pattern of **1**, which matches very well with the simulated pattern generated from single crystal data, indicating a high purity of the samples. Cation exchange of disordered Rb^+/K^+ by Cs^+ ions was carried out at 50°C for 7h under N_2 protection ($\text{Cs}^+:\text{Rb}^+/\text{K}^+ = 30:1$ mole ratio). The product was washed with distilled water 6 times. Microprobe Analysis showed Rb^+ and K^+ were exchanged partially. ICP-AES elemental analysis indicated 15.8 % of the Cs^+ in the structure.

Optical diffuse reflectance experiments were carried out at room temperature and the result is shown in Figure 13. The optical adsorption spectrum gives a sharp absorption

edge at 2.6 eV, indicating that the title compound is a semiconductor with an intermediate band gap.

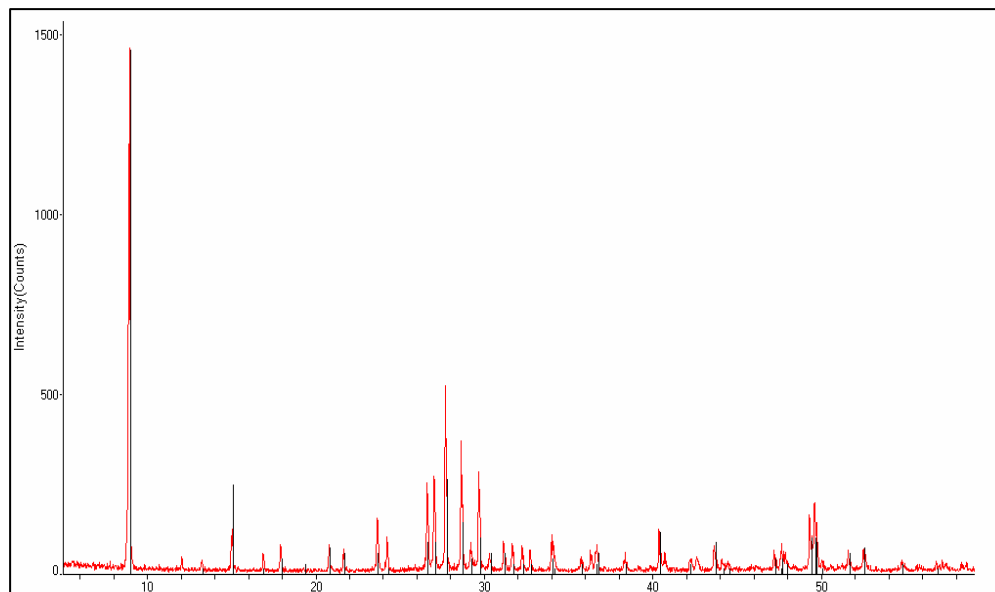


Figure 12. Powder X-ray diffraction pattern of **1** (red) shown along with simulated pattern from the single crystal data (black).

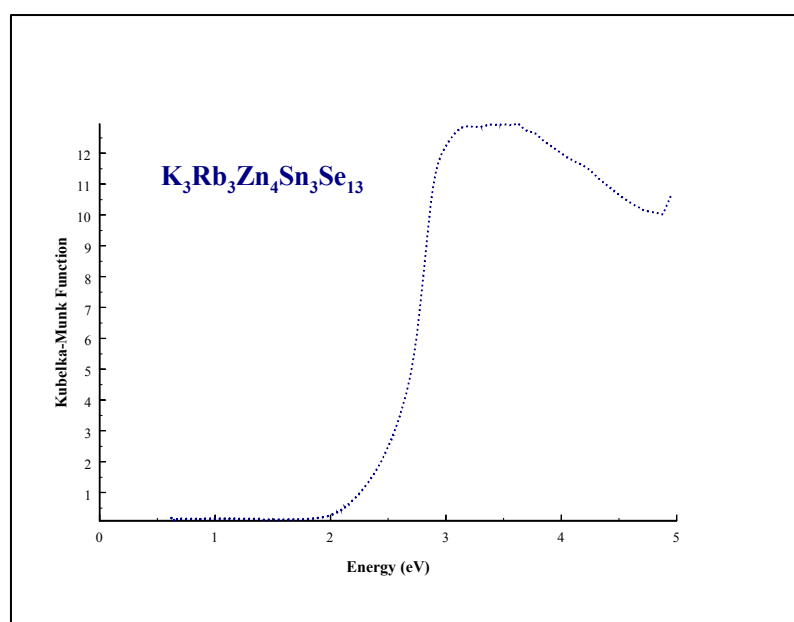


Figure 13. Optical absorption spectrum for **1**. Estimated band gap is 2.6 eV.

3.3. Conclusion

In summary, open-framework bimetallic chalcogenide compounds can combine semiconductor properties with other interesting functionality such as porosity in a single structure. There is a great potential to develop and to tailor these materials based on desired multifunctionality. Future investigation will focus on the design and synthesis of chalcogenides that make use of both electron charge and spin and are potentially important in optoelectronic devices and information storage.

CHAPTER FOUR

Synthesis, Structure and Properties of a 3D Open-Framework Quaternary Chalcogenide Built on a Bimetallic Tetrahedral Cluster $[\text{M}_4\text{Sn}_3\text{S}_{13}]^{5-}$ (M = Sn/Zn)

A multifunctional three-dimensional quaternary chalcogenide $[\text{Na}_5\text{Zn}_{3.5}\text{Sn}_{3.5}\text{S}_{13}]\cdot 6\text{H}_2\text{O}$ has been synthesized by solvothermal reactions. $[\text{Na}_5\text{Zn}_{3.5}\text{Sn}_{3.5}\text{S}_{13}]\cdot 6\text{H}_2\text{O}$ represents an interesting example of metal chalcogenides that combines semiconductivity, porosity, and light emission in a single structure. It crystallizes in the cubic space group $Fm-3c$, $a = 17.8630(3) \text{ \AA}$, $V = 5699.85(17) \text{ \AA}^3$, $Z = 8$. This compound is thermally stable up to 450°C . A band gap of 2.9 eV is estimated from the optical diffuse reflectance data. A strong photoluminescence peak is observed at 2.43 eV in Mn doped samples. The electronic and optical properties of this compound can be systematically tuned by substitution of metal and chalcogen elements.

4.1. Experimental Section

4.1.1. Crystal Growth and Sample Preparation

Single crystals of $[\text{Na}_5\text{Zn}_{3.5}\text{Sn}_{3.5}\text{S}_{13}]\cdot 6\text{H}_2\text{O}$ (**2**) were obtained in a reaction containing 0.50 mmol of Na_2S (anhydrous, Alfa Aesar), 0.80 mmol of S (powder, sublimed, Stream Chemicals), 0.25 mmol of Sn (powder, -325 mesh, 99.8%, Aldrich), and 0.017 mmol of ZnCl_2 (anhydrous, 98.7%, Fisher). The starting materials were pre-mixed and grinded, and then loaded in a 9 mm OD thick wall Pyrex tube. The sample was pre-heated at 90°C in programmable furnace for 1 hour and followed by addition of 0.20 mL CH_3OH (99.9%, Fisher) and 0.20 mL distilled H_2O . The reaction was heated at 150°C in furnace for 7 days. The products were washed with 80% alcohol followed by distilled water. Pale yellow cubic crystals and crystalline powders with around 27% yield were obtained.

A series of experiments were carried out to substitute Zn metal by Mn and S by Se in compound **2**. The Mn and Se concentrations were varied between 3% and 20% based on Zn and S respectively employing the same synthesis route as used for **2**.

4.1.2. Structure Characterization, Optical Absorption and Thermal Analysis

Single crystal X-ray diffraction of **2** was carried out on a Bruker-AXS smart APEX CCD diffractometer (Billerica, Massachusetts USA) with graphite-monochromated MoK α Radiation ($\lambda = 0.71073$ Å). All calculations were performed using the SHELXL-97 crystallographic software package. The data were collected at a temperature 100(2) K to a maximum θ value of 30.50°. Of a total of 14849 reflections collected, 738 were independent ($R_{\text{int}} = 0.0516$). The structure was solved by direct methods and expanded using Fourier techniques. The non-hydrogen atoms were refined anisotropically and the hydrogen atom was refined isotropically. The final cycle of full matrix least-squares refinement on F² was based on 738 observed reflections as well as 30 variable parameters and converged at $R_1 = 0.0261$. The unit cell parameters, along with data collection and refinement details, are listed in Table 4. Atomic coordinates and equivalent isotropic temperature factors are listed in Table 5. Shown in Table 6 are selected bond lengths (Å) and bond angles (°).

Table 4. Crystallographic data and structure refinement of **2**

Empirical formula	Na ₅ Zn _{3.5} Sn _{3.5} S ₁₃ (H ₂ O) ₆
Formula weight	1284.04
Crystal size (mm)	0.045 × 0.043 × 0.041
Temperature (K)	100
Crystal system	Cubic
Space group	<i>Fm-3c</i> (No.226)
Unit cell parameters (Å)	<i>a</i> = 17.8630(3)
<i>V</i> (Å ³)	5699.85(17),
<i>Z</i>	8
Calculated density (Mg/m ³)	2.993
<i>F</i> (000)	4824
Absorption coefficient (mm ⁻¹)	6.961
<i>λ</i> (Å)	0.71073
<i>θ</i> range for data collection (°)	2.28 to 30.50
Index ranges	-25 ≤ <i>h</i> ≤ 25, -25 ≤ <i>k</i> ≤ 25, -25 ≤ <i>l</i> ≤ 25
Reflections collected	14849
Independent reflections	738 [<i>R</i> (int) = 0.0516]
Completeness to <i>θ</i>	100.0 %
Refinement method	Full-matrix least-squares on <i>F</i> ²
Data / restraints / parameters	738 / 0 / 30
Goodness-of-fit on <i>F</i> ²	1.005
Final <i>R</i> indices [<i>I</i> > 2σ(<i>I</i>)]	<i>R</i> 1 = 0.0261, <i>wR</i> 2 = 0.0583
Absolute structure parameter	0.07(3)
<i>R</i> indices (all data)	<i>R</i> 1 = 0.0278, <i>wR</i> 2 = 0.0595
Largest diff. peak and hole (e/Å ³)	0.674 and -0.503

Table 5. Atomic coordinates ($\times 10^4$) and equivalent isotropic displacement parameters ($\text{\AA}^2 \times 10^3$) for **2**

Atoms	x	y	z	U_{eq}
Sn(1)	0	5000	2500	11(1)
M(2)*	764(1)	5764(1)	764(1)	11(1)
Na(1)	3538(1)	6462(1)	1462(1)	26(1)
S(1)	78(1)	6146(1)	1808(1)	8(1)
S(2)	0	5000	0	14(1)
Na(2)	2500	7500	2500	23(1)
O(1)	3822(2)	7500	2500	18(1)
H(1)	4040(40)	7840(40)	2240(40)	38(19)

U_{eq} is defined as one third of the trace of the orthogonalized U^{ij} tensor.

* M = 0.125 Sn + 0.875 Zn

Table 6. Selected bond lengths (Å) and angles (°) for **2**

Atoms	Bond length	Atoms	Bond length
Sn(1)-S(1)	2.3951(9)	Na(1)-S(1)#10	2.875(2)
Sn(1)-S(1)#1	2.3952(9)	S(1)-Na(1)#11	2.875(2)
Sn(1)-S(1)#2	2.3952(9)	S(2)-M(2)#12	2.3648(8)
Sn(1)-S(1)#3	2.3952(9)	S(2)-M(2)#1	2.3648(8)
M(2)-S(1)#4	2.3331(9)	S(2)-M(2)#13	2.3648(8)
M(2)-S(1)#5	2.3331(9)	Na(2)-O(1)	2.361(4)
M(2)-S(1)	2.3331(9)	Na(2)-O(1)#6	2.362(4)
M(2)-S(2)	2.3647(8)	Na(2)-O(1)#4	2.362(4)
Na(1)-O(1)	2.671(3)	Na(2)-O(1)#7	2.362(4)
Na(1)-O(1)#6	2.671(3)	Na(2)-O(1)#5	2.362(4)
Na(1)-O(1)#7	2.671(3)	Na(2)-O(1)#14	2.362(4)
Na(1)-S(1)#8	2.875(2)	O(1)-Na(1)#15	2.671(3)
Na(1)-S(1)#9	2.875(2)	O(1)-H(1)	0.86(7)
Atoms	Bond angle	Atoms	Bond angle
S(1)-Sn(1)-S(1)#1	117.86(4)	M(2)-S(1)-Sn(1)	101.15(3)
S(1)-Sn(1)-S(1)#2	105.45(2)	M(2)-S(1)-Na(1)#11	112.83(7)
S(1)#1-Sn(1)-S(1)#2	105.45(2)	Sn(1)-S(1)-Na(1)#11	102.89(3)
S(1)-Sn(1)-S(1)#3	105.45(2)	M(2)-S(2)-M(2)#12	109.5
S(1)#1-Sn(1)-S(1)#3	105.45(2)	M(2)-S(2)-M(2)#1	109.5
S(1)#2-Sn(1)-S(1)#3	117.86(4)	M(2)#12-S(2)-M(2)#1	109.5
S(1)#4-M(2)-S(1)#5	109.87(3)	M(2)-S(2)-M(2)#13	109.5
S(1)#4-M(2)-S(1)	109.87(3)	M(2)#12-S(2)-M(2)#13	109.5
S(1)#5-M(2)-S(1)	109.87(3)	M(2)#1-S(2)-M(2)#13	109.5
S(1)#4-M(2)-S(2)	109.07(3)	O(1)-Na(2)-O(1)#6	90.0
S(1)#5-M(2)-S(2)	109.07(3)	O(1)-Na(2)-O(1)#4	90.0
S(1)-M(2)-S(2)	109.07(3)	O(1)#6-Na(2)-O(1)#4	180.0
O(1)-Na(1)-O(1)#6	77.37(17)	O(1)-Na(2)-O(1)#7	90.0
O(1)-Na(1)-O(1)#7	77.37(17)	O(1)#6-Na(2)-O(1)#7	90.0

Atoms	Bond angle	Atoms	Bond angle
O(1)#6-Na(1)-O(1)#7	77.37(17)	O(1)#4-Na(2)-O(1)#7	90.0
O(1)-Na(1)-S(1)#8	78.78(9)	O(1)-Na(2)-O(1)#5	90.000(1)
O(1)#6-Na(1)-S(1)#8	118.53(4)	O(1)#6-Na(2)-O(1)#5	90.0
O(1)#7-Na(1)-S(1)#8	147.27(5)	O(1)#4-Na(2)-O(1)#5	90.0
O(1)-Na(1)-S(1)#9	118.53(4)	O(1)#7-Na(2)-O(1)#5	180.0
O(1)#6-Na(1)-S(1)#9	147.27(5)	O(1)-Na(2)-O(1)#14	180.0
O(1)#7-Na(1)-S(1)#9	78.78(9)	O(1)#6-Na(2)-O(1)#14	90.000(1)
S(1)#8-Na(1)-S(1)#9	93.46(10)	O(1)#4-Na(2)-O(1)#14	90.0
O(1)-Na(1)-S(1)#10	147.27(5)	O(1)#7-Na(2)-O(1)#14	90.000(1)
O(1)#6-Na(1)-S(1)#10	78.78(9)	O(1)#5-Na(2)-O(1)#14	90.0
O(1)#7-Na(1)-S(1)#10	118.53(4)	Na(2)-O(1)-H(1)	117(5)
S(1)#8-Na(1)-S(1)#10	93.46(10)	Na(1)#15-O(1)-H(1)	88(5)
S(1)#9-Na(1)-S(1)#10	93.46(10)	Na(1)-O(1)-H(1)	102(5)

Symmetry transformations used to generate equivalent atoms:

#1 -x,-y+1,z #2 y-1/2,-x+1/2,-z+1/2 #3 -y+1/2,x+1/2,-z+1/2 #4 y-1/2,z+1/2,x
 #5 z,x+1/2,y-1/2 #6 -y+1,z+1/2,-x+1/2 #7 z,-x+1,-y+1 #8 x+1/2,z+1/2,y-1/2 #9 -
 y+1,-x+1/2,z+0 #10 -z+1/2,y+0,-x+0 #11 -y+1/2,-x+1,z+0 #12 x,-y+1,-z #13 -x,y,-
 z #14 -x+1/2,-y+3/2,z #15 x,-y+3/2,-z+1/2 #16 -x+1/2,y,-z+1/2

The phase purity of all samples was analyzed by powder X-ray diffraction using a Rigaku D/M-2200T automated diffraction system (Ultima+). The measurements were made with a 2θ range between 3 and 70° at the operation power of 40 KV/40 mA. The band gaps of **2** and all substituted samples were assessed by optical diffuse reflectance experiments at room temperature. All measurements were made on a Shimadzu UV-3101PC double beam, double monochromated spectrophotometer in the range of 250-

2000 nm. Thermogravimetric analysis (TGA) was carried out on a TA Instrument Q50 (New Castle, Delaware USA). Differential scanning calorimetry (DSC) experiments were performed on a TA Instrument Q100 (New Castle, Delaware USA) from room temperature to 500 °C with a ramp rate of 10°C/min.

4.1.3. Photoluminescence Spectroscopy

Photoluminescence (PL) was measured at room temperature with a SPEX 1403 spectrometer (Metuchen, New Jersey USA), RCAC31034 GaAs PMT, and the 325 nm line of a He-Cd laser with ~ 5mW power.

4.1.4 Solvent Exchange Experiments

In order to evaluate the exchange capability of the solvent molecules in the pores, experiments were carried out to exchange water with dimethyl sulfoxide. The samples were heated by TGA to remove all water molecules inside the pores while keeping the framework structure intact. After TGA, the samples were analyzed by powder X-ray diffraction and followed by addition of water and dimethyl sulfoxide respectively. The samples were placed in these solvents and heated at ~60°C for a few hours and then left at room temperature for 2 days. The final products were washed with ethyl ether several times and dried in the air. PXRD and TGA were carried out again with the same procedure as before. All the TGA in solvent exchange experiments were performed from room temperature to 350°C with ramp rate 5°C/min and kept isothermal at 350°C for 30 minutes under nitrogen.

4.2. Results and Discussion

The building block of the 3D $[\text{Na}_5\text{Zn}_{3.5}\text{Sn}_{3.5}\text{S}_{13}]\cdot 6\text{H}_2\text{O}$ (**2**) structure is a bimetallic

cluster $[M_4Sn_3S_{13}]^{5-}$, which consists of four MS_4 ($M = 0.125 \text{ Sn} + 0.875 \text{ Zn}$) tetrahedra that share a corner of S atom at the core, and $6 \times \frac{1}{2}$ terminal SnS_4 tetrahedra. Two of the S atoms in each SnS_4 tetrahedron are corner-shared with two MS_4 tetrahedra within the same cluster while the other two S atoms link to two MS_4 tetrahedra in the adjacent cluster by corner-sharing. The building block can also be conveniently written as $[(SM_4)(SnS_4)_{6/2}]$ or $[M_4Sn_3S_{13}]^{5-}$, since its core can be considered as a SM_4 tetrahedron⁵³, and since each of the six outer SnS_4 tetrahedra is shared with an adjacent cluster (Figure 14a). Each cluster is linked to six adjacent clusters through an S-S edge of SnS_4 tetrahedra in *a*, *b*, *c* directions, respectively, to form a three-dimensional network structure. The 3D network of **2** contains open channels running through all three directions (Figure 14b). The smallest cross section of the channels measured approximately $5.4 \times 5.4 \text{ \AA}$ (between the centers of sulfur atoms). There are two crystallographically independent Na atoms. Each of the four Na(1) atoms are located at the corner of channels surrounded by three H_2O molecules in the channel and three S atoms from the framework. The Na(2) atom is found in the center of the channel with six surrounding H_2O molecules forming an octahedron (Figure 14c). The pore volume (when excluding Na^+ and H_2O) was calculated to be 1613.9 \AA^3 using the SOLV routine in PLATON⁵⁴, around 28.3% of the volume within a unit cell.

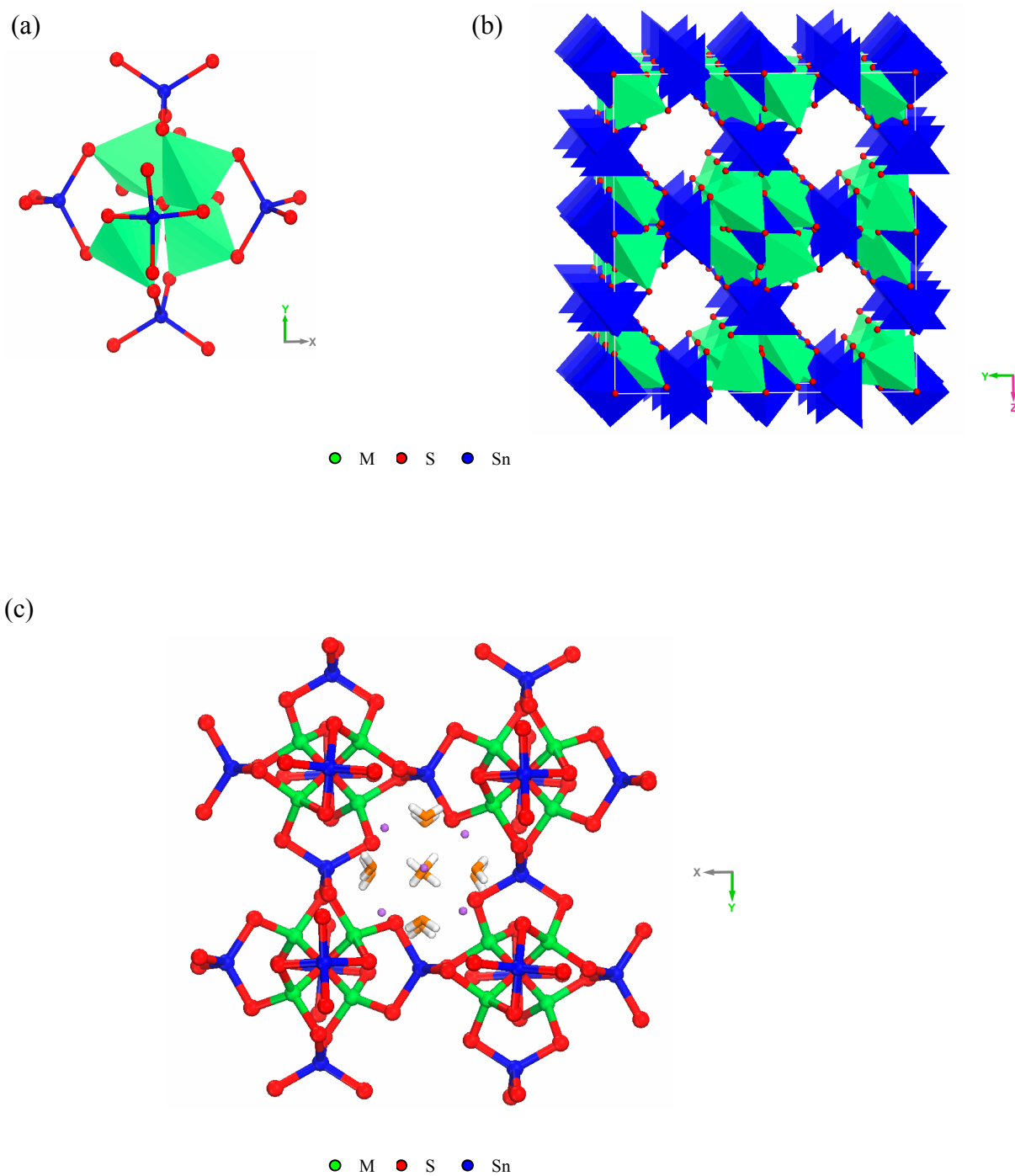


Figure 14. (a) $\text{SM}_4(\text{SnS}_4)_6$ cluster ($\text{M} = \text{Zn, Sn}$) (b) View of the 3D network without Na cations and H_2O molecules (c) Highly symmetric pore with Na cations (purple) and H_2O molecules.

Figure 15 shows the similarities and differences of the $[\text{M}_4\text{Sn}_3\text{S}_{13}]^{5-}$ ($\text{M} = 0.125 \text{ Sn} + 0.875 \text{ Zn}$) building unit of **2** in comparison with $[\text{M}'_4\text{Sn}_3\text{Se}_{13}]^{6-}$ ($\text{M}' = \text{Zn}^{23}, \text{Hg}^{55}$) in $\text{K}_3\text{Rb}_3\text{Zn}_4\text{Sn}_3\text{Se}_{13}$ and $\text{K}_6\text{Hg}_4\text{Sn}_3\text{Se}_{13} \cdot \text{MeOH}(\text{H}_2\text{O})_3$. There are two crystallographically independent Zn/Hg sites for the four inner ZnSe_4 or HgSe_4 tetrahedra, while the four inner MS_4 tetrahedra in the $[\text{M}_4\text{Sn}_3\text{S}_{13}]^{5-}$ cluster are identical. The $[\text{M}_4\text{Sn}_3\text{S}_{13}]^{5-}$ cluster possess higher T_d symmetry, while the symmetry is a lower C_{3v} for $[\text{Zn}_4\text{Sn}_3\text{Se}_{13}]^{6-}$ and $[\text{Hg}_4\text{Sn}_3\text{Se}_{13}]^{6-}$ clusters. Each of the three surrounding SnSe_4 tetrahedra in $[\text{Zn}_4\text{Sn}_3\text{Se}_{13}]^{6-}$ corner shares Se of three ZnSe_4 tetrahedra in the core, leaving one Se atom corner-shared by another ZnSe_4 tetrahedron from the adjacent cluster, while in $[\text{M}_4\text{Sn}_3\text{S}_{13}]^{5-}$ each of the three surrounding SnS_4 tetrahedra corner shares S of two MS_4 tetrahedra in the core, leaving two S atoms corner-shared by another MS_4 tetrahedron from the adjacent cluster.

This light yellow **2** is stable in air and water. The thermal stability was studied via thermogravimetric analysis (TGA) conducted on pure polycrystalline samples. Figure 16a shows the TGA profile with a ramp rate of $15^\circ\text{C}/\text{min}$ from room temperature to 700°C under nitrogen. The sample began to lose water molecules at $\sim 150^\circ\text{C}$ and completed the process at $\sim 350^\circ\text{C}$ with a total loss of 8.1%, in reasonable agreement with the calculated value of 8.4%. The compound decomposed around 450°C . The high thermal stability may be due to high framework symmetry and the higher charged Sn^{4+} metal sites which provide sufficient bond valences to balance the edge or corner S^{2-} anions.¹⁵ DSC shows a large endothermic peak at 350°C that may associates with the water loss (Figure 16b). Powder X-ray diffraction was performed immediately after heating up to 350°C for 1 hour. Clearly there are changes in the X-ray pattern, indicating

a phase change. There is also a change in the band gap of the heated sample, giving a lowered band gap of 2.6eV.

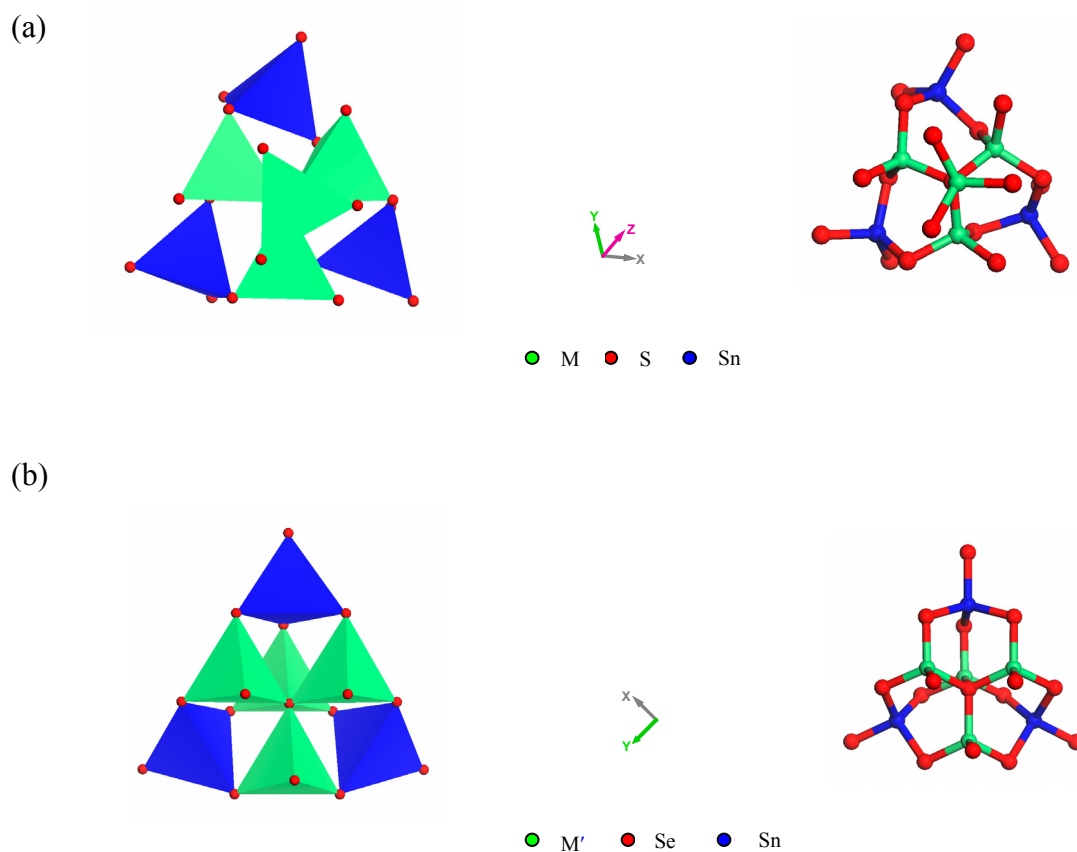


Figure 15. (a) Building block of $[M_4Sn_3S_{13}]^{5-}$ ($M = 0.125Sn + 0.875Zn$) in **2**; (b) Building block of $[M'_4Sn_3Se_{13}]^{6-}$ ($M' = Zn, Hg$) in $K_3Rb_3Zn_4Sn_3Se_{13}$ and $K_6Hg_4Sn_3Se_{13} \cdot MeOH(H_2O)_3$.

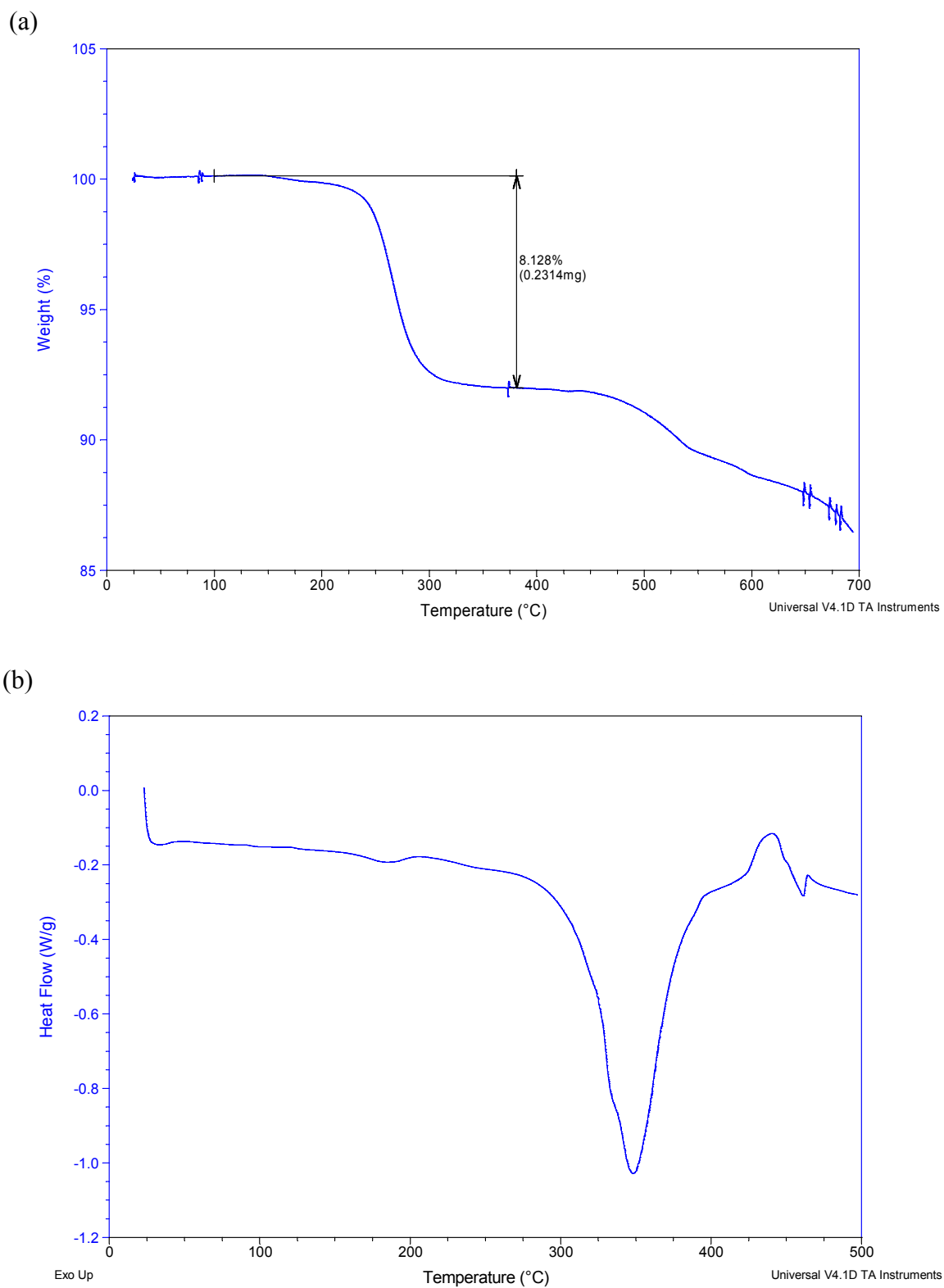


Figure 16. (a) TGA profile and (b) DSC plot for compound **2**.

One way to tune the electronic and optical properties of materials is by alloying or doping/substitution. We investigated substitution effects by replacing Zn with Mn and S with Se. No phase separation was observed in the concentration range of 3-20% based on the powder X-ray analysis. The PXRD patterns of the substituted samples are shown in Figure 17. The optical properties were studied by measuring the room temperature diffuse reflectance of **2** as well as Mn and Se substituted samples. The optical spectra of **2**, along with Mn and Se substituted samples are plotted in Figure 18a and 18b, respectively. The sharp absorption edge was observed at ~ 2.9 eV for **2**. As the concentration of Se and Mn was increased, a red shift in the band gap was achieved, as expected based on the atomic properties of the substituents. For Se doped samples, the band gap varies smoothly and can be well defined as in II-VI semiconductor alloys involving S and Se. Figure 19 shows a nice linear relationship of the band gap energy as a function of Se concentration. However, for the Mn doped samples, because Mn is strongly mismatched with the host element Zn, the doping leads to the red shift of the host band gap. It also generates an impurity state below the band gap which eventually evolves into a new absorption band (a small lump at around 2.0 eV) that merges with the perturbed host absorption band. The effect of Mn doping is at least to some extent similar to that in other systems of isoelectronic doping.⁵⁶

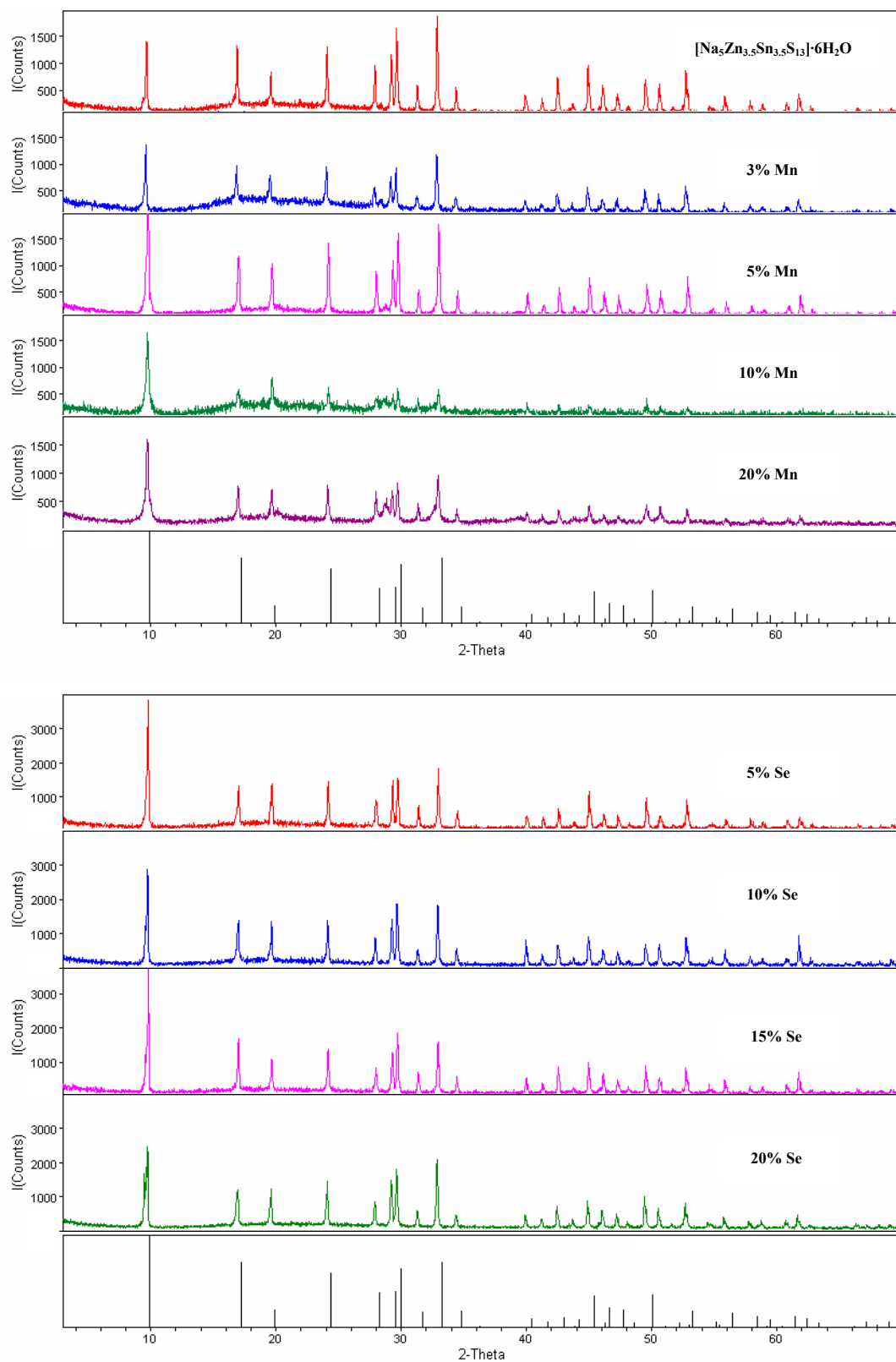
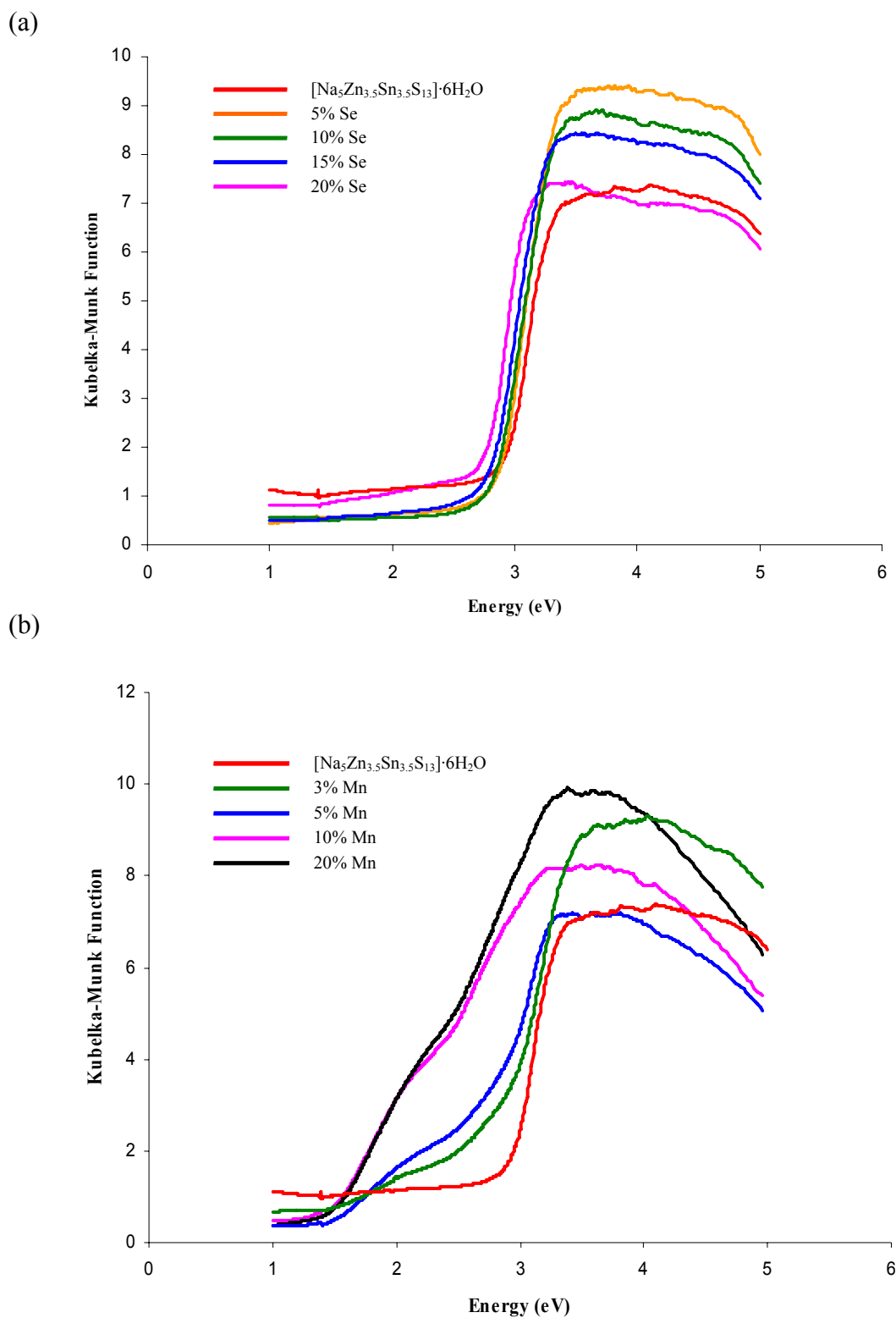


Figure 17. Powder X-ray diffraction patterns of $[\text{Na}_5\text{Zn}_{3.5}\text{Sn}_{3.5}\text{S}_{13}] \cdot 6\text{H}_2\text{O}$ and Mn, Se substituted compounds with the substituent concentration between 3% and 20%. (black lines: simulated pattern from the single crystal data)



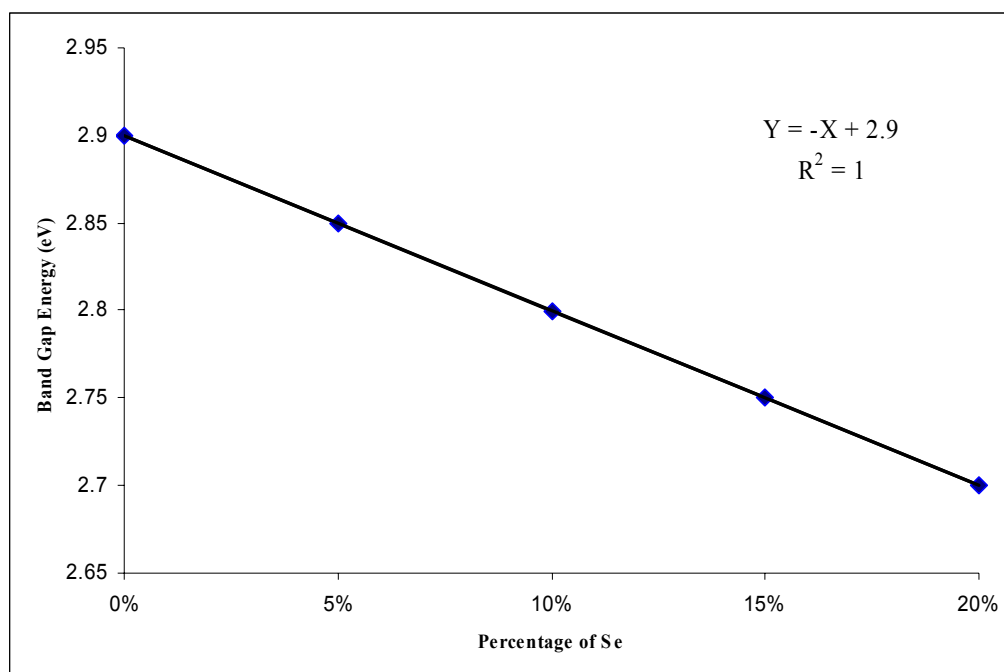


Figure 19. Band gap energy as a function of Se concentration in **2**.

Figure 20 shows the TGA results before and after solvent exchange with dimethyl sulfoxide (DMSO). Figure 20(a) indicated all water molecules inside the channels were removed with a weight loss around 7.9% (above 100°C). The weight loss below 100°C was primarily from the solvents on the surface. Another TGA was carried out on the sample after being immersed in DMSO, and removed the excess DMSO on the surface by washing with ethyl ether several times. The second TGA (Figure 20(b)) gave 4.9% weight loss, which indicated ~1 DMSO molecule replacing 6 H₂O molecules inside the pores. Powder X-ray diffraction showed the structure remained the same before and after TGA (Figure 21). Water restoration experiment was performed as well with the same procedure. It gave around 4% weight loss from 100°C, which indicated the H₂O molecules can partially go back into the open channels.

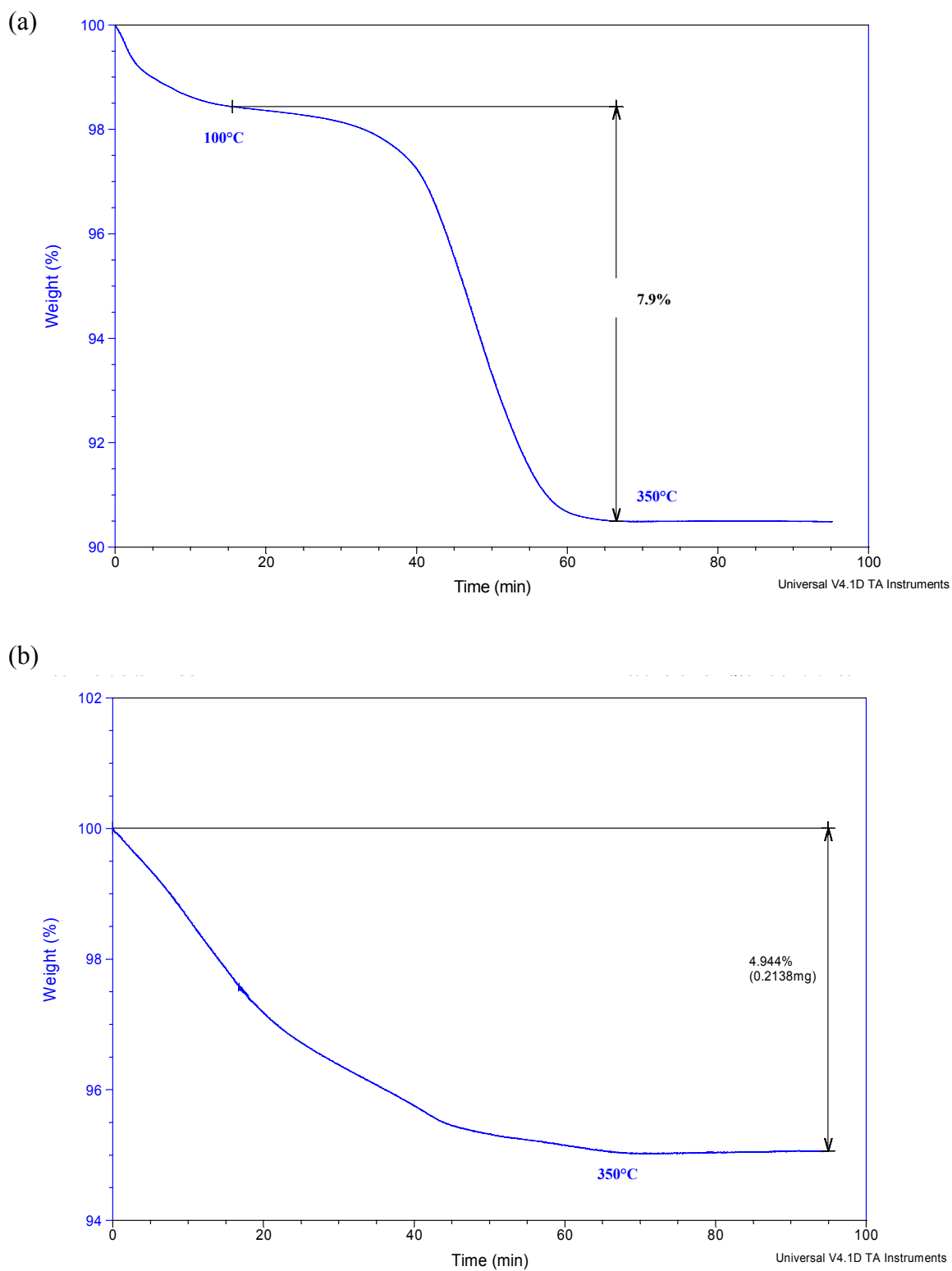
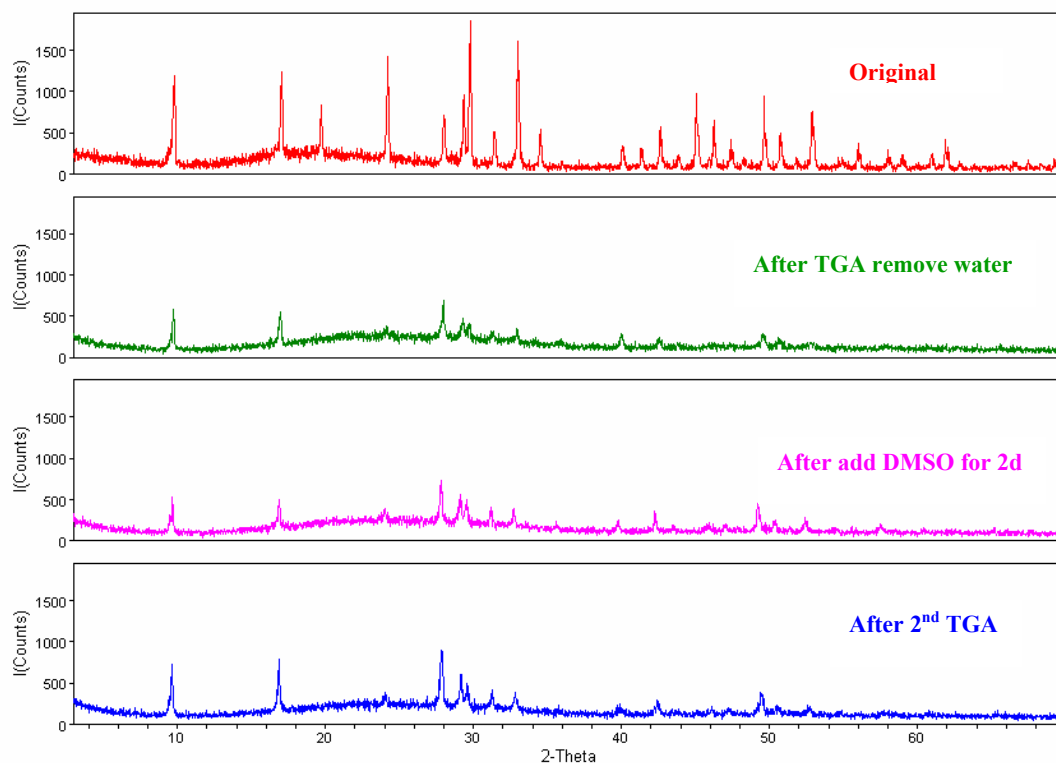


Figure 20. (a) TGA profile showing removal of water molecules in the channels. (b) TGA profile after the exchange by DMSO. A weight loss of 4.9 % was observed.



Rutgers University - Camden

x5.mw> Tuesday, Dec 11, 2007 10:12:54a

Figure 21. Powder X-ray patterns for DMSO solvent exchange experiments

Figure 22 shows the PL spectra of **2** with Mn concentration varying from 0 to 20%, measured at room temperature. The powder was held in a quartz vial. The emission of 0% sample is very weak. With increasing Mn concentration, a PL band at 2.03-2.04 eV appears and its intensity increases continuously. The peak energy is consistent with that of Mn content in II-VI semiconductors, and the energy is insensitive to the host⁵⁷. The emission above the Mn related band seems to also enhance with increasing Mn doping level. The origin is unclear, but could be defect related, which deserves further investigation.

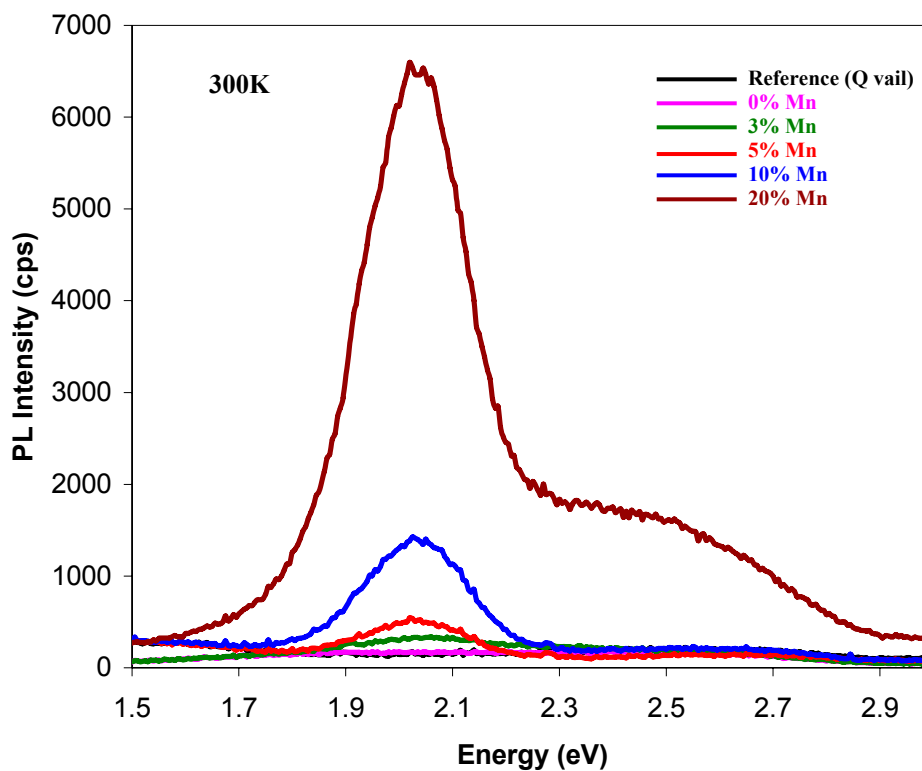


Figure 22. Room temperature photoluminescence of Mn doped $[\text{Na}_5\text{Zn}_{3.5}\text{Sn}_{3.5}\text{S}_{13}]\cdot 6\text{H}_2\text{O}$ with varying Mn concentration.

4.3. Concluding Remarks

In summary, a new open-framework quaternary metal chalcogenide compound $[\text{Na}_5\text{Zn}_{3.5}\text{Sn}_{3.5}\text{S}_{13}]\cdot 6\text{H}_2\text{O}$ built on an bimetallic tetrahedral cluster $[\text{M}_4\text{Sn}_3\text{S}_{13}]^{5-}$ ($\text{M} = 0.125\text{Sn} + 0.875\text{Zn}$), has been synthesized and characterized. The compound combines semiconductor properties with other interesting functionality such as porosity in a single structure. The successful doping/substitution of Mn and Se allows systematic tuning of the band gap and optical properties of this semiconductor compound. The relatively large

band gap (~ 3 eV) makes it a promising candidate as a transparent conducting material, if either n- or p-type doping should be shown feasible. Since it is a non-oxide large band gap material, it is of particular interest for the application as a p-type transparent conducting material. The study of solvent exchange indicates that the guest molecules in the open pores can be easily taken out and restored without changing the framework structure. This work provides useful information for the future design and synthesis of new metal chalcogenides with desired multifunctionality.

CHAPTER FIVE

**Novel Iron-Sulfur Material with Unique 2D Anionic [Fe₁₆S₂₀] Layered
structure: Synthesis, Structure and Properties**

Since its introduction^{58, 59}, spontaneous self-assembly of iron-sulfur clusters containing the cores such as $[\text{Fe}_2\text{S}_2]^{2+}$ ^{60, 61}, linear $[\text{Fe}_3\text{S}_4]^{1+}$ ⁶¹, cubic $[\text{Fe}_4\text{S}_4]^{2+}$ ^{58, 60, 62, 63} and prismatic $[\text{Fe}_6\text{S}_6]^{3+, 2+}$ ⁶⁴ have been well studied, especially for magnetic and biological applications. All of these studies were based on molecular clusters with zero dimensions. 2D Layered chalcogenides with both iron and copper sulfide $[\text{CuFeS}_2]^{1-}$ in ACuFeS_2 ($\text{A}=\text{Li, Na, K, Rb, Cs}$)⁶⁵⁻⁶⁹ have been reported as well. Both Cu and Fe ions are randomly distributed at tetrahedral sites. So far there are no 2D layered structures constructed by only iron-sulfur reported. In this study we have synthesized the first novel iron-sulfur material built with unique anionic $[\text{Fe}_{16}\text{S}_{20}]^{4-}$ Layers. Diffuse reflectance spectrum of the sample showed a very low absorption coefficient and a small band gap $\sim 0.5\text{eV}$. Doping/substitution experiments with Co and Mn replacing Fe were carried out and the properties will be discussed.

5.1. Experimental Section

5.1.1. Crystal Growth and Sample Preparation

The synthesis of layered ion sulfide material $[\text{Fe}(\text{en})_3]_2 \cdot [\text{Fe}_{16}\text{S}_{20}] \cdot \text{en}$ (**3**) involved mixing of FeCl_2 (0.50 mmol, 99.5%, Alfa Aesar), dimethylsulfoxide (DMSO) (71 μl , 1.0 mmol, 99.9%, Acros Organics) and ethylenediamine (8.0 ml, 99%, Acros Organics) in a Teflon-lined stainless steel autoclave. The mixture was stirred for 10 minutes and the vessel was then sealed and heated at 200°C in furnace for 7 days. The autoclave was subsequently allowed to cool to room temperature. The product was filtered off, washed with 80% ethanol and distilled water. The pure black plate-like crystals were obtained. A series of experiments were carried out to substitute Fe atoms by Co or Mn. The Co and

Mn concentrations were varied between 3% and 100% based on Fe respectively employing the same synthesis route.

Fe(III)(en)₃Cl₃ compound for X-ray absorption analysis was prepared by adding slowly and stirring anhydrous Fe(III)Cl₃ (1.0 mmol, anhydrous, 98%, Stream) dissolved in 6.0 ml absolute ethanol, followed by 1 ml ethylenediamine (8.0 ml, 99%, Acros Organics) in a teflon autoclave.⁷⁰ The reaction was heated at 50°C in furnace for 6 hours and the pale green-colored solids was filtered, washed with ether, and dried under Ar protection. The dry solids are stable for weeks in glove-box under N₂.

5.1.2. Structure Characterization, Optical Absorption and Thermal Analysis

Single crystal X-ray diffraction of **3** was carried out on a Bruker-AXS smart APEX CCD diffractometer with graphite-monochromated MoK α Radiation ($\lambda = 0.71073$ Å). All calculations were performed using the SHELXL-97 crystallographic software package. The data were collected at a temperature 100(2) K to a maximum θ value of 23.35°. Of a total of 39073 reflections collected, 8318 were independent ($R_{int} = 0.2169$). The structure was solved by direct methods and expanded using Fourier techniques. The final cycle of full matrix least-squares refinement on F^2 was based on 8318 observed reflections as well as 596 variable parameters and converged at $R_1 = 0.0690$. The unit cell parameters, along with data collection and refinement details, are listed in Table 7. Atomic coordinates and equivalent isotropic temperature factors are listed in Tables 8. Shown in Table 9 are selected bond lengths (Å) and bond angles (°).

Table 7. Crystallographic data and structure refinement for **3**

Empirical formula	[Fe(en) ₃] ₂ ·[Fe ₁₆ S ₂₀]·en
Formula weight	2067.23
Crystal size (mm)	0.31 x 0.04 x 0.005 mm
Temperature (K)	100(2)
Crystal system	Monoclinic
Space group	P2(1)/c (No.14)
Unit cell parameters (Å)	$a = 8.4028(15)\text{Å}$, $b = 33.278(6)\text{Å}$, $c = 20.490(4)\text{Å}$ $\alpha = 90^\circ$, $\beta = 90.276(3)^\circ$, $\gamma = 90^\circ$
V (Å ³)	5729.4(17)
Z	4
Calculated density (Mg/m ³)	2.397
$F(000)$	4160
Absorption coefficient (mm ⁻¹)	5.162
λ (Å)	0.71073
θ range for data collection (°)	1.84 to 23.35°
Limiting indices	$-9 \leq h \leq 9$, $-36 \leq k \leq 37$, $-22 \leq l \leq 22$
Reflections collected	39073
Independent reflections	8318 [R(int) = 0.2169]
Completeness to θ	99.8 %
Refinement method	Full-matrix least-squares on F^2
Data / restraints / parameters	8318 / 443 / 596
Goodness-of-fit on F^2	1.007
Final R indices [$I > 2\sigma(I)$]	$R1 = 0.0690$, $wR2 = 0.1240$
Absorption correction	Semi-empirical from equivalents
R indices (all data)	$R1 = 0.1873$, $wR2 = 0.1581$
Largest diff. peak and hole (e/Å ³)	1.913 and -2.068

Table 8. Atomic coordinates ($\times 10^4$) and equivalent isotropic displacement parameters ($\text{\AA}^2 \times 10^3$) for **3**

Atoms	x	y	z	U(eq)
Fe(1)	-1576(4)	2425(1)	-254(1)	10(1)
Fe(2)	-4645(4)	2089(1)	-244(1)	9(1)
Fe(3)	-5334(4)	2897(1)	-66(1)	9(1)
Fe(4)	-308(4)	1665(1)	-234(1)	9(1)
Fe(5)	1571(4)	2568(1)	-84(1)	9(1)
Fe(6)	-6539(4)	1180(1)	-46(1)	11(1)
Fe(7)	-5324(4)	406(1)	27(1)	8(1)
Fe(8)	328(4)	3340(1)	-48(1)	10(1)
Fe(9)	-8428(4)	85(1)	73(2)	10(1)
Fe(10)	330(4)	858(1)	-7(2)	9(1)
Fe(11)	-6589(4)	3665(1)	-16(1)	8(1)
Fe(12)	-3378(4)	1329(1)	-210(1)	9(1)
Fe(13)	-3438(4)	3829(1)	-156(1)	8(1)
Fe(14)	-363(4)	4151(1)	-118(2)	10(1)
Fe(15)	-4659(4)	4596(1)	-94(1)	9(1)
Fe(16)	-1576(4)	4914(1)	-63(1)	9(1)
S(1)	-3688(7)	2617(2)	-853(2)	10(1)
S(2)	-2478(7)	1888(2)	360(2)	8(1)
S(3)	-6336(7)	2367(2)	518(3)	13(1)
S(4)	-498(7)	2804(2)	542(3)	13(1)
S(5)	1336(7)	1398(2)	542(2)	10(1)
S(6)	510(7)	2185(2)	-880(2)	11(1)
S(7)	-7475(7)	3129(2)	-647(2)	11(1)
S(8)	-7487(6)	612(2)	-576(2)	8(1)
S(9)	-5425(7)	1550(2)	-854(2)	11(1)
S(10)	-4471(7)	955(2)	593(2)	10(1)
S(11)	-3647(7)	83(2)	-698(2)	11(1)
S(12)	-10540(7)	355(2)	655(2)	9(1)
S(13)	-4532(7)	3413(2)	586(2)	11(1)
S(14)	-1279(7)	1121(2)	-805(3)	11(1)
S(15)	-1335(7)	3653(2)	-775(2)	11(1)
S(16)	-8690(7)	3839(2)	610(2)	10(1)
S(17)	-2527(6)	4354(2)	496(2)	7(1)
S(18)	-5516(7)	4092(2)	-761(2)	9(1)
S(19)	507(7)	4692(2)	-709(2)	10(1)
S(20)	-6367(7)	4870(2)	657(2)	11(1)
Fe(17)	3403(4)	3299(1)	-2562(1)	11(1)
N(1)	1685(18)	3621(4)	-1922(7)	13(4)
C(1)	976(19)	3959(6)	-2278(8)	16(5)
C(2)	2310(20)	4184(5)	-2636(9)	29(6)
N(2)	3136(18)	3899(4)	-3056(7)	12(4)

Atoms	x	y	z	U(eq)
N(3)	5375(15)	3177(5)	-3246(6)	11(4)
C(3)	6820(20)	3359(7)	-2981(7)	25(6)
C(4)	6974(19)	3281(6)	-2265(7)	15(5)
N(4)	5537(15)	3421(5)	-1925(6)	15(4)
N(5)	3247(18)	2676(4)	-2138(7)	14(4)
C(5)	2250(20)	2425(5)	-2556(9)	17(5)
C(6)	861(19)	2664(6)	-2821(9)	21(6)
N(6)	1485(17)	3022(4)	-3168(6)	13(4)
Fe(18)	1654(4)	450(1)	-2477(1)	11(1)
N(7)	3385(18)	123(4)	-1829(6)	9(4)
C(7)	4000(20)	-227(6)	-2173(9)	24(6)
C(8)	2650(20)	-440(5)	-2521(8)	12(5)
N(8)	1822(19)	-162(4)	-2945(7)	14(4)
N(9)	3556(18)	738(4)	-3086(7)	14(4)
C(9)	4177(19)	1100(5)	-2751(9)	17(5)
C(10)	2790(20)	1331(5)	-2472(9)	13(5)
N(10)	1803(19)	1074(4)	-2061(7)	16(4)
N(11)	-477(16)	307(5)	-1856(7)	15(4)
C(11)	-1950(20)	407(9)	-2204(9)	53(9)
C(12)	-1790(20)	423(8)	-2913(8)	41(7)
N(12)	-285(16)	597(5)	-3147(6)	10(4)
N(13)	8290(30)	1497(8)	-3066(13)	102(11)
C(13)	8160(30)	1743(8)	-2512(11)	70(10)
C(14)	6890(30)	2059(7)	-2549(10)	52(8)
N(14)	6650(30)	2272(6)	-3141(9)	49(6)

U_{eq} is defined as one third of the trace of the orthogonalized U^{ij} tensor.

Table 9. Selected bond lengths (Å) and angles (°) for **3**

Atoms	Bond length	Atoms	Bond length
Fe(1)-S(1)	2.246(7)	Fe(6)-Fe(7)	2.776(5)
Fe(1)-S(4)	2.251(6)	Fe(6)-Fe(10)#1	2.843(5)
Fe(1)-S(2)	2.315(7)	Fe(7)-S(10)	2.279(6)
Fe(1)-S(6)	2.317(7)	Fe(7)-S(8)	2.298(6)
Fe(1)-Fe(5)	2.708(5)	Fe(7)-S(11)#3	2.301(6)
Fe(1)-Fe(4)	2.743(5)	Fe(7)-S(11)	2.316(6)
Fe(1)-Fe(2)	2.810(5)	Fe(7)-Fe(7)#3	2.757(6)
Fe(2)-S(9)	2.282(6)	Fe(7)-Fe(9)	2.820(5)
Fe(2)-S(2)	2.297(6)	Fe(8)-S(4)	2.266(7)
Fe(2)-S(1)	2.301(6)	Fe(8)-S(15)	2.287(7)
Fe(2)-S(3)	2.309(7)	Fe(8)-S(16)#2	2.289(6)
Fe(2)-Fe(12)	2.747(5)	Fe(8)-S(7)#2	2.331(7)
Fe(2)-Fe(3)	2.774(4)	Fe(8)-Fe(14)	2.764(4)
Fe(3)-S(13)	2.276(6)	Fe(8)-Fe(11)#2	2.806(5)
Fe(3)-S(7)	2.286(7)	Fe(9)-S(11)#3	2.230(7)
Fe(3)-S(3)	2.296(7)	Fe(9)-S(12)#4	2.261(6)
Fe(3)-S(1)	2.324(6)	Fe(9)-S(12)	2.323(7)
Fe(3)-Fe(11)	2.765(5)	Fe(9)-S(8)	2.341(6)
Fe(3)-Fe(5)#1	2.822(5)	Fe(9)-Fe(9)#4	2.718(7)
Fe(4)-S(5)	2.281(6)	Fe(9)-Fe(10)#1	2.778(4)
Fe(4)-S(6)	2.286(6)	Fe(10)-S(12)#2	2.277(6)
Fe(4)-S(14)	2.303(7)	Fe(10)-S(5)	2.282(7)
Fe(4)-S(2)	2.318(7)	Fe(10)-S(14)	2.292(6)
Fe(4)-Fe(10)	2.780(4)	Fe(10)-S(8)#2	2.325(6)
Fe(4)-Fe(12)	2.812(5)	Fe(10)-Fe(9)#2	2.778(4)
Fe(5)-S(3)#2	2.245(7)	Fe(10)-Fe(6)#2	2.843(5)
Fe(5)-S(6)	2.251(6)	Fe(11)-S(16)	2.263(7)
Fe(5)-S(4)	2.303(7)	Fe(11)-S(18)	2.275(6)
Fe(5)-S(7)#2	2.337(7)	Fe(11)-S(13)	2.279(7)
Fe(5)-Fe(8)	2.775(5)	Fe(11)-S(7)	2.324(7)
Fe(5)-Fe(3)#2	2.821(5)	Fe(11)-Fe(13)	2.721(4)
Fe(6)-S(9)	2.268(6)	Fe(11)-Fe(8)#1	2.806(5)
Fe(6)-S(5)#1	2.277(7)	Fe(12)-S(14)	2.257(7)
Fe(6)-S(10)	2.297(7)	Fe(12)-S(10)	2.263(6)
Fe(6)-S(8)	2.320(6)	Fe(12)-S(9)	2.284(7)
Fe(6)-Fe(12)	2.725(5)	Fe(12)-S(2)	2.321(7)
Fe(13)-S(13)	2.256(6)	S(7)-Fe(8)#1	2.331(7)
Fe(13)-S(15)	2.258(7)	S(7)-Fe(5)#1	2.337(7)
Fe(13)-S(18)	2.308(7)	S(8)-Fe(10)#1	2.325(6)
Fe(13)-S(17)	2.325(6)	S(11)-Fe(9)#3	2.230(7)
Fe(13)-Fe(15)	2.752(5)	S(11)-Fe(7)#3	2.301(6)

Atoms	Bond length	Atoms	Bond length
Fe(13)-Fe(14)	2.797(5)	S(12)-Fe(9)#4	2.260(6)
Fe(14)-S(15)	2.286(7)	S(12)-Fe(10)#1	2.277(6)
Fe(14)-S(19)	2.291(6)	S(16)-Fe(8)#1	2.290(6)
Fe(14)-S(16)#2	2.294(6)	S(16)-Fe(14)#1	2.294(6)
Fe(14)-S(17)	2.317(6)	S(19)-Fe(16)#6	2.239(6)
Fe(14)-Fe(16)	2.736(5)	S(20)-Fe(16)#5	2.229(7)
Fe(15)-S(18)	2.277(6)	S(20)-Fe(15)#5	2.290(6)
Fe(15)-S(20)#5	2.289(6)	Fe(17)-N(3)	2.213(13)
Fe(15)-S(20)	2.298(6)	Fe(17)-N(1)	2.229(13)
Fe(15)-S(17)	2.303(6)	Fe(17)-N(6)	2.229(13)
Fe(15)-Fe(15)#5	2.778(6)	Fe(17)-N(2)	2.248(13)
Fe(15)-Fe(16)	2.798(5)	Fe(17)-N(4)	2.250(13)
Fe(16)-S(20)#5	2.229(7)	Fe(17)-N(5)	2.254(13)
Fe(16)-S(19)#6	2.240(6)	Fe(18)-N(12)	2.181(13)
Fe(16)-S(19)	2.320(7)	Fe(18)-N(7)	2.246(13)
Fe(16)-S(17)	2.330(6)	Fe(18)-N(9)	2.245(13)
Fe(16)-Fe(16)#6	2.722(7)	Fe(18)-N(10)	2.248(13)
S(3)-Fe(5)#1	2.245(7)	Fe(18)-N(8)	2.254(13)
S(5)-Fe(6)#2	2.277(7)	Fe(18)-N(11)	2.253(13)
Atoms	Bond angle	Atoms	Bond angle
S(1)-Fe(1)-S(4)	123.4(3)	Fe(5)-Fe(1)-Fe(2)	164.74(15)
S(1)-Fe(1)-S(2)	104.9(2)	Fe(4)-Fe(1)-Fe(2)	89.46(13)
S(4)-Fe(1)-S(2)	99.8(2)	S(9)-Fe(2)-S(2)	106.8(2)
S(1)-Fe(1)-S(6)	113.2(2)	S(9)-Fe(2)-S(1)	113.8(2)
S(4)-Fe(1)-S(6)	106.9(2)	S(2)-Fe(2)-S(1)	103.7(2)
S(2)-Fe(1)-S(6)	106.6(2)	S(9)-Fe(2)-S(3)	120.6(2)
S(1)-Fe(1)-Fe(5)	142.1(2)	S(2)-Fe(2)-S(3)	104.0(2)
S(4)-Fe(1)-Fe(5)	54.41(18)	S(1)-Fe(2)-S(3)	106.2(2)
S(2)-Fe(1)-Fe(5)	112.8(2)	S(9)-Fe(2)-Fe(12)	53.04(17)
S(6)-Fe(1)-Fe(5)	52.51(17)	S(2)-Fe(2)-Fe(12)	53.91(18)
S(1)-Fe(1)-Fe(4)	125.2(2)	S(1)-Fe(2)-Fe(12)	125.5(2)
S(4)-Fe(1)-Fe(4)	110.6(2)	S(3)-Fe(2)-Fe(12)	126.2(2)
S(2)-Fe(1)-Fe(4)	53.76(17)	S(9)-Fe(2)-Fe(3)	140.8(2)
S(6)-Fe(1)-Fe(4)	52.91(17)	S(2)-Fe(2)-Fe(3)	112.2(2)
Fe(5)-Fe(1)-Fe(4)	77.40(13)	S(1)-Fe(2)-Fe(3)	53.51(17)
S(1)-Fe(1)-Fe(2)	52.72(17)	S(3)-Fe(2)-Fe(3)	52.74(17)
S(4)-Fe(1)-Fe(2)	125.7(2)	Fe(12)-Fe(2)-Fe(3)	166.09(15)
S(2)-Fe(1)-Fe(2)	52.18(17)	S(9)-Fe(2)-Fe(1)	124.7(2)
S(6)-Fe(1)-Fe(2)	124.4(2)	S(2)-Fe(2)-Fe(1)	52.74(17)
S(1)-Fe(2)-Fe(1)	50.94(17)	S(5)-Fe(4)-Fe(12)	112.68(19)

Atoms	Bond angle	Atoms	Bond angle
S(3)-Fe(2)-Fe(1)	114.5(2)	S(6)-Fe(4)-Fe(12)	126.1(2)
Fe(12)-Fe(2)-Fe(1)	90.57(13)	S(14)-Fe(4)-Fe(12)	51.19(17)
Fe(3)-Fe(2)-Fe(1)	78.95(12)	S(2)-Fe(4)-Fe(12)	52.74(17)
S(13)-Fe(3)-S(7)	106.4(2)	Fe(1)-Fe(4)-Fe(12)	90.61(14)
S(13)-Fe(3)-S(3)	112.5(2)	Fe(10)-Fe(4)-Fe(12)	77.80(12)
S(7)-Fe(3)-S(3)	103.9(3)	S(3)#2-Fe(5)-S(6)	122.4(3)
S(13)-Fe(3)-S(1)	122.3(2)	S(3)#2-Fe(5)-S(4)	112.8(2)
S(7)-Fe(3)-S(1)	104.1(2)	S(6)-Fe(5)-S(4)	107.4(3)
S(3)-Fe(3)-S(1)	105.9(2)	S(3)#2-Fe(5)-S(7)#2	103.9(3)
S(13)-Fe(3)-Fe(11)	52.67(17)	S(6)-Fe(5)-S(7)#2	103.3(2)
S(7)-Fe(3)-Fe(11)	53.76(18)	S(4)-Fe(5)-S(7)#2	105.3(2)
S(3)-Fe(3)-Fe(11)	123.4(2)	S(3)#2-Fe(5)-Fe(1)	141.2(2)
S(1)-Fe(3)-Fe(11)	128.7(2)	S(6)-Fe(5)-Fe(1)	54.78(18)
S(13)-Fe(3)-Fe(2)	138.3(2)	S(4)-Fe(5)-Fe(1)	52.62(17)
S(7)-Fe(3)-Fe(2)	115.0(2)	S(7)#2-Fe(5)-Fe(1)	114.5(2)
S(3)-Fe(3)-Fe(2)	53.16(17)	S(3)#2-Fe(5)-Fe(8)	123.8(2)
S(1)-Fe(3)-Fe(2)	52.77(17)	S(6)-Fe(5)-Fe(8)	113.3(2)
Fe(11)-Fe(3)-Fe(2)	168.42(16)	S(4)-Fe(5)-Fe(8)	51.99(17)
S(13)-Fe(3)-Fe(5)#1	124.8(2)	S(7)#2-Fe(5)-Fe(8)	53.44(18)
S(7)-Fe(3)-Fe(5)#1	53.21(18)	Fe(1)-Fe(5)-Fe(8)	78.43(13)
S(3)-Fe(3)-Fe(5)#1	50.79(17)	S(3)#2-Fe(5)-Fe(3)#2	52.39(18)
S(1)-Fe(3)-Fe(5)#1	112.77(19)	S(6)-Fe(5)-Fe(3)#2	126.2(2)
Fe(11)-Fe(3)-Fe(5)#1	90.40(13)	S(4)-Fe(5)-Fe(3)#2	124.0(2)
Fe(2)-Fe(3)-Fe(5)#1	79.35(12)	S(7)#2-Fe(5)-Fe(3)#2	51.57(17)
S(5)-Fe(4)-S(6)	121.0(2)	Fe(1)-Fe(5)-Fe(3)#2	165.80(15)
S(5)-Fe(4)-S(14)	105.1(2)	Fe(8)-Fe(5)-Fe(3)#2	89.28(13)
S(6)-Fe(4)-S(14)	114.0(2)	S(9)-Fe(6)-S(5)#1	122.7(3)
S(5)-Fe(4)-S(2)	103.5(2)	S(9)-Fe(6)-S(10)	106.2(2)
S(6)-Fe(4)-S(2)	107.5(2)	S(5)#1-Fe(6)-S(10)	113.3(2)
S(14)-Fe(4)-S(2)	103.9(2)	S(9)-Fe(6)-S(8)	104.0(2)
S(5)-Fe(4)-Fe(1)	127.1(2)	S(5)#1-Fe(6)-S(8)	103.8(2)
S(6)-Fe(4)-Fe(1)	53.96(17)	S(10)-Fe(6)-S(8)	105.0(2)
S(14)-Fe(4)-Fe(1)	125.4(2)	S(9)-Fe(6)-Fe(12)	53.49(17)
S(2)-Fe(4)-Fe(1)	53.64(18)	S(5)#1-Fe(6)-Fe(12)	140.8(2)
S(5)-Fe(4)-Fe(10)	52.50(17)	S(10)-Fe(6)-Fe(12)	52.73(17)
S(6)-Fe(4)-Fe(10)	140.4(2)	S(8)-Fe(6)-Fe(12)	115.0(2)
S(14)-Fe(4)-Fe(10)	52.59(17)	S(9)-Fe(6)-Fe(7)	112.9(2)
S(2)-Fe(4)-Fe(10)	111.9(2)	S(5)#1-Fe(6)-Fe(7)	123.8(2)
Fe(1)-Fe(4)-Fe(10)	165.52(16)	S(10)-Fe(6)-Fe(7)	52.35(17)
S(8)-Fe(6)-Fe(7)	52.69(16)	S(15)-Fe(8)-Fe(5)	129.2(2)
Fe(12)-Fe(6)-Fe(7)	79.44(13)	S(16)#2-Fe(8)-Fe(5)	123.5(2)
S(9)-Fe(6)-Fe(10)#1	127.6(2)	S(7)#2-Fe(8)-Fe(5)	53.62(18)
S(5)#1-Fe(6)-Fe(10)#1	51.51(17)	Fe(14)-Fe(8)-Fe(5)	169.05(16)

Atoms	Bond angle	Atoms	Bond angle
S(10)-Fe(6)-Fe(10)#1	124.0(2)	S(4)-Fe(8)-Fe(11)#2	125.1(2)
S(8)-Fe(6)-Fe(10)#1	52.35(16)	S(15)-Fe(8)-Fe(11)#2	113.7(2)
Fe(12)-Fe(6)-Fe(10)#1	167.12(16)	S(16)#2-Fe(8)-Fe(11)#2	51.52(17)
Fe(7)-Fe(6)-Fe(10)#1	89.29(13)	S(7)#2-Fe(8)-Fe(11)#2	52.81(18)
S(10)-Fe(7)-S(8)	106.3(2)	Fe(14)-Fe(8)-Fe(11)#2	79.61(12)
S(10)-Fe(7)-S(11)#3	112.4(2)	Fe(5)-Fe(8)-Fe(11)#2	90.53(14)
S(8)-Fe(7)-S(11)#3	103.6(2)	S(11)#3-Fe(9)-S(12)#4	120.9(2)
S(10)-Fe(7)-S(11)	120.5(2)	S(11)#3-Fe(9)-S(12)	113.5(2)
S(8)-Fe(7)-S(11)	106.0(2)	S(12)#4-Fe(9)-S(12)	107.3(2)
S(11)#3-Fe(7)-S(11)	106.7(2)	S(11)#3-Fe(9)-S(8)	104.4(2)
S(10)-Fe(7)-Fe(7)#3	138.1(2)	S(12)#4-Fe(9)-S(8)	103.9(2)
S(8)-Fe(7)-Fe(7)#3	115.3(2)	S(12)-Fe(9)-S(8)	105.3(2)
S(11)#3-Fe(7)-Fe(7)#3	53.59(17)	S(11)#3-Fe(9)-Fe(9)#4	140.2(2)
S(11)-Fe(7)-Fe(7)#3	53.09(17)	S(12)#4-Fe(9)-Fe(9)#4	54.70(18)
S(10)-Fe(7)-Fe(6)	52.94(17)	S(12)-Fe(9)-Fe(9)#4	52.58(18)
S(8)-Fe(7)-Fe(6)	53.41(16)	S(8)-Fe(9)-Fe(9)#4	115.1(2)
S(11)#3-Fe(7)-Fe(6)	123.32(19)	S(11)#3-Fe(9)-Fe(10)#1	124.0(2)
S(11)-Fe(7)-Fe(6)	128.37(19)	S(12)#4-Fe(9)-Fe(10)#1	114.65(19)
Fe(7)#3-Fe(7)-Fe(6)	168.5(2)	S(12)-Fe(9)-Fe(10)#1	52.11(16)
S(10)-Fe(7)-Fe(9)	125.1(2)	S(8)-Fe(9)-Fe(10)#1	53.20(16)
S(8)-Fe(7)-Fe(9)	53.26(16)	Fe(9)#4-Fe(9)-Fe(10)#1	79.74(16)
S(11)#3-Fe(7)-Fe(9)	50.39(17)	S(11)#3-Fe(9)-Fe(7)	52.66(17)
S(11)-Fe(7)-Fe(9)	114.32(19)	S(12)#4-Fe(9)-Fe(7)	125.1(2)
Fe(7)#3-Fe(7)-Fe(9)	79.27(15)	S(12)-Fe(9)-Fe(7)	125.47(19)
Fe(6)-Fe(7)-Fe(9)	90.75(13)	S(8)-Fe(9)-Fe(7)	51.88(16)
S(4)-Fe(8)-S(15)	121.1(3)	Fe(9)#4-Fe(9)-Fe(7)	167.0(2)
S(4)-Fe(8)-S(16)#2	111.5(2)	Fe(10)#1-Fe(9)-Fe(7)	89.73(13)
S(15)-Fe(8)-S(16)#2	105.8(2)	S(12)#2-Fe(10)-S(5)	113.9(2)
S(4)-Fe(8)-S(7)#2	106.8(2)	S(12)#2-Fe(10)-S(14)	121.1(2)
S(15)-Fe(8)-S(7)#2	106.1(2)	S(5)-Fe(10)-S(14)	105.4(2)
S(16)#2-Fe(8)-S(7)#2	104.2(2)	S(12)#2-Fe(10)-S(8)#2	107.3(2)
S(4)-Fe(8)-Fe(14)	137.0(2)	S(5)-Fe(10)-S(8)#2	103.5(2)
S(15)-Fe(8)-Fe(14)	52.79(17)	S(14)-Fe(10)-S(8)#2	103.9(2)
S(16)#2-Fe(8)-Fe(14)	52.98(17)	S(12)#2-Fe(10)-Fe(9)#2	53.60(17)
S(7)#2-Fe(8)-Fe(14)	115.8(2)	S(5)-Fe(10)-Fe(9)#2	124.2(2)
S(4)-Fe(8)-Fe(5)	53.23(18)	S(14)-Fe(10)-Fe(9)#2	128.1(2)
S(8)#2-Fe(10)-Fe(9)#2	53.72(16)	S(10)-Fe(12)-Fe(6)	53.88(17)
S(12)#2-Fe(10)-Fe(4)	138.4(2)	S(9)-Fe(12)-Fe(6)	52.96(17)
S(5)-Fe(10)-Fe(4)	52.44(17)	S(2)-Fe(12)-Fe(6)	113.5(2)
S(14)-Fe(10)-Fe(4)	52.95(17)	S(14)-Fe(12)-Fe(2)	124.9(2)
S(8)#2-Fe(10)-Fe(4)	114.07(19)	S(10)-Fe(12)-Fe(2)	111.51(19)
Fe(9)#2-Fe(10)-Fe(4)	167.58(16)	S(9)-Fe(12)-Fe(2)	53.00(17)
S(12)#2-Fe(10)-Fe(6)#2	126.4(2)	S(2)-Fe(12)-Fe(2)	53.11(17)

Atoms	Bond angle	Atoms	Bond angle
S(8)#2-Fe(10)-Fe(6)#2	52.18(16)	S(10)-Fe(12)-Fe(4)	127.4(2)
Fe(9)#2-Fe(10)-Fe(6)#2	90.22(13)	S(9)-Fe(12)-Fe(4)	123.4(2)
Fe(4)-Fe(10)-Fe(6)#2	78.92(12)	S(2)-Fe(12)-Fe(4)	52.64(17)
S(16)-Fe(11)-S(18)	122.2(2)	Fe(6)-Fe(12)-Fe(4)	165.74(15)
S(16)-Fe(11)-S(13)	112.3(2)	Fe(2)-Fe(12)-Fe(4)	89.35(13)
S(18)-Fe(11)-S(13)	106.9(2)	S(13)-Fe(13)-S(15)	122.8(2)
S(16)-Fe(11)-S(7)	105.3(2)	S(13)-Fe(13)-S(18)	106.5(3)
S(18)-Fe(11)-S(7)	103.5(2)	S(15)-Fe(13)-S(18)	112.9(2)
S(13)-Fe(11)-S(7)	105.0(2)	S(13)-Fe(13)-S(17)	102.0(2)
S(16)-Fe(11)-Fe(13)	140.4(2)	S(15)-Fe(13)-S(17)	105.2(2)
S(18)-Fe(11)-Fe(13)	54.15(17)	S(18)-Fe(13)-S(17)	105.7(2)
S(13)-Fe(11)-Fe(13)	52.74(17)	S(13)-Fe(13)-Fe(11)	53.52(18)
S(7)-Fe(11)-Fe(13)	113.9(2)	S(15)-Fe(13)-Fe(11)	140.4(2)
S(16)-Fe(11)-Fe(3)	123.8(2)	S(18)-Fe(13)-Fe(11)	53.01(17)
S(18)-Fe(11)-Fe(3)	113.54(19)	S(17)-Fe(13)-Fe(11)	114.11(19)
S(13)-Fe(11)-Fe(3)	52.57(17)	S(13)-Fe(13)-Fe(15)	112.7(2)
S(7)-Fe(11)-Fe(3)	52.51(18)	S(15)-Fe(13)-Fe(15)	124.1(2)
Fe(13)-Fe(11)-Fe(3)	79.07(13)	S(18)-Fe(13)-Fe(15)	52.61(17)
S(16)-Fe(11)-Fe(8)#1	52.37(17)	S(17)-Fe(13)-Fe(15)	53.14(16)
S(18)-Fe(11)-Fe(8)#1	126.4(2)	Fe(11)-Fe(13)-Fe(15)	79.54(13)
S(13)-Fe(11)-Fe(8)#1	124.7(2)	S(13)-Fe(13)-Fe(14)	126.6(2)
S(7)-Fe(11)-Fe(8)#1	53.04(18)	S(15)-Fe(13)-Fe(14)	52.45(18)
Fe(13)-Fe(11)-Fe(8)#1	166.83(15)	S(18)-Fe(13)-Fe(14)	124.5(2)
Fe(3)-Fe(11)-Fe(8)#1	89.78(13)	S(17)-Fe(13)-Fe(14)	52.81(16)
S(14)-Fe(12)-S(10)	123.1(2)	Fe(11)-Fe(13)-Fe(14)	166.76(15)
S(14)-Fe(12)-S(9)	112.0(2)	Fe(15)-Fe(13)-Fe(14)	89.33(13)
S(10)-Fe(12)-S(9)	106.8(2)	S(15)-Fe(14)-S(19)	111.9(2)
S(14)-Fe(12)-S(2)	105.3(2)	S(15)-Fe(14)-S(16)#2	105.7(2)
S(10)-Fe(12)-S(2)	101.9(2)	S(19)-Fe(14)-S(16)#2	120.2(2)
S(9)-Fe(12)-S(2)	106.0(2)	S(15)-Fe(14)-S(17)	104.6(2)
S(14)-Fe(12)-Fe(6)	140.9(2)	S(19)-Fe(14)-S(17)	108.2(2)
S(16)#2-Fe(14)-S(17)	105.0(2)	S(20)#5-Fe(16)-S(17)	105.1(2)
S(15)-Fe(14)-Fe(16)	124.4(2)	S(19)#6-Fe(16)-S(17)	105.0(2)
S(19)-Fe(14)-Fe(16)	54.10(17)	S(19)-Fe(16)-S(17)	106.7(2)
S(16)#2-Fe(14)-Fe(16)	128.3(2)	S(20)#5-Fe(16)-Fe(16)#6	137.3(2)
S(17)-Fe(14)-Fe(16)	54.16(16)	S(19)#6-Fe(16)-Fe(16)#6	54.72(18)
S(15)-Fe(14)-Fe(8)	52.84(17)	S(19)-Fe(16)-Fe(16)#6	52.00(17)
S(19)-Fe(14)-Fe(8)	136.6(2)	S(17)-Fe(16)-Fe(16)#6	117.3(2)
S(16)#2-Fe(14)-Fe(8)	52.83(17)	S(20)#5-Fe(16)-Fe(14)	124.4(2)
S(17)-Fe(14)-Fe(8)	114.89(19)	S(19)#6-Fe(16)-Fe(14)	115.1(2)
Fe(16)-Fe(14)-Fe(8)	168.87(16)	S(19)-Fe(16)-Fe(14)	53.10(17)
S(15)-Fe(14)-Fe(13)	51.56(17)	S(17)-Fe(16)-Fe(14)	53.70(17)
S(19)-Fe(14)-Fe(13)	125.7(2)	Fe(16)#6-Fe(16)-Fe(14)	80.64(16)

Atoms	Bond angle	Atoms	Bond angle
Fe(16)-Fe(14)-Fe(13)	90.69(13)	S(19)-Fe(16)-Fe(15)	124.58(19)
Fe(8)-Fe(14)-Fe(13)	79.71(12)	S(17)-Fe(16)-Fe(15)	52.39(16)
S(18)-Fe(15)-S(20)#5	112.9(2)	Fe(16)#6-Fe(16)-Fe(15)	169.3(2)
S(18)-Fe(15)-S(20)	119.8(2)	Fe(14)-Fe(16)-Fe(15)	89.64(13)
S(20)#5-Fe(15)-S(20)	105.4(2)	Fe(1)-S(1)-Fe(2)	76.3(2)
S(18)-Fe(15)-S(17)	107.5(2)	Fe(1)-S(1)-Fe(3)	102.0(2)
S(20)#5-Fe(15)-S(17)	104.0(2)	Fe(2)-S(1)-Fe(3)	73.72(19)
S(20)-Fe(15)-S(17)	105.9(2)	Fe(2)-S(2)-Fe(1)	75.1(2)
S(18)-Fe(15)-Fe(13)	53.64(17)	Fe(2)-S(2)-Fe(4)	115.7(2)
S(20)#5-Fe(15)-Fe(13)	123.7(2)	Fe(1)-S(2)-Fe(4)	72.60(19)
S(20)-Fe(15)-Fe(13)	129.2(2)	Fe(2)-S(2)-Fe(12)	73.0(2)
S(17)-Fe(15)-Fe(13)	53.88(16)	Fe(1)-S(2)-Fe(12)	116.8(2)
S(18)-Fe(15)-Fe(15)#5	137.0(2)	Fe(4)-S(2)-Fe(12)	74.6(2)
S(20)#5-Fe(15)-Fe(15)#5	52.86(17)	Fe(5)#1-S(3)-Fe(3)	76.8(2)
S(20)-Fe(15)-Fe(15)#5	52.59(17)	Fe(5)#1-S(3)-Fe(2)	103.3(2)
S(17)-Fe(15)-Fe(15)#5	115.2(2)	Fe(3)-S(3)-Fe(2)	74.1(2)
Fe(13)-Fe(15)-Fe(15)#5	168.8(2)	Fe(1)-S(4)-Fe(8)	100.3(2)
S(18)-Fe(15)-Fe(16)	125.6(2)	Fe(1)-S(4)-Fe(5)	73.0(2)
S(20)#5-Fe(15)-Fe(16)	50.77(17)	Fe(8)-S(4)-Fe(5)	74.8(2)
S(20)-Fe(15)-Fe(16)	114.54(19)	Fe(6)#2-S(5)-Fe(4)	103.3(2)
S(17)-Fe(15)-Fe(16)	53.29(16)	Fe(6)#2-S(5)-Fe(10)	77.1(2)
Fe(13)-Fe(15)-Fe(16)	90.34(14)	Fe(4)-S(5)-Fe(10)	75.1(2)
Fe(15)#5-Fe(15)-Fe(16)	79.77(15)	Fe(5)-S(6)-Fe(4)	97.4(2)
S(20)#5-Fe(16)-S(19)#6	120.2(2)	Fe(5)-S(6)-Fe(1)	72.71(19)
S(20)#5-Fe(16)-S(19)	112.1(2)	Fe(4)-S(6)-Fe(1)	73.1(2)
S(19)#6-Fe(16)-S(19)	106.7(2)	Fe(3)-S(7)-Fe(11)	73.7(2)
Fe(3)-S(7)-Fe(8)#1	116.8(2)	Fe(3)-S(13)-Fe(11)	74.8(2)
Fe(11)-S(7)-Fe(8)#1	74.2(2)	Fe(12)-S(14)-Fe(10)	101.1(2)
Fe(3)-S(7)-Fe(5)#1	75.2(2)	Fe(12)-S(14)-Fe(4)	76.1(2)
Fe(11)-S(7)-Fe(5)#1	116.6(2)	Fe(10)-S(14)-Fe(4)	74.5(2)
Fe(8)#1-S(7)-Fe(5)#1	72.9(2)	Fe(13)-S(15)-Fe(14)	76.0(2)
Fe(7)-S(8)-Fe(6)	73.9(2)	Fe(13)-S(15)-Fe(8)	103.3(2)
Fe(7)-S(8)-Fe(10)#1	117.3(2)	Fe(14)-S(15)-Fe(8)	74.4(2)
Fe(6)-S(8)-Fe(10)#1	75.5(2)	Fe(11)-S(16)-Fe(8)#1	76.1(2)
Fe(7)-S(8)-Fe(9)	74.85(19)	Fe(11)-S(16)-Fe(14)#1	103.0(2)
Fe(6)-S(8)-Fe(9)	117.4(2)	Fe(8)#1-S(16)-Fe(14)#1	74.2(2)
Fe(10)#1-S(8)-Fe(9)	73.08(19)	Fe(15)-S(17)-Fe(14)	115.2(2)
Fe(6)-S(9)-Fe(2)	98.4(2)	Fe(15)-S(17)-Fe(13)	72.99(19)
Fe(6)-S(9)-Fe(12)	73.54(19)	Fe(14)-S(17)-Fe(13)	74.13(19)
Fe(2)-S(9)-Fe(12)	74.0(2)	Fe(15)-S(17)-Fe(16)	74.31(19)
Fe(12)-S(10)-Fe(7)	101.5(2)	Fe(14)-S(17)-Fe(16)	72.14(19)
Fe(12)-S(10)-Fe(6)	73.4(2)	Fe(13)-S(17)-Fe(16)	115.5(2)
Fe(7)-S(10)-Fe(6)	74.7(2)	Fe(11)-S(18)-Fe(15)	100.6(2)

Atoms	Bond angle	Atoms	Bond angle
Fe(7)#3-S(11)-Fe(7)	73.3(2)	Fe(16)#6-S(19)-Fe(14)	102.4(2)
Fe(9)#4-S(12)-Fe(10)#1	101.9(2)	Fe(16)#6-S(19)-Fe(16)	73.3(2)
Fe(9)#4-S(12)-Fe(9)	72.7(2)	Fe(14)-S(19)-Fe(16)	72.79(19)
Fe(10)#1-S(12)-Fe(9)	74.3(2)	Fe(16)#5-S(20)-Fe(15)#5	76.5(2)
Fe(13)-S(13)-Fe(3)	100.8(2)	Fe(16)#5-S(20)-Fe(15)	104.3(2)
Fe(13)-S(13)-Fe(11)	73.7(2)	Fe(15)#5-S(20)-Fe(15)	74.6(2)

Symmetry transformations used to generate equivalent atoms:

#1 $x-1, y, z$ #2 $x+1, y, z$ #3 $-x-1, -y, -z$ #4 $-x-2, -y, -z$ #5 $-x-1, -y+1, -z$ #6 $-x, -y+1, -z$

The phase purity of each sample was analyzed by powder X-ray diffraction using a Rigaku D/M-2200T automated diffraction system (Ultima+). The measurements were made with a 2θ range between 3 and 70° at the operation power of 40 KV/40 mA. Figure 23 gave the PXRD pattern of pure compound **3**. The band gap of **3** and all substituted samples were assessed by optical diffuse reflectance experiments at room temperature. All measurements were made on a Shimadzu UV-3101PC double beam, double monochromated spectrophotometer in the range of 200-2000 nm. Thermogravimetric analysis (TGA) was carried out on a TA Instrument Q50 Thermogravimetric analyzer under nitrogen.

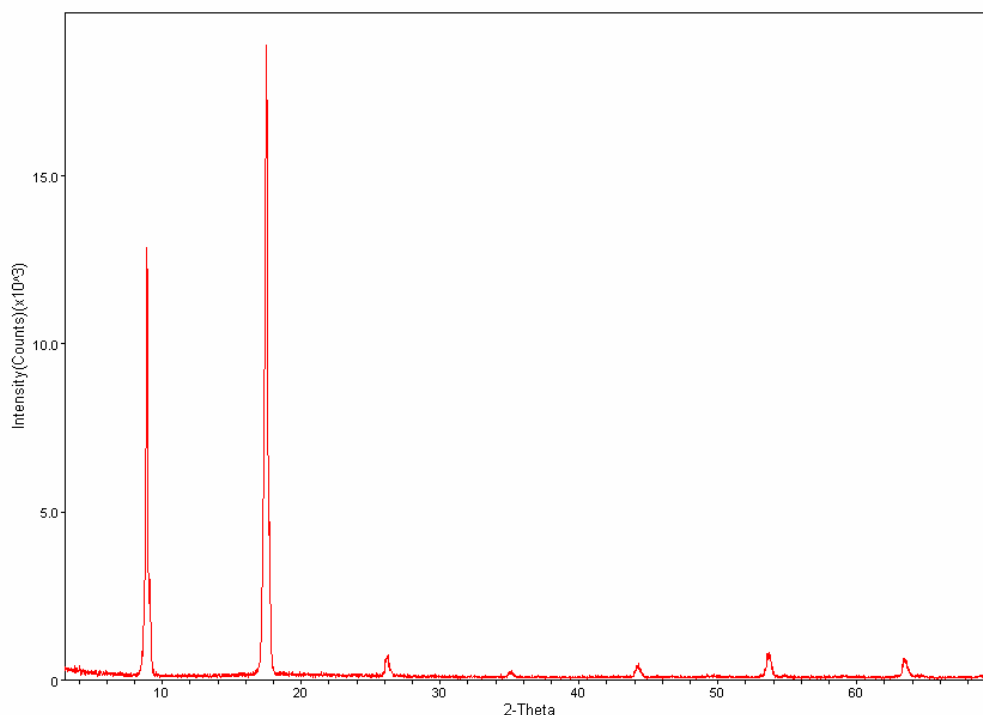


Figure 23. Powder X-ray diffraction pattern of **3**

5.1.3. X-ray Absorption Analysis (XAS)

The Fe-*K* X-ray absorption analysis (XAS) measurements were performed in the fluorescence mode on crystal samples on beamline X19A (Upton, New York USA) at the Brookhaven National Synchrotron Light Source. A double crystal Si (111) monochromator was used. The incident and transmitted beam intensities were measured with ionization chambers and the fluorescence intensities with Canberra PIPS detectors. The absolute energy calibration was set to the elemental Fe-*K* edge (first inflection point) 7.112 KeV. The simultaneous standard technique was used in which a standard sample

(FeO in this case) is placed after the second ionization chamber and a simultaneous fluorescence spectrum is collected for the standard. This allows a relative energy calibration between spectra of better than 0.05 eV.

5.2. Results and Discussion

The compound **3** exhibits unique two-dimensional Fe-S layers, shown in Figure 24(a). Interestingly, Fe in the $[\text{Fe}_{16}\text{S}_{20}]$ layers has 7-coordination where 4-coordination to adjacent S atoms and 3-coordination to adjacent Fe atoms, which is not quite common coordination geometry. There are sixteen crystallographically independent Fe atoms on this non-symmetric plane. And the bond lengths between Fe to Fe atoms vary from 2.708 to 2.843 Å which is a little longer comparing with metal-metal bonds in other iron complexes, such as $\text{Fe}_3(\text{CO})_9$ (2.46 Å).⁷¹ S^{2-} on the 2D layers has two different coordination sites (3 and 4-coordination). From the side view of this structure as shown in Figure 24(b), the iron layer is flanked by two sulfur layers, forming a sandwich like structure. The Fe-S layer possesses a negative charge, which is balanced by the cations between the sandwich layers. The cation is a $[\text{Fe}(\text{en})_3]^{2+}$ chelating complex with most likely iron 2+ valence charge which is observed in most chalcogenide compounds²¹, where Fe coordinates to 3 ethylenediamine molecules. Thus, the layer is most likely $[\text{Fe}_{16}\text{S}_{20}]^{4-}$ with mixed valency of Fe(II) and Fe(III).

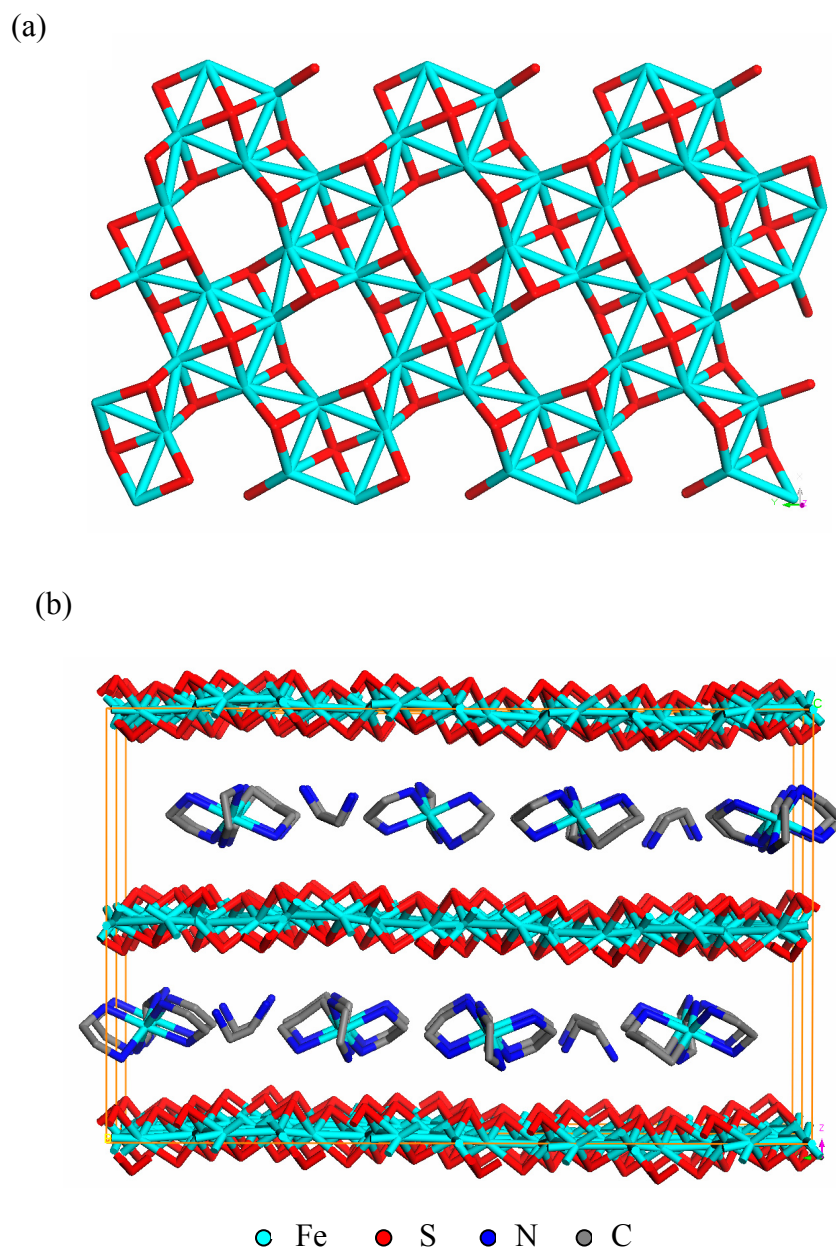


Figure 24. (a) Anionic $[\text{Fe}_{16}\text{S}_{20}]^{4-}$ layers (b) Side view of the layered structure showing $[\text{Fe}(\text{en})_3]^{2+}$ and ethylenediamine molecules residing between the $[\text{Fe}_{16}\text{S}_{20}]^{4-}$ layers.

In order to understand more about the structure and valence state of Fe, X-ray absorption analysis was performed to study the Fe valence charge. Figure 25(a) showed the transition metal Fe *K*-edges. In general one expects a chemical shift to higher energy of an x-ray absorption edge with increasing formal chemical valence due to the loss of electronic screening with increasing valence. A number of factors however complicate this picture. The Fe *K* edge (see figure) marks the onset of dipole allowed transitions from the core-level *1s* level to empty *p*-states. Both transitions to continuum states and atomic-like Fe-4*p* states dominate the Fe-*K* near edge structure. In general there will be multiplicity of 4*p* states due to solid-state splittings of the 4*p* levels and by replication of 4*p* features associated with different 3*d* configurations which are covalently band mixed into the solid-state electronic structure. Thus the onset of the steeply rising portion of the edge will be influenced by 4*p* state splittings.

A good example of such splittings is provided by comparing the formally trivalent Fe₂O₃ and Fe(en)₃Cl₃. The Fe(en)₃Cl₃ has a smoothly rising edge whereas the Fe₂O₃ has a feature split down to lower energy and the peak features split to higher energy. The two spectra cross at absorption coefficient of about 0.75 indicating their comparable chemical shift. The +4 compound SrFeO_{3- δ} can be seen to have a clearly higher chemical shift.

The situation for the divalent compounds is somewhat more complicated. The divalent compounds FeO, and FeS compounds edges are clearly shifted to lower energy relative to the trivalent compounds however the difference in the near edge features of the two gives a rather widespread for the chemical shift in the divalent state. Moreover, the compound of interest here has a much lower symmetry than these standards precluding a direct simple comparison of their chemical shifts. Comparison of the inflection point of

the initial rise in the compound **3** (Fe-S-en) spectrum to the divalent standards can be said to support a “close to” divalent state for this compound.

In Figure 25(b) the Fe-K pre-edge region is shown. Here the term pre-edge is used because these small features are shifted down in energy below the main edge. The features in this pre-edge region are due to quadrupole $1s$ to $3d$ transitions or dipole $1s$ to hybrid d/p states. The pre-edge features typically have semi-localized $3d$ final states which have an attractive Coulomb interaction with the $1s$ core hole created in the ionization process. This Coulomb energy accounts for the shifting of these features below the main edge. In general the Fe^{2+} spectra show pre-edge features in a lower energy range, labeled “a” in the inset, and the Fe^{3+} , Fe^{4+} pre-edge features occur in a somewhat higher “b” energy range. The Fe^{2+} pre-edge features are typically broader and unresolved. In contrast the Fe^{3+} and Fe^{4+} pre-edge features typically show distinct b1-b2 sub features. The pre-edge feature of the compound **3**(Fe-S-en) appears in structure and in energy consistent with a basically Fe^{2+} state. The quite high relative intensity of the compound **3**(Fe-S-en) pre-edge feature should be noted. The Fe in Fe-S-en sits in a non-centro-symmetric environment. This allows for d - p hybridization and the admixture of the stronger dipole $1s$ to p transitions into the pre-edge feature. Thus the high relative intensity of the Fe-S-en pre-edge feature is consistent with the low symmetry site.

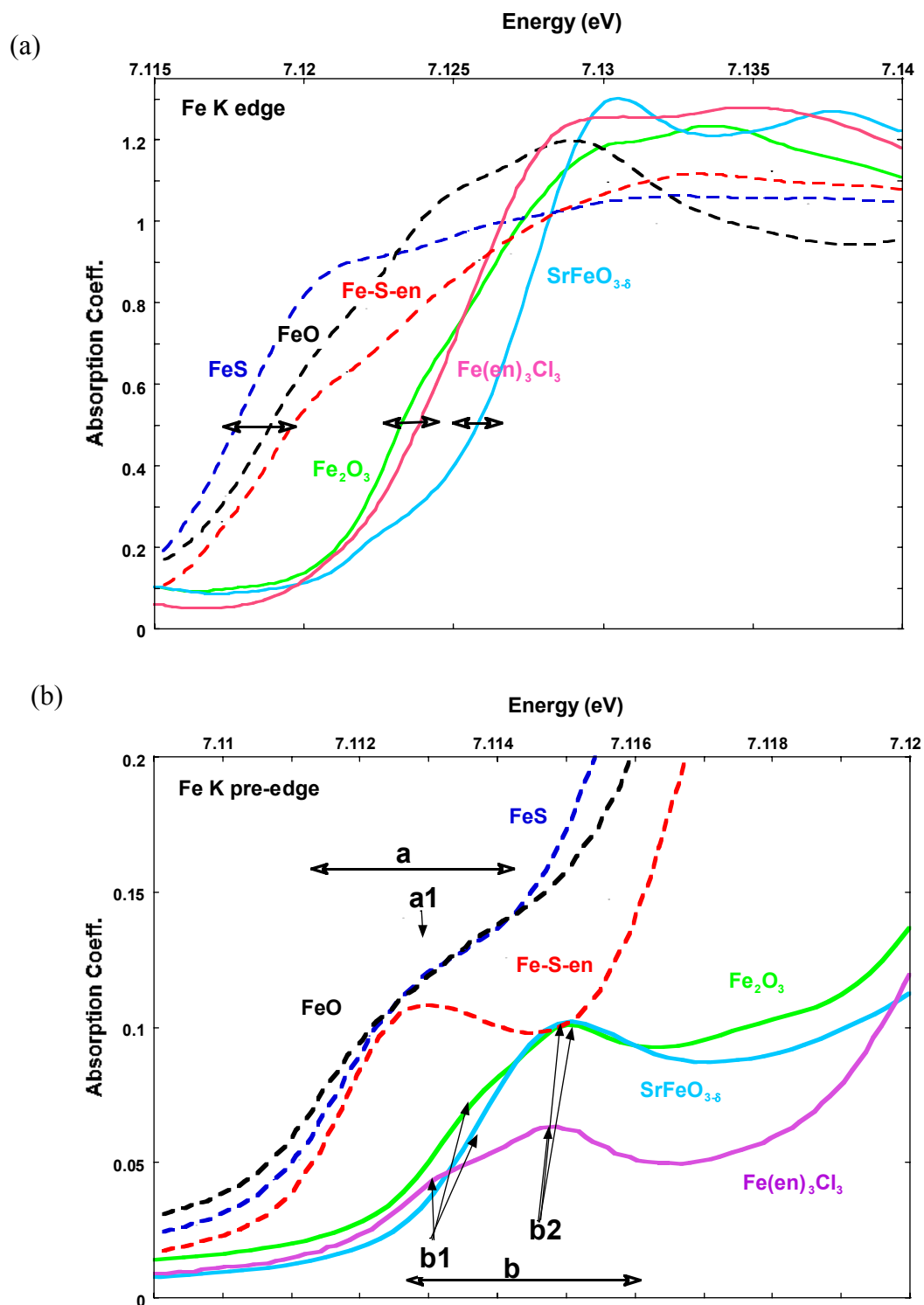


Figure 25. (a) XAS spectra of Fe K edge for a series of Fe compounds with different valence charge. (b). XAS spectra of Fe K Pre-edge. (Fe(II)S: dash blue, Fe(II)O: dash black, Fe-S-en (compound **3**): dash red, Fe(III) $_2$ O $_3$: solid green, Fe(III)(en) $_3$ Cl $_3$: solid purple, SrFe(IV)O $_{3.8}$: solid blue)

TGA has been carried out and gave a weight loss of $\sim 19.9\%$ at about 350°C (Figure 26), which matched well with calculated amount of all ethylenediamine molecules (20.3%). And the sample was characterized by Powder X-ray diffraction after TGA. It indicated Fe_9S_{10} as major phase after 500°C (Figure 27) which is consistent with the composition of Fe and S in the original **3**. The continuous weight loss after 350°C is due to the decomposition of iron sulfide (Fe_9S_{10}). All the sulfur might be oxidized or sublimed and the final residues after TGA 700°C were iron oxide. Another TGA was carried out again from room temperature to 160°C with $5^\circ\text{C}/\text{min}$ and kept for 40 minutes. It showed around 3% weight loss which probably came from the free ethylenediamine molecules (Figure 28). Powder X-ray diffraction showed the compound was still intact after TGA which is shown in Figure 29. Optical diffuse reflectance experiment (UV-Vis) indicated a low band gap of $\sim 0.5\text{ eV}$ (Figure 30).

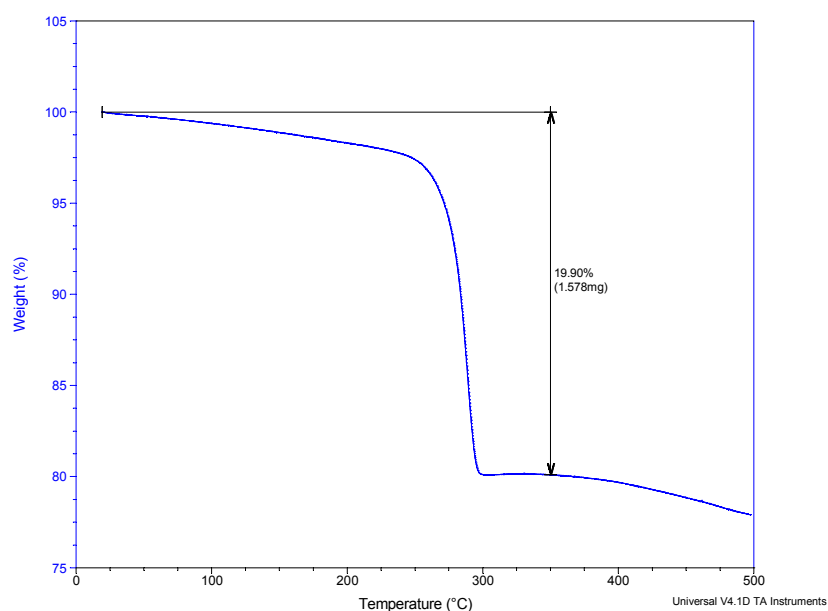


Figure 26. TGA pattern of compound **3** gave 19.9% weight loss at around 350°C .

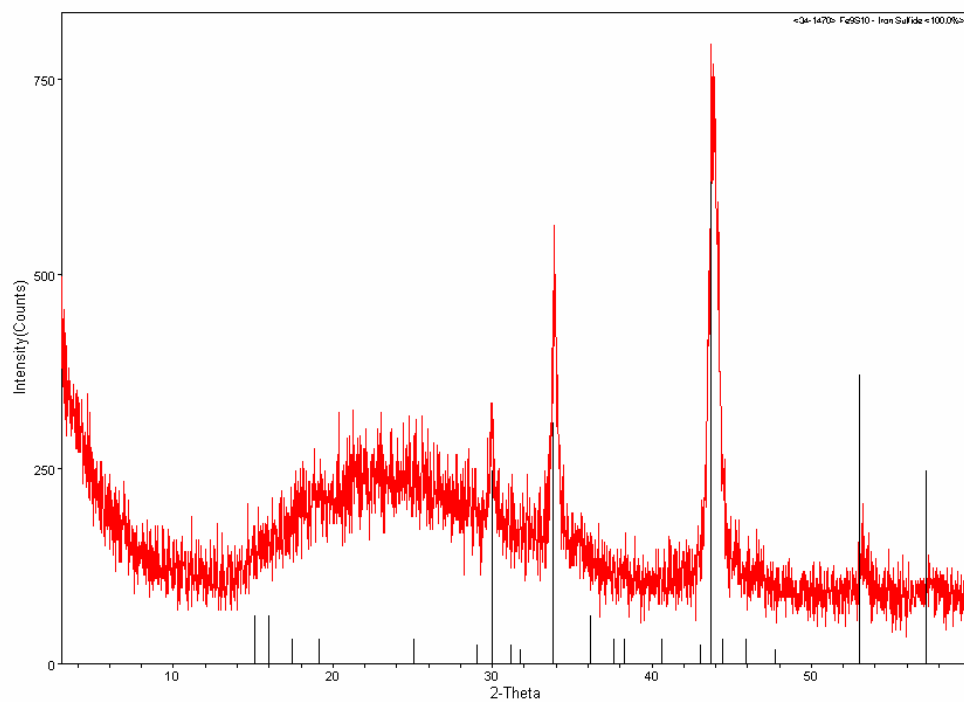


Figure 27. Powder X-ray pattern of **3** after TGA 500° C (black line: Fe_9S_{10}).

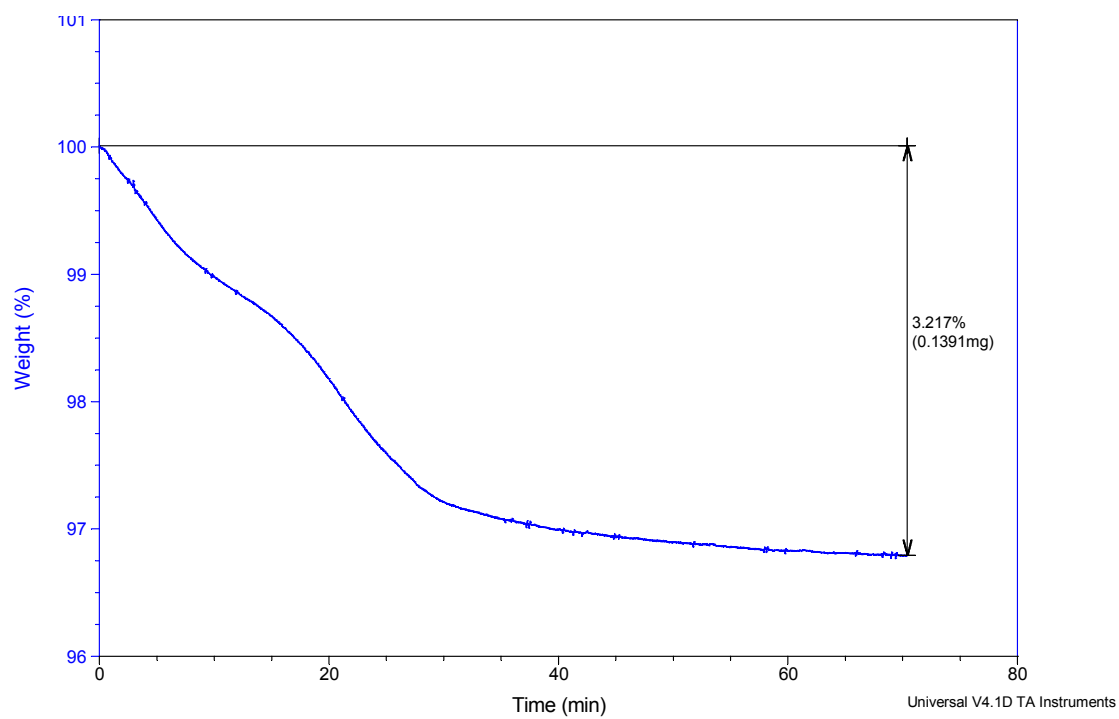


Figure 28. TGA pattern run until 160° C and kept for 40 minutes.

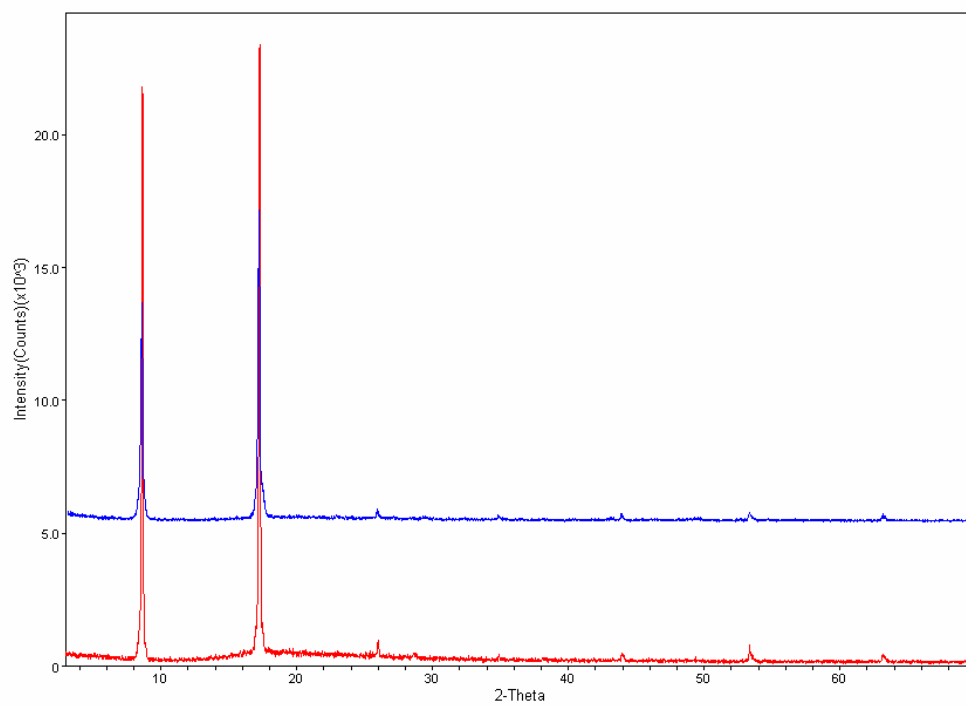


Figure 29. Powder X-ray pattern of before (red) and after (blue) TGA 160° C.

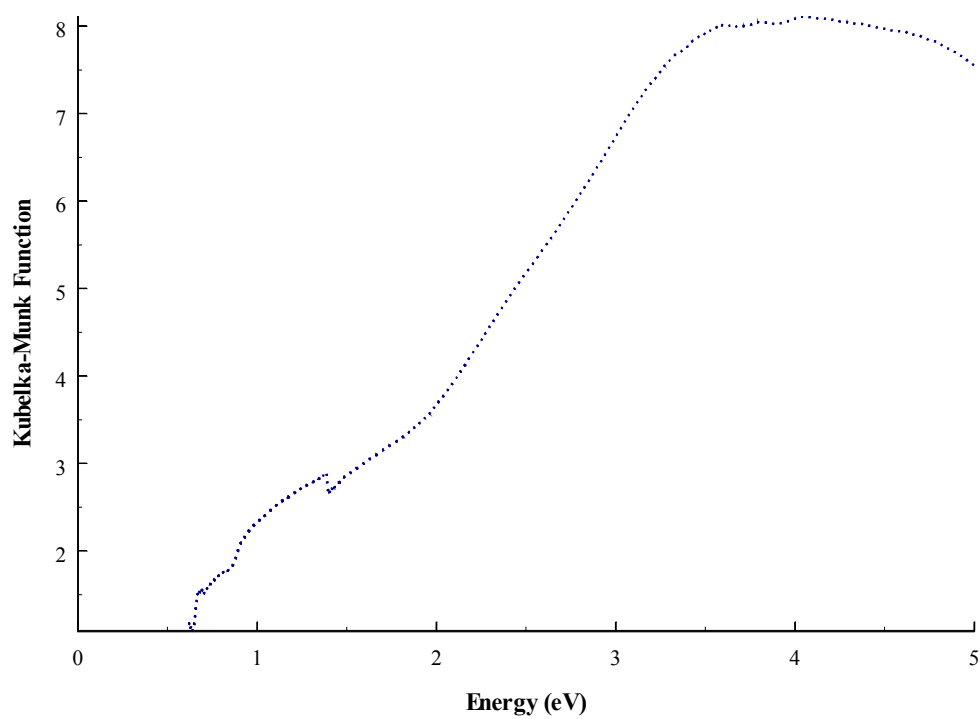
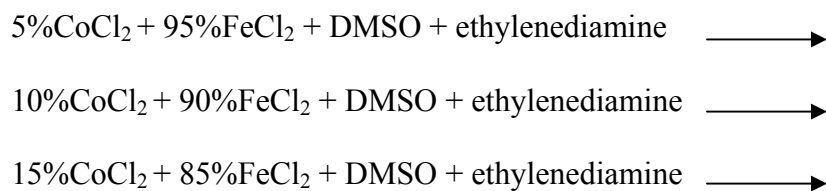


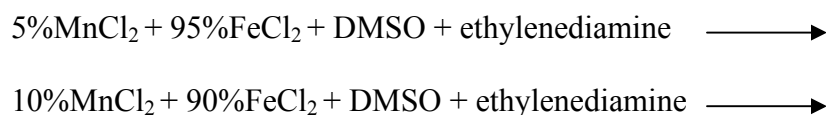
Figure 30. UV-Vis diffuse reflectance spectrum of compound **3**.

In order to tune the semiconductivity and magnetic properties, substitution of Fe on the layers with Co and Mn in different concentration under the same synthesis strategy were performed (scheme 1, 2). PXRD patterns showed all final products have the same structure as the pure Fe compound (Figure 31). While the intensity of peaks decreased as the Co concentration increased. The UV-Vis diffuse spectroscopy showed band gap of the final products with Mn and Co doping/substitution (Figure 32). The band gaps of 5% and 10% Mn/Co doping compounds have no significant change comparing the original compound **3**. The band gap of the higher Co concentration 15% was shifted to ~2 eV. It gave clear evidence that there is another major phase instead of the original one.

Scheme 1



Scheme 2



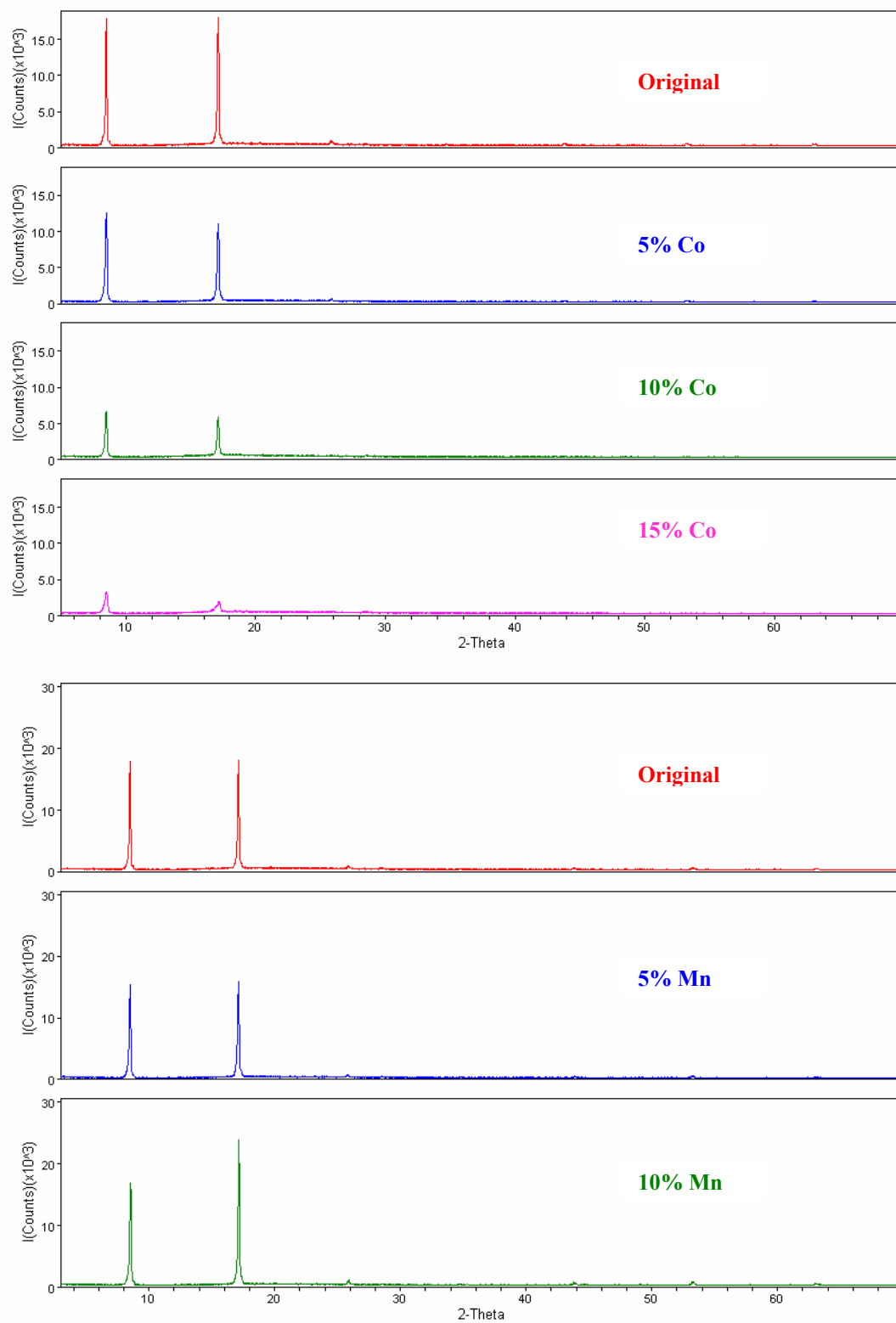


Figure 31. Powder X-ray patterns of the original and doped/substituted compounds.

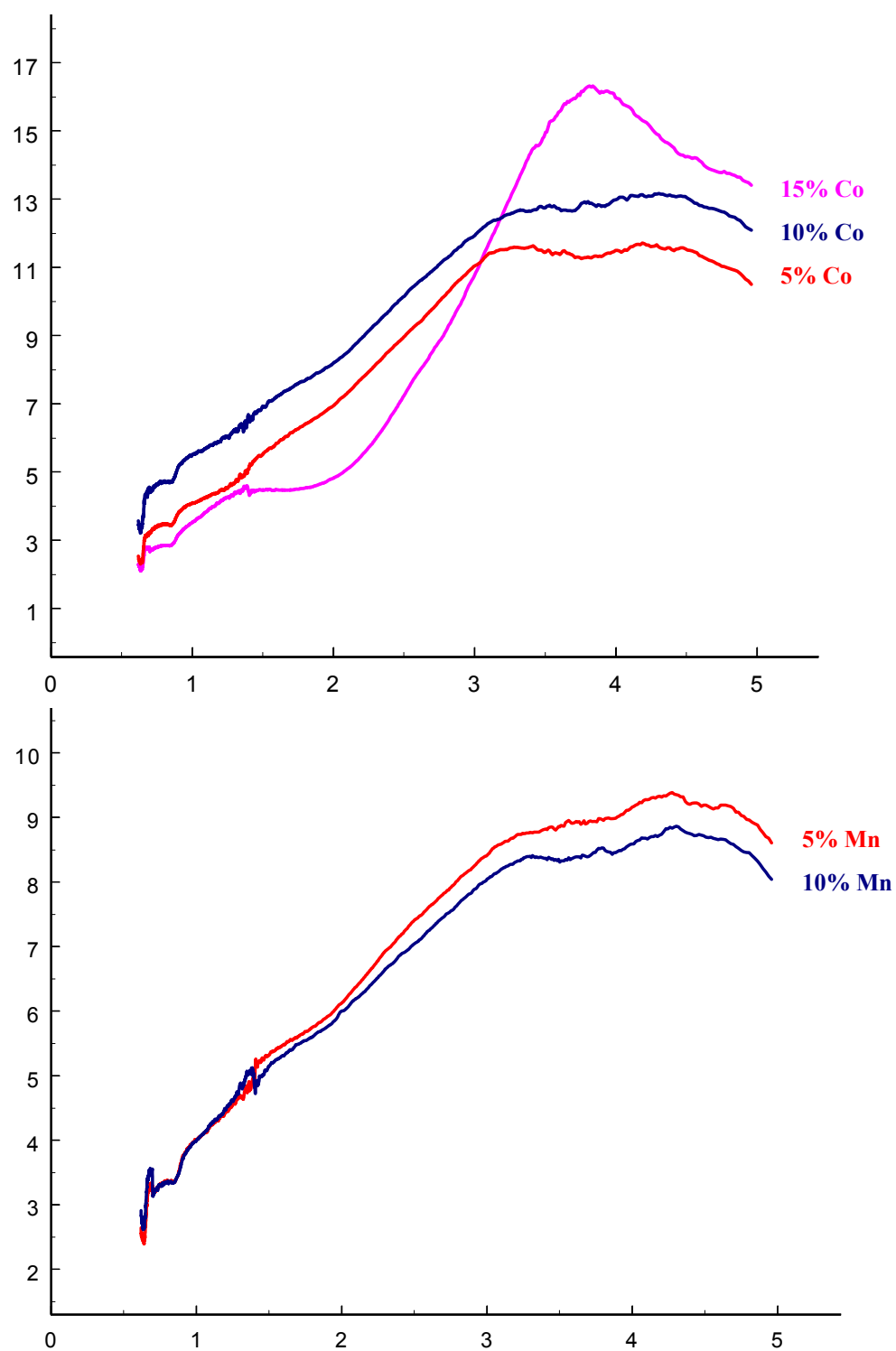


Figure 32. UV-Vis diffuse reflectance spectrum of Co/Mn doped compounds.

5.3. Conclusion and Summary

The novel iron-sulfur compound with unique anionic $[\text{Fe}_{16}\text{S}_{20}]^{4-}$ 2D layers has been successfully synthesized. Like other known iron sulfide materials, this new compound demonstrates low band gap characteristic as well. The unique Fe-S, Fe-Fe coordination, and two dimensional layers may exhibit interesting optical and electrical properties. X-ray absorption analysis provided the evidence for the +2 valence description of Fe. The magnetic measurements based on Co and Mn doped materials will be studied in the near future.

Reference

1. N. F. Zheng, X. H. Bu and P. Y. Feng, *Angewandte Chemie-International Edition*, 2004, **43**, 4753-4755.
2. H. Ahari, A. Garcia, S. Kirkby, G. A. Ozin, D. Young and A. J. Lough, *Journal of the Chemical Society-Dalton Transactions*, 1998, 2023-2027.
3. S. Dhingra and M. G. Kanatzidis, *Science*, 1992, **258**, 1769-1772.
4. K. W. Kim and M. G. Kanatzidis, *Journal of the American Chemical Society*, 1992, **114**, 4878-4883.
5. J. B. Parise, *Science*, 1991, **251**, 293-294.
6. W. S. Sheldrick and M. Wachhold, *Angewandte Chemie-International Edition*, 1997, **36**, 207-224.
7. W. S. Sheldrick, *Journal of the Chemical Society-Dalton Transactions*, 2000, 3041-3052.
8. S. Yang, X. Chen and S. Motojima, *Journal of Materials Science*, 2004, **39**, 2727-2736.
9. R. Hilton and P. D. Fleischauer, *Surface and Coatings Technology*, 1992, **54-55**, 435.
10. L. Wang, J. Schindler, J. A. Thomas, C. R. Kannewurf and M. G. Kanatzidis, *Chemistry of Materials*, 1995, **7**, 1753.
11. G. Prasad and O. N. Srivasta, *Journal of Physics D*, 1988, **21**, 1028-1030.
12. X. H. Bu, N. F. Zheng and P. Y. Feng, *Chemistry-a European Journal*, 2004, **10**, 3356-3362.
13. G. S. H. Lee, D. C. Craig and I. Ma, *Journal of the American Chemical Society*, 1988, **110**, 4863-4864.
14. H. Li, A. Laine and O. M. Yaghi, *Science*, 1999, **283**, 1145-1147.
15. P. Y. Feng, X. H. Bu and N. F. Zheng, *Accounts of Chemical Research*, 2005, **38**, 293-303.
16. A. M. Pirani, H. P. A. Mercier, D. A. Dixon, H. Borrmann and G. J. Schrobilgen, *Inorganic Chemistry*, 2001, **40**, 4823-4829.
17. H. L. Li, A. Laine, M. O'Keeffe and O. M. Yaghi, *Science*, 1999, **283**, 1145-1147.
18. H. L. Li, J. Kim, T. L. Groy, M. O'Keeffe and O. M. Yaghi, *Journal of the American Chemical Society*, 2001, **123**, 4867-4868.
19. O. Palchik, R. G. Iyer, J. H. Liao and M. G. Kanatzidis, *Inorganic Chemistry*, 2003, **42**, 5052-5054.
20. P. N. Trikalitis, K. K. Rangan and M. G. Kanatzidis, *Journal of the American Chemical Society*, 2002, **124**, 2604-2613.
21. J. Li, Z. Chen, R. J. Wang and D. M. Proserpio, *Coordination Chemistry Reviews*, 1999, **192**, 707-735.
22. Z. Chen, J. Li, unpublished results.
23. M. Wu, W. P. Sul, N. Jasutkar, X. Y. Huang and J. Li, *Materials Research Bulletin*, 2005, **40**, 21-27.
24. X. H. Bu, N. F. Zheng, Y. Q. Li and P. Y. Feng, *Journal of the American Chemical Society*, 2003, **125**, 6024-6025.

25. The formula of an isolated Tn unit is where $tn = n(n + 1)(n + 2)/6$ is the nth tetrahedral number. The corresponding formula for a corner-connected supertetrahedral framework is $Mtn Qtn + 1$.
26. R. L. Whetten, J. T. Khoury and M. M. Alvarez, *Advanced materials*, 1996, **8**, 428.
27. S. A. Harfenist, Z. L. Wang, R. L. Whetten, I. Vezmar and M. M. Alvarez, *Advanced Materials*, 1997, **9**, 817.
28. S. A. Harfenist, Z. L. Wang, M. M. Alvarez, I. Vezmar and R. L. Whetten, *Journal of Physical Chemistry*, 1996, **100**, 13904-13910.
29. N. F. Zheng, X. H. Bu and P. Y. Feng, *Journal of the American Chemical Society*, 2003, **125**, 1138-1139.
30. N. F. Zheng, X. G. Bu, B. Wang and P. Y. Feng, *Science*, 2002, **298**, 2366-2369.
31. H. L. Li, M. Eddaoudi, A. Laine, M. O'Keeffe and O. M. Yaghi, *Journal of the American Chemical Society*, 1999, **121**, 6096-6097.
32. C. L. Cahill, Y. Ko and J. B. Parise, *Chemistry of Materials*, 1998, **10**, 19.
33. M. J. MacLachlan, S. Petrov, R. L. Bedard, I. Manners and G. A. Ozin, *Angewandte Chemie-International Edition*, 1998, **37**, 2076-2079.
34. H. Li, A. Laine, M. O'Keeffe and O. M. Yaghi, *Science*, 1999, **283**, 1145.
35. Y. Zheng, J. R. Li, Y. B. Xie and X. H. Bu, *Acta Crystallographica Section E-Structure Reports Online*, 2002, **58**, o923-o924.
36. R. J. Coustal, *Chemical Physics*, 1958, **38**, 277.
37. D. M. P. Mingos and D. R. Baghurst, *Chemical Society Reviews*, 1991, **20**, 1-47.
38. H. C. Metcalf, J. E. Williams and J. F. Caska, *Modern Chemistry*, Holt, Reinhart, Winston, New York, 1982.
39. R. A. Laudise, *C&EN News*, 1987, **30**.
40. Y. Park and M. G. Kanatzidis, *Inorganic Chemistry*, 2001, **40**, 5913-5916.
41. H. Schafer, K. Volk, B. Eisenmann, *Fifth European Crystallographic Meeting*, Copenhagen, 1979, pp. 0-52.
42. W. S. Sheldrick, *Z. Anorg. Allg. Chem.*, 1988, **562**, 23.
43. A. Stein, S. W. Keller and T. E. Mallouk, *Science*, 1993, **259**, 1558.
44. M. E. Davis, *Nature*, 2002, **417**, 813.
45. N. F. Zheng, X. H. Bu and P. Y. Feng, *Journal of the American Chemical Society*, 2002, **124**, 9688-9689.
46. S. D. Brunauer, L. S.; Deming, D. W.; Teller, E., *Journal of the American Chemical Society*, 1940, **62**, 1723-1732.
47. N. F. Zheng, X. H. Bu and P. Y. Feng, *Nature*, 2003, **426**, 428-432.
48. N. Zheng, X. H. Bu, H. Vu and P. Y. Feng, *Angewandte Chemie-International Edition*, 2005, **44**, 5299-5303.
49. J. Li, Z. Chen, X. X. Wang and D. M. Proserpio, *Journal of Alloys and Compounds*, 1997, **262**, 28-33.
50. H. G. Wendlandt, *Reflectance Spectroscopy*, Interscience, A Division of John Wiley & Sons, New York, 1966.
51. A. Bianconi, *X-ray Absorption: Principles, Applications, Techniques of EXAFS, SEXAFS, XANES*, Wiley, New York, 1988.
52. T. J. McCarthy, S. P. Ngeyl, J. H. Liao, D. C. DeGroot, T. Hogan, C. R. Kannewurf and M. G. Kanatzidis, *Chemistry of Materials*, 1993, **5**, 331-340.

53. N. F. Zheng, X. H. Bu and P. Y. Feng, *Journal of the American Chemical Society*, 2005, **127**, 5286-5287.
54. A. L. Spek, *PLATON, A Multipurpose Crystallographic Tool*, Utrecht, 2005.
55. C. L. Cahill and J. B. Parise, *Chemistry of Materials*, 1997, **9**, 807-811.
56. Y. Zhang, B. Fluegel, A. Mascarenhas, H. P. Xin and C. W. Tu, *Physical Review B*, 2000, **62**, 4493-4500.
57. B. Tripathi, Y. K. Vijay, S. Wate, F. Singh and D. K. Avasthi, *Solid-State Electronics*, 2007, **51**, 81-84.
58. T. A. Herskovitz, B. A. Holm, R. H. Ibers, J. A. Phillips and J. F. Weiher, *Proceedings of the National Academy of Sciences*, 1972, **69**, 2437.
59. A. H. Averill, T. Holm and R. H. Ibers, *Journal of the American Chemical Society*, 1973, **95**, 3523.
60. J. G. Reynolds and R. H. Holm, *Inorganic Chemistry*, 1980, **19**, 3257.
61. K. S. Hagen, A. D. Watson and R. H. Holm, *Journal of the American Chemical Society*, 1983, **105**, 3905.
62. K. S. Hagen, A. D. Watson and R. H. Holm, *Inorganic Chemistry*, 1984, **23**, 2984.
63. S. Rutchik, S. Kim and M. A. Walters, *Inorganic Chemistry*, 1988, **27**, 1515.
64. D. Coucouvanis, M. G. Kanatzidis, W. R. Dunham and W. R. Hagen, *Journal of the American Chemical Society*, 1984, **106**, 7998.
65. R. Fong, J. R. Dahn, R. J. Batchelor, F. W. B. Einstein and C. H. W. Jones, *Physics Review B*, 1989, **39**, 4424-4429.
66. J. Llanos, C. Contrerasortega, C. Mujica, H. G. Vonschnering and K. Peters, *Materials Research Bulletin*, 1993, **28**, 39-44.
67. C. Mujica, J. Paez and J. Llanos, *Materials Research Bulletin*, 1994, **29**, 263-268.
68. J. Llanos, P. Valenzuela, C. Mujica, A. Buljan and R. Ramirez, *Journal of Solid State Chem*, 1996, **122**, 31-35.
69. C. L. Mujica, J. Llanos, M. Guzmán and C. Contreras-Ortega, *Nucleotecnica*, 1994, **14**, 23.
70. G. A. Renovitch and W. A. Baker, *Journal of the American Chemical Society*, 1968, **90**, 3585-3587.
71. H. M. Powell and R. V. G. Ewens, *Journal of the Chemical Society*, 1939, 286-292.

Curriculum Vita

Min Wu

Education

Ph.D. of Materials/Inorganic Chemistry Department of Chemistry and Chemical Biology Rutgers, The State University of NJ-New Brunswick	2002 ~ 2007
B.S. of Analytical Chemistry Department of Chemistry Beijing University of Chemical Technology, P.R.China	1996 ~ 2000

Experience

Research Assistant Department of Chem. & Chem. Biol., Rutgers University-New Brunswick	2002 ~ 2007
Teaching Assistant Department of Chem. & Chem. Biol., Rutgers University-New Brunswick	2002 ~ 2007
Internship (GC-MS Analyst) Accutest Laboratories (Corporate Headquarters), Dayton, NJ	2003
Associate Scientist Beijing Research Institute of Chemical Industry, SINOPEC, P.R.China	2000 ~ 2001
Internship Yanshan Petrochemical Company, P.R.China	1999

Honors and Awards

Certificate of Teaching with Technology (Rutgers University)	2006
Rieman Prize for Outstanding Teaching Performance (Rutgers University)	2006
Morgan Fund (Rutgers University)	2003 ~ 2004
Vice president of Chemistry Students Association (BUCT, China)	1998 ~ 1999
Academic Excellent Scholarship (BUCT, China)	1996 ~ 2000

Publication and Presentation

1. **Wu, M.**, Huang, X. Y., Emge T., Li, J. Unique magnetic Iron/cobalt sulfide with 2D layered structure and thin film process. *In Preparation*.
2. **Wu, M.**, Emge T., Huang, X. Y., Zhang Y., Li, J. Design and tuning properties of three dimensional porous quaternary chalcogenide built on a bimetallic tetrahedral cluster $[M_4Sn_3S_{13}]^{5-}$ (M = Zn/Sn). *Journal of Solid State Chemistry, in press*
3. **Wu, M.**, Su, W. P., Jasutkar, N., Huang, X. Y., Li, J. An open-framework bimetallic chalcogenide structure $K_3Rb_3Zn_4Sn_3Se_{13}$ built on a unique $[Zn_4Sn_3Se_{16}]^{12-}$ cluster: synthesis, crystal structure, ion exchange and optical properties. *Materials Research Bulletin* 40, 21-27 (2005).
4. **Wu, M.**, Rhee, H. K., Huang, X. Y., Li, J. Synthesis and characterization of ZnO-L (L=ethylenediamine, aniline) materials. *The 37th Middle Atlantic Regional Meeting of the American Chemical Society*, Piscataway, NJ, USA, 2005.
5. **Wu, M.**, Li, J., Huang, X. Y., Su, W. P. Open framework materials based on Sn-M-Q secondary building blocks (M = Zn, Co, Mn; Q = S, Se). *ACS national Meeting 228*, Philadelphia, PA, USA, 2004.
6. **Wu, M.**, Huang, X. Y., Li, J. Synthesis and characterization of Sn-Zn-Se base open-framework compound $K_3Rb_3Sn_3Zn_4Se_{13}$ and its derivatives. *The 36th Middle Atlantic Regional Meeting of the American Chemical Society*, Princeton, NJ, USA, 2003